Physik - Department

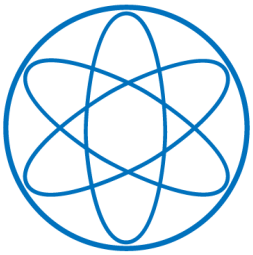

Point Defects in MnSi and YBCO Studied by Doppler Broadening Spectroscopy Using a Positron Beam

Dissertation
von

Markus Reiner

Technische Universität München

Technische Universität München

Lehrstuhl E21 für Experimentalphysik

Point Defects in MnSi and YBCO Studied by Doppler Broadening Spectroscopy Using a Positron Beam

Markus Reiner

Vollständiger Abdruck der von der Fakultät für Physik der Technischen Universität München zur Erlangung des akademischen Grades eines

Doktors der Naturwissenschaften (Dr. rer. nat.)

genehmigten Dissertation.

Vorsitzender:	apl. Prof. Dr. Norbert Kaiser
Prüfer der Dissertation:	1. Priv.-Doz. Dr. Christoph Hugenschmidt
	2. Univ.-Prof. Dr. Johannes Barth

Die Dissertation wurde am 08.09.2015 bei der Technischen Universität München eingereicht und durch die Fakultät für Physik am 28.10.2015 angenommen.

Summary

Within the scope of this thesis, positrons were used for probing high-quality crystals of two materials in the focus of permanent attention in solid state physics, namely bulk MnSi and thin films of $YBa_2Cu_3O_{7-\delta}$. For this purpose, Doppler Broadening Spectroscopy (DBS) of the electron-positron annihilation line was applied using the high-intensity positron beam at the NEutron induced POsitron Source MUniCh (NEPOMUC) at the Forschungsreaktor München II (FRM II). Cooperation partners from Technische Universität München and Universität Augsburg provided the monocrystalline specimens. The DBS experiments were conducted at the so-called CDB spectrometer designed for implanting positrons with a well defined incident energy into specimens and analyzing the Doppler shift of the annihilation γ-quanta. Prior to the measurements, the beam spot size at the sample position was minimized and a maximum resolution of around 200 μm (full width at half maximum) at an incident energy of 30 keV was achieved. Furthermore, a new apparatus was constructed and set into operation which enables the heating of samples up to temperatures of 900 °C while biased at high voltages down to -25 kV. For a reliable interpretation of the recorded data, complementary techniques such as analysis of the chemical composition or positron lifetime measurements were applied. The calculation of annihilation characteristics in matter was an accompanying method of high importance for corroborating conclusions from the measurements. In all probed MnSi crystals, only Mn vacancies and no Si vacancies were found. Moreover, Mn vacancies were shown to homogeneously distribute in the crystals. The concentration as precisely measured at the NEPOMUC beam excellently agreed with results obtained in an additional experiment where positrons were generated by absorption of high-energetic γ-radiation in the crystals. Positrons in $YBa_2Cu_3O_{7-\delta}$ are highly sensitive to the oxygen deficiency δ. A reliable correlation between the Doppler broadening of the annihilation radiation and δ was established. In unique studies, it was possible to investigate the spatial variation of δ and its time dependent evolution at elevated temperatures in-situ. Moreover, in a collaboration with the Universität der Bundeswehr München, novel, pixelated high-purity Germanium detectors were used for the first time in coincident measurements of the Doppler shifts of both annihilation quanta.

Zusammenfassung

Im Rahmen dieser Arbeit wurden Positronen benutzt, um qualitativ hochwertige Kristalle zweier Materialien zu untersuchen, die im Brennpunkt langanhaltender Aufmerksamkeit in der Festkörperphysik stehen, nämlich Bulkproben aus MnSi und dünne Filme aus $YBa_2Cu_3O_{7-\delta}$. Zu diesem Zwecke wurde die Doppler-Verbreiterungs-Spektroskopie (DBS) der Annihilationslinie von Elektronen und Positronen am Strahl der hochintensiven neutroneninduzierten Positronenquelle München (NEPOMUC) am Forschungsreaktor München II (FRM II) angewendet. Kooperationspartner an der Technischen Universität München und der Universität Augsburg stellten die einkristallinen Proben zur Verfügung. Die DBS-Experimente wurden am sogenannten CDB-Spektrometer durchgeführt, dass dafür ausgelegt ist, Positronen mit wohldefinierter Energie in eine Probe zu implantieren und die Dopplerverschiebung der Annihilationsgammaquanten zu analysieren. Vor den Messungen wurde der Strahldurchmesser am Probenort minimiert und eine maximale Ortsauflösung von 200 μm (Halbwertsbreite) bei einer Auftreffenergie von 30 keV erreicht. Außerdem wurde eine neue Vorrichtung konstruiert und in Betrieb genommen, die es erlaubt, Proben auf Temperaturen von bis zu 900 °C zu heizen während eine Hochspannung von bis zu -25 kV anliegt. Zur verlässlichen Interpretation der aufgenommenen Daten wurden ergänzende Techniken wie die Analyse der chemischen Zusammensetzung oder Positronenlebensdauermessungen angewendet. Von hoher Wichtigkeit für die Bekräftigung von Schlussfolgerungen aus den Messungen war die Berechnung von Annihilationscharakteristiken in Materie als begleitende Methode. In allen untersuchten MnSi Kristallen wurden nur Mn und keine Si Fehlstellen nachgewiesen. Außerdem wurde gezeigt, dass Mn Leerstellen in den Kristallen homogen verteilt sind. Die Konzentration, die am NEPOMUC-Strahl genau gemessen wurde, stimmte hervorragend mit den Ergebnissen eines zusätzlich durchgeführten Experiments überein, bei dem die Positronen durch Absorption hochenergetischer Gammaquanten in den Kristallen erzeugt wurden. Positronen in $YBa_2Cu_3O_{7-\delta}$ sind hochempfindlich auf das Sauerstoffdefizit δ. Eine verlässliche Korrelation zwischen der Dopplerverbreiterung der Annihilationsstrahlung und δ wurde gefunden. In einzigartigen Studien konnte die räumliche Variation von δ und sein zeitabhängiges Verhalten bei hohen Temperaturen in-situ untersucht werden. Zudem wurden in Zusammenarbeit mit der Universität der Bundeswehr München neuartige gepixelte hochreine Germanium-Detektoren das erste Mal in koinzidenten Messungen der Dopplerverschiebung beider Annihilationsquanten verwendet.

Contents

Chapter 1

1 Introduction

In non-destructive Positron Annihilation Spectroscopy (PAS), which is well described in review articles and textbooks [1–5], positrons are used for probing solids in order to reveal information on electronic or structural properties. This information is obtained by analyzing the observables of the electron-positron annihilation radiation. Among the numerous techniques applied for investigating solids, such as microscopy, X-ray and neutron scattering, measurements of thermodynamic, electric or magnetic properties or analysis of the chemical composition, PAS features an outstanding sensitivity on open volume defects like vacancies, dislocations or voids. The type and concentration of such defects is probed by Positron Annihilation Lifetime Spectroscopy (PALS) or (Coincident) Doppler Broadening Spectroscopy ((C)DBS). In PALS, the positron lifetime in matter of up to a few 100 ps is measured. In (C)DBS, the Doppler shift of the annihilation γ-quanta energy from $m_0c^2 = 511\,\mathrm{keV}$, which amounts up to typically 10 keV, is evaluated.[1] The signature of (C)DB spectra is determined by the momentum distribution of the annihilating electron-positron pair and can be calculated using, e. g., the MIKA Doppler program [6]. CDBS is particularly suited to determine the chemical vicinity of the annihilation site and thus, to characterize this site. Both, PALS and (C)DBS can be used for measuring the concentration of open volume defects.

The use of monoenergetic, so-called slow positron beams for PAS is an enhanced technique. It allows depth dependent investigations by varying the incident positron energy [7, 8]. Positron beams are an excellent tool for examining thin films up to a thickness of several 100 nm. For the studies presented in this thesis, a high-intensity and high-brightness positron beam provided by the NEutron induced POsitron source MUniC (NEPOMUC) at the ForschungsReaktor München II (FRM II) was used [9–11]. The experiments were conducted at the so-called CDB spectrometer [12–14]. This was designed for (C)DBS measurements and successfully applied in many research projects in the past

[1] m_0 denotes the electron or positron mass and c the speed of light.

as can be seen exemplarily in several publications [15–22]. Important prospects of this apparatus are the possible use for laterally resolved measurements, in-situ experiments at lower and elevated temperatures and fast detection of CDB spectra.

The main focus of the present thesis was the application of (C)DBS at NEPOMUC in order to investigate single-crystalline bulk MnSi and thin films of $YBa_2Cu_3O_{7-\delta}$ (YBCO). MnSi is of high interest due to its exotic magnetic properties driven by strong electronic correlations. Despite numerous experimental studies published in literature (see e. g. references [23–36]), the presence and role of lattice defects has not been investigated in detail so far. A comprehensive defect study will be presented in this thesis with a focus onto the detected vacancies. YBCO is a well known material due to the found high-temperature superconductivity [37–39]. In this system, the superconductive properties, e. g. the critical temperature T_c, depend on the oxygen deficiency δ. Thus, the reliable characterization of δ is important for a deeper understanding of superconductivity and other recently observed phenomena such as charge-density-wave order [40–42] and their possible application in technical devices [43–45]. Here, particularly thin films have a great potential which can be prepared with high quality. The benefit of positrons as nanoprobes for the oxygen deficiency in thin YBCO films will be demonstrated.

The main part of this thesis is structured as follows: Firstly, it is shown how positrons can be used to probe open volume defects in solids in chapter 2. The techniques of (C)DBS and PALS as well as the concept of slow monoenergetic positrons are described. In chapter 3, a method for calculating CDB spectra and lifetimes of positron states in solids is explained which was routinely applied in the present work. Subsequently, in chapter 4, the CDB spectrometer at the NEPOMUC positron source is introduced; especially the performed adjustments for laterally resolved measurements, the installation of a new sample heating device and first measurements with a novel detector system of pixelated High-Purity Ge (HPGe) detectors are treated. The comprehensive studies on MnSi and YBCO are presented in chapter 5 and 6, respectively. Finally, a conclusion of this work is given in chapter 7.

Chapter 2
2 Defect Spectroscopy with Positrons

The positron is the anti-particle of the electron. The existence of this elementary particle was postulated by Dirac [46,47] in 1930/31 prior to its discovery by Anderson in 1932 [48]. The positron has the same properties as the electron but an opposite charge and magnetic moment. Since open volume defects in solids form an attractive potential for positrons, PAS is a standard technique for defect spectroscopy. Observing the electron-positron annihilation by (C)DBS or PALS allows one to draw conclusions about the presence of various defect types and their concentration. For this purpose, the so-called trapping model is most commonly applied. Depth dependent PAS using the slow positron beam technique enables to investigate thin film systems and depth distributions of defects. Basics of these techniques are explained in the following.

2.1 Positrons in Matter

The Fate of Positrons in Matter

In most PAS experiments, positrons stem from radioactive isotopes such as ^{22}Na or from slow positron beams. These positrons, which have typical kinetic energies between a few eV and around several 100 keV, are implanted into solids. During and after implantation, several processes occur which are summarized in figure 2.1. A fraction of the positrons is reflected at the surface, which is not of further interest in the following. At very low incident energies below typical 2 keV, some of the positrons annihilate or leave the solid prior to their complete thermalization as so-called epithermal positrons [49–51]. All other incident positrons are rapidly thermalized within a few picoseconds and subsequently only have thermal energies. After thermalization positrons have a well defined depth distribution as explained in section 2.4. The thermalized positrons diffuse through the solid until they annihilate with an electron in the bulk with a rate of typically 10^{10} /s. The annihilation in defect free bulk can be analyzed for probing the electronic structure by

measuring the Angular Correlation of the Annihilation Radiation (ACAR). Prior to the annihilation in the bulk, other phenomena can take place during diffusion: (i) The positron gets trapped in open volume defects such as vacancies, dislocations, grain boundaries or voids. (ii) The positron reaches the surface and annihilates there or leaves the solid as moderated positron if energetic favorable. Effect (i) is used in defect spectroscopy as conducted by (C)DBS and PALS within this thesis. Effect (ii) is applied for analyzing the chemical composition in the top-most atomic layer by Positron induced Auger Electron Spectroscopy (PAES) [52,53] or for the brightness enhancement of slow positron beams by using reemitted and hence, remoderated positrons for beam formation [54]. Under some circumstances it is possible that the positron annihilates after having formed Positronium (Ps), i. e., in a bound state with a single electron. In metals and semiconductors, the annihilation of Ps is often observed at the surface. Nearly always, a decay into two or three γ-quanta takes place in dependence on the total spin of the Ps atom. For spin one, the three γ-quanta emitted in most cases have a continuous energy spectrum [55].

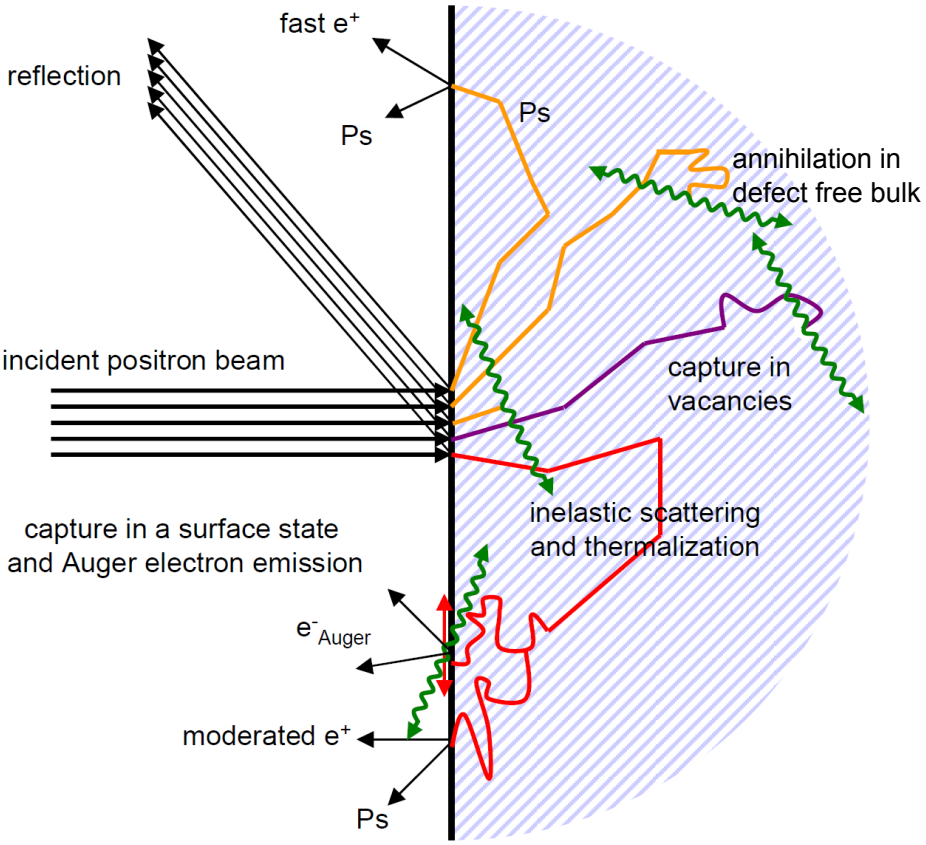

Figure 2.1: The fate of positrons implanted into a solid: Possible processes are sketched. In this thesis, CDBS and PALS were used in order to distinguish the annihilation in defect free bulk or after capture in vacancies (figure taken from [56]).

Electron-Positron Annihilation

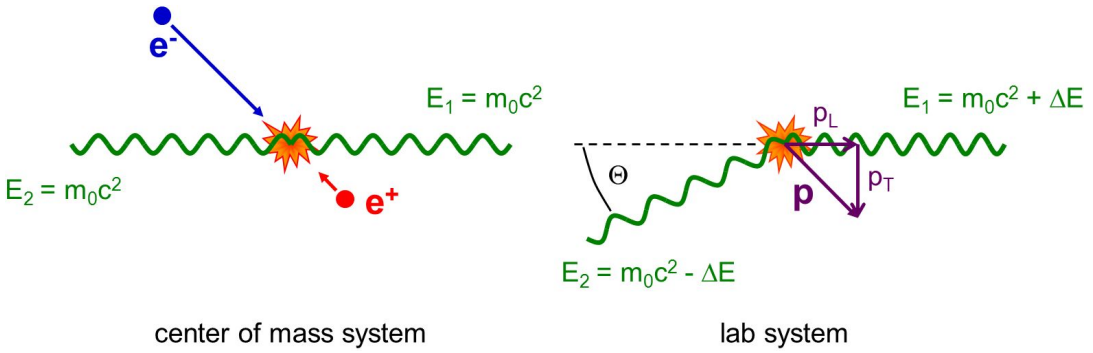

Figure 2.2: Electron-positron annihilation in the center of mass and lab system, where an angular deviation Θ in the emission direction and a Doppler shift ΔE of the energy of the γ-quanta are detected due to the momentum $\mathbf{p}$ of the annihilating pair.

The annihilation in solids takes place with surrounding electrons and almost always leads to the emission of two γ-quanta. The probability Γ for the annihilation is given by

$$\Gamma = \pi r_0 c^2 n_- \tag{2.1}$$

with the electron density n_- and the classical electron radius $r_0 = \frac{e^2}{m_0 c^2}$ [1].[1] Thus, positrons annihilate with a rate of around 10^{10} /s in defect free metals. In the center of mass system of the annihilating pair, the two annihilation γ-quanta with an energy of m_0c^2 are emitted in opposite directions. An angular deviation Θ from 180° and a Doppler shift ΔE from m_0c^2 are observed in the lab system. These are caused by the momentum $\mathbf{p}$ of the annihilating pair as shown in figure 2.2. Since the positrons are thermalized in a solid, this momentum mainly stems from electrons which are bound at least with a few electronvolts. The momentum component p_T transversal to the emission direction leads to the angular deviation

$$\Theta = \frac{p_T}{m_0 c} \tag{2.2}$$

of the γ-quanta [1]. This deviation is measured in ACAR for investigating Fermi surfaces, which requires a high lateral resolution for the coincident detection of the annihilation γ-quanta. The longitudinal momentum component p_L results in an energy shift

$$\Delta E = \frac{1}{2} p_L c \tag{2.3}$$

of the γ-quanta [1]. In (C)DBS, this energy shift is measured with high resolution in order to characterize the annihilation site as defect free bulk or a certain kind of defect.

[1] e denotes the elementary charge.

2.2 Positrons as Probe for Open Volume Defects

The missing atomic cores in vacancies and other kind of open volume defects form a potential well for positively charged particles. Positrons are very likely to be trapped there, which explains the high suitability of PAS for defect spectroscopy. Basics of this process are described in various textbooks or review articles, see e. g. [57]. Typical binding energies for positrons in metallic vacancies are around 1.0 eV. In semiconductors, the situation is more complex and various aspects like, e. g., the charge state of a vacancy play a role in the trapping process. The positron capture in open volume defects is illustrated in figure 2.3 for the simple case of a monovacancy in Cu. The probability density $|\Psi_+(\mathbf{r})|^2$ of the positron is plotted. In defect free Cu, the positron occupies a delocalized state and $|\Psi_+(\mathbf{r})|^2$ has the highest amplitudes in the interatomar space. In the presence of a vacancy, $|\Psi_+(\mathbf{r})|^2$ is localized at its site due to the trapping of the positron.

In PAS, the trapping of positrons is investigated in order to determine present types

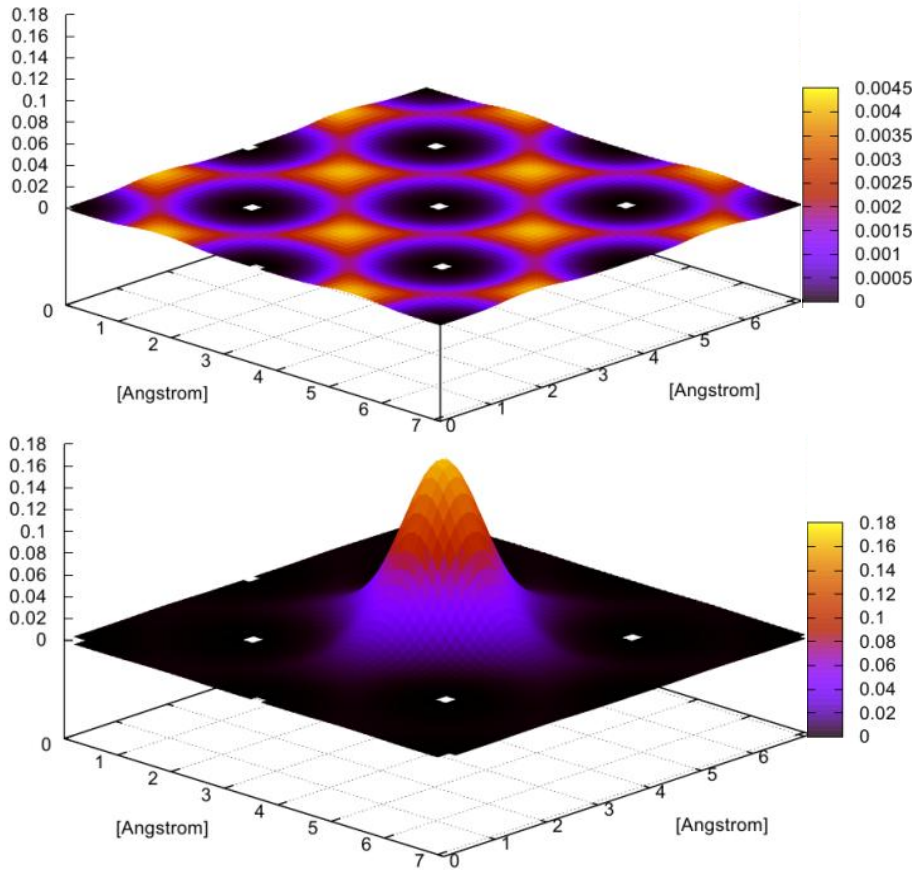

Figure 2.3: 2D plot of the positron probability density $|\Psi_+(\mathbf{r})|^2$ in Cu. *Top*: Defect-free Cu. *Bottom*: Vacancy in Cu (figure taken from [58]).

of vacancy-like defects as well as their distribution and concentration. Positrons trapped in open volume defects show longer lifetimes due to a locally decreased electron density and their annihilation radiation is less Doppler broadened due to a smaller overlap with high momentum core electrons. For analyzing PALS or CDBS data, the so-called trapping model is applied, which is well described in literature, e. g. in [57]. Here, a simple case is considered with only a single type of vacancy present in the solid. It is assumed that detrapping of captured positrons does not play a role as it is mostly the case at room temperature. The following rate equations describe the probabilities $n_\mathrm{b}(t)$ and $n_\mathrm{v}(t)$ of a positron to be delocalized in defect free bulk or trapped in vacancies, respectively, as function of the time t:

$$\frac{\mathrm{d}n_\mathrm{b}(t)}{\mathrm{d}t} = -\lambda_\mathrm{b} n_\mathrm{b}(t) - \kappa_\mathrm{v} n_\mathrm{b}(t) \tag{2.4}$$

$$\frac{\mathrm{d}n_\mathrm{v}(t)}{\mathrm{d}t} = -\lambda_\mathrm{v} n_\mathrm{v}(t) + \kappa_\mathrm{v} n_\mathrm{b}(t) \tag{2.5}$$

Here, λ_b and λ_v denote the positron annihilation rates in both states with $\lambda_\mathrm{b} > \lambda_\mathrm{v}$ as described above. The trapping coefficient κ_v depends by

$$\kappa_\mathrm{v} = \mu_\mathrm{v} c_\mathrm{v} \tag{2.6}$$

on the vacancy concentration c_v with μ_v as vacancy specific trapping coefficient[2]. The equations 2.4 and 2.5 are solved with the boundary conditions

$$n_\mathrm{b}(0) = 1 \qquad \text{and} \qquad n_\mathrm{v}(0) = 0 \tag{2.7}$$

indicating that all incident positrons are implanted into the defect free bulk. This leads to $n_+(t)$ as probability for the positron to be alive in the solid

$$n_+(t) = n_\mathrm{b}(t) + n_\mathrm{v}(t) = \frac{\lambda_\mathrm{b} - \lambda_\mathrm{v}}{\lambda_\mathrm{b} - \lambda_\mathrm{v} + \kappa_\mathrm{v}} \exp\left[-\left(\lambda_\mathrm{b} + \kappa_\mathrm{v}\right) t\right] + \frac{\kappa_\mathrm{v}}{\lambda_\mathrm{b} - \lambda_\mathrm{v} + \kappa_\mathrm{v}} \exp\left[-\lambda_\mathrm{v} t\right] \tag{2.8}$$

at a given time t. Thus, due to trapping of positrons in vacancies, two characteristic lifetimes can be detected in PALS. The fraction η_v of positrons annihilating in a vacancy is given by

$$\eta_\mathrm{v} = \int_0^\infty \mathrm{d}t \; \lambda_\mathrm{v} n_\mathrm{v}(t) = \frac{\kappa_\mathrm{v}}{\lambda_\mathrm{b} + \kappa_\mathrm{v}} \tag{2.9}$$

whereas the remainder of the positrons $\eta_\mathrm{b} = 1 - \eta_\mathrm{v}$ annihilates in the bulk. These fractions can be determined from CDBS measurements. Typically, vacancy concentrations in a range between 10^{-7} and 10^{-4} per atom can be measured. The presented model also describes positron trapping in any other kind of open volume defects and agglomerations of foreign atoms with a higher affinity to positrons than the surrounding bulk [59, 60].

[2] for monovacancies in metals: $\mu_\mathrm{v} = 10^{14} - 10^{15}/\mathrm{s}$ [57]

2.3 Techniques of PAS for Defect Spectroscopy

2.3.1 Doppler Broadening Spectroscopy (DBS)

In conventional DBS, the energy of the annihilation radiation is measured with High-Purity Germanium (HPGe) detectors with a typical energy resolution of 1.4 keV (FWHM) at 511 keV. A Doppler broadened profile is detected due to shift ΔE of the energy of the annihilation γ-quanta as defined by equation 2.3. The analysis of this profile enables to reveal the contribution of various positron states to the annihilation. The broadening is smaller for positrons trapped in defects as discussed above and shown by the exemplary spectra in figure 2.4. For a quantitative analysis, most commonly two lineshape parameters are determined from DBS spectra, the so-called S-parameter S and the W-parameter W [8]. In defect rich samples, S is higher and W is lower compared to defect free bulk. As illustrated in figure 2.4, S is given by the area below the central part whereas W is the area below the outer wing. Both areas are normalized by the total area of the profile. The peak is background corrected prior the evaluation of the respective areas. This correction is done by fitting the background levels left and right of the peak and subtracting an error-function [61]. In this work, the central part is defined by $\Delta E < 0.84$ keV. This leads to $S \approx 0.5$ which causes the minimal statistical error ΔS for S [12]. An individual energy interval for W was chosen for each investigated system based on the CDBS results.

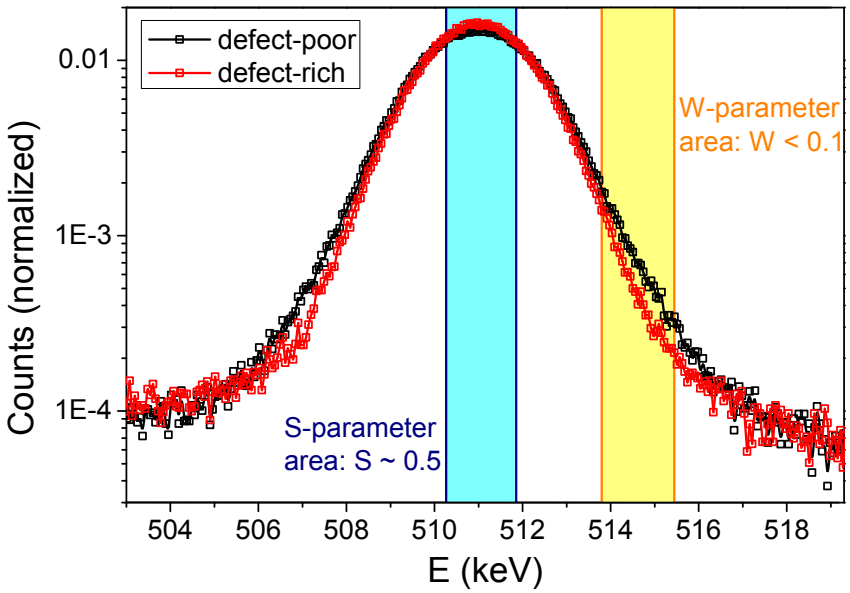

Figure 2.4: Doppler broadened profile of the annihilation line as measured by a High-Purity Germanium (HPGe) detector in a defect-poor and defect-rich specimen of MnSi. The lineshape parameters S and W are determined from the marked areas and used for the evaluation. S increases whereas W decreases in open volume defects.

Often, a superposition of various positron states with characteristic S-parameters and W-parameters is detected in samples. In the previously discussed case from section 2.2, these states would be the defect-free bulk with S_b and W_b and the monovacancy with S_v and W_v as characteristic lineshape parameters. Thus, one would detect the S-parameter

$$S = \eta_\mathrm{b} S_\mathrm{b} + \eta_\mathrm{v} S_\mathrm{v} = (1 - \eta_\mathrm{v})\, S_\mathrm{b} + \eta_\mathrm{v} S_\mathrm{v} \tag{2.10}$$

and the W-parameter

$$W = \eta_\mathrm{b} W_\mathrm{b} + \eta_\mathrm{v} W_\mathrm{v} = (1 - \eta_\mathrm{v})\, W_\mathrm{b} + \eta_\mathrm{v} W_\mathrm{v} \tag{2.11}$$

with η_v as fraction of positrons annihilating in a vacancy as given by equation 2.9. Since S is more sensitive to the annihilation with valence electrons and W to the annihilation with core electrons, investigating the correlation between S and W facilitates the data interpretation. In the considered case, a varying concentration c_v of vacancies leads to correlated changes in S and W: Plotting S and W in a so-called S-W-plot, as shown in figure 5.4, yields a straight line on which the data points lie. The end points of this line are the extremal points (S_b,W_b) and (S_v,W_v). Therefore, in more complex cases, in particular when additional positron states become present in a sample, the analysis of such S-W-plots facilitates the data interpretation as can be seen, e. g., in [62].

2.3.2 Coincident Doppler Broadening Spectroscopy (CDBS)

In CDBS [63, 64], the energy of both annihilation quanta is measured in coincidence by use of a collinear set-up of two HPGe detectors. Events coincidentally detected in both detectors are plotted in a 2D map with the coordinate axes E_1 and E_2, i. e. the energies measured in the respective detectors. Their sum energy E_sum amounts to 1022 keV in the case of a valid event. Actually, E_sum is reduced by the binding energy of the annihilating electron and positron, but this deficit only leads to marginal shifts [8, 65]. Thus, valid events in the coincident photo peak can be extracted from the 2D spectra. Details of the analysis are described in [12, 66]. An evaluation algorithm developed by Pikart was used [67] for the present studies. Compared to spectra of conventional DBS using a single detector, CDB spectra have an increased peak to background ratio of around $10^5 : 1$ and an effective energy resolution enhanced by a factor of $\sqrt{2}$. The theoretical background and calculation of CDB spectra is described in detail in chapter 3.

Exemplarily, CDB spectra measured in annealed samples of Al and Cu are shown in figure 2.5(a). Usually, the so-called CDB ratio curves are evaluated, which are obtained by dividing normalized CDB spectra by a reference spectrum chosen for each study individually. In figure 2.5(b), the CDB ratio curve of Cu with respect to Al is plotted. Obviously, the CDB signature is element dependent and can be used for a characteriza-

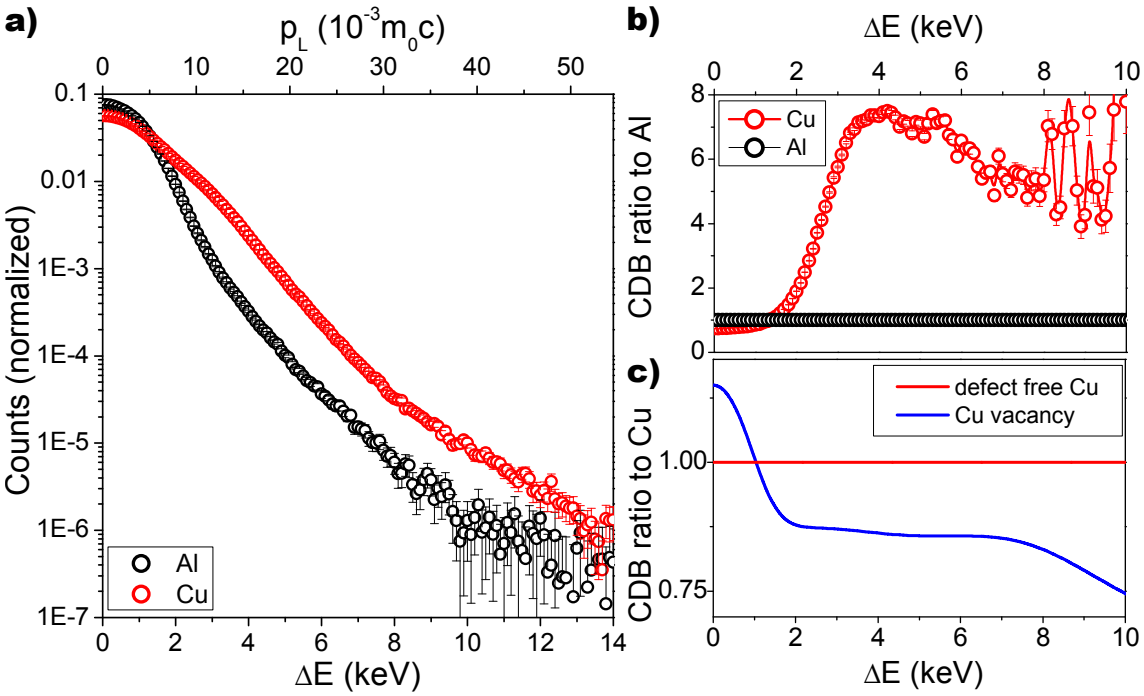

Figure 2.5: (a) CDB spectra of Al and Cu as function of the Doppler shift ΔE and the longitudinal momentum component p_L. (b) Element specific CDB ratio curves of Al and Cu as obtained from the spectra shown in (a) with Al as reference. (c) Structure specific CDB ratio curves calculated for positrons annihilating in Cu vacancies and defect-free Cu with the spectrum of defect-free Cu as reference.

tion of the chemical vicinity of the annihilation site. This element sensitivity is caused by the annihilation with core electrons bound with element characteristic energies. Also the identification of defect types is possible by CDB spectra as the theoretical ratio curves plotted in figure 2.5(c) demonstrate. The respective spectra were calculated for defect free Cu and a Cu monovacancy, respectively. They were folded with a Gaussian in order to mimic the experimental energy resolution of around 1 keV (FWHM); the spectrum for bulk Cu serves as CDB reference. Compared to this, the ratio curve of the monovacancy in Cu shows an enhancement for low Doppler shifts $\Delta E < 1\,\mathrm{keV}$ and a lower intensity for high Doppler shifts. These features correspond to a lower probability for annihilation with high momentum core electrons in open volume defects as described in section 2.2. In contrast, the probability with low momentum valence electrons is relatively increased. In conventional DBS, a higher S- and a lower W-parameter are detected here.

When annihilation in several positron states takes place, a superposition of various CDB spectra or ratio curves is observed. In the previously discussed case of annihilation in defect free bulk and in a monovacancy, a behavior analogous to that of the lineshape parameters S and W, as described by equations 2.10 and 2.11, is observed in CDBS.

Consequently, one detects, as function of the Doppler shift ΔE, a CDB spectrum

$$I(\Delta E) = \eta_{\mathrm{b}} I_{\mathrm{b}}(\Delta E) + \eta_{\mathrm{v}} I_{\mathrm{v}}(\Delta E) = (1 - \eta_{\mathrm{v}}) I_{\mathrm{b}}(\Delta E) + \eta_{\mathrm{v}} I_{\mathrm{v}}(\Delta E) \tag{2.12}$$

which stems from a superposition of the spectra $I_{\mathrm{b}}(\Delta E)$ and $I_{\mathrm{v}}(\Delta E)$ characteristic for defect free bulk and the vacancy, respectively. Such a superposition of CDB spectra is analyzed in chapter 5 in order to determine vacancy concentrations in MnSi from η_{v}.

2.3.3 Positron Annihilation Lifetime Spectroscopy (PALS)

In PALS, the measurement of positron lifetimes requires a start signal. The widely used positron emitter ^{22}Na decays into an excited stated of ^{22}Ne. This state de-excites instantaneously by emission of a γ-quantum with an energy of 1275 keV, which serves as start signal. In the case of pulsed beams, the start signal is obtained from the pulsing apparatus. The annihilation quanta are usually detected by a BaF_2 detector set-up with a high time resolution of typically 200 - 250 ps. The positron lifetime spectrum is given by the probability of an annihilation at certain time t and hence, is described by

$$-\frac{\mathrm{d}n_+(t)}{\mathrm{d}t} = \sum_i I_i \lambda_i \exp\left[-\lambda_i t\right] \tag{2.13}$$

as a sum of exponential decay components with relative intensities I_i characteristic for the positron states present in a sample [57]. The states are described by

$$\tau_i = \frac{1}{\lambda_i} \tag{2.14}$$

as characteristic lifetimes. In the previously discussed case of annihilations in defect free bulk and in a vacancy, where $n_+(t)$ is described by equation 2.8, two decay components are detectable. The respective annihilation rates

$$\lambda_1 = \lambda_{\mathrm{b}} + \kappa_{\mathrm{v}} \qquad \text{and} \qquad \lambda_2 = \lambda_{\mathrm{v}} \tag{2.15}$$

lead to a short-lived bulk component $\tau_1 = 1/\lambda_1$ as the so-called reduced bulk lifetime and to $\tau_2 = 1/\lambda_2 = \tau_{\mathrm{v}}$ as long-living vacancy component. The effective bulk annihilation rate $\lambda_{\mathrm{eff}} = \lambda_1$ is increased due to the vanishing of positrons in vacancies after capture. The mean lifetime of the positrons in the sample τ_{mean} is then given by

$$\tau_{\mathrm{mean}} = I_1 \tau_1 + I_2 \tau_2. \tag{2.16}$$

The convolution of equation 2.13 with a Gaussian or a sum of Gaussians describes measured spectra [68] detected with a finite resolution as exemplarily shown in figure 5.10.

2.4 Depth Profiling Using Slow Positrons

Slow monoenergetic positron beams enable depth dependent investigations [7, 8]. The application of this technique requires UHV conditions, i. e. pressures below 10^{-6} mbar. With incident positron energies E_+ in a typical range between 0.1 and 30 keV, it is possible to measure defect concentrations and analyze thin film system as demonstrated in the following.

2.4.1 Depth Dependent PAS

Positron Implantation

The variation of the incident positron energy E_+ enables depth profiling with positrons. After thermalizing within a few picoseconds due to scattering processes mainly with electrons and phonons, the depth distribution of positrons is described by so-called Makhovian profiles [2]. The mean positron implantation depth $\bar{z}$ is given by

$$\bar{z} = \frac{A}{\rho} {E_+}^n \tag{2.17}$$

with A and n as material dependent parameters and the mass density ρ. Typically, at $E_+ = 30$ keV a depth up to 5 μm is probed. The respective depth distribution as function of depth z is described by the implantation profile

$$P(z, E_+) = \frac{m z^{m-1}}{z_0^m} \exp\left[\left(-\frac{z}{z_0}\right)^m\right] \tag{2.18}$$

and depends on the incident energy E_+. Here, m and

$$z_0 = \frac{\bar{z}}{\Gamma\left(1/m + 1\right)} \tag{2.19}$$

Material	$\boldsymbol{A}$ **(keV$^{-n}\mu$g/cm^2)**	$\boldsymbol{m}$	$\boldsymbol{n}$
Au	6.58	1.71	1.49
Cu	3.78	1.78	1.61
Ge	4.3	1.78	1.6
Si	3.3	1.91	1.69

Table 2.1: Makhovian parameters which describe the depth distribution of positrons implanted in various elements (values taken from [2]).

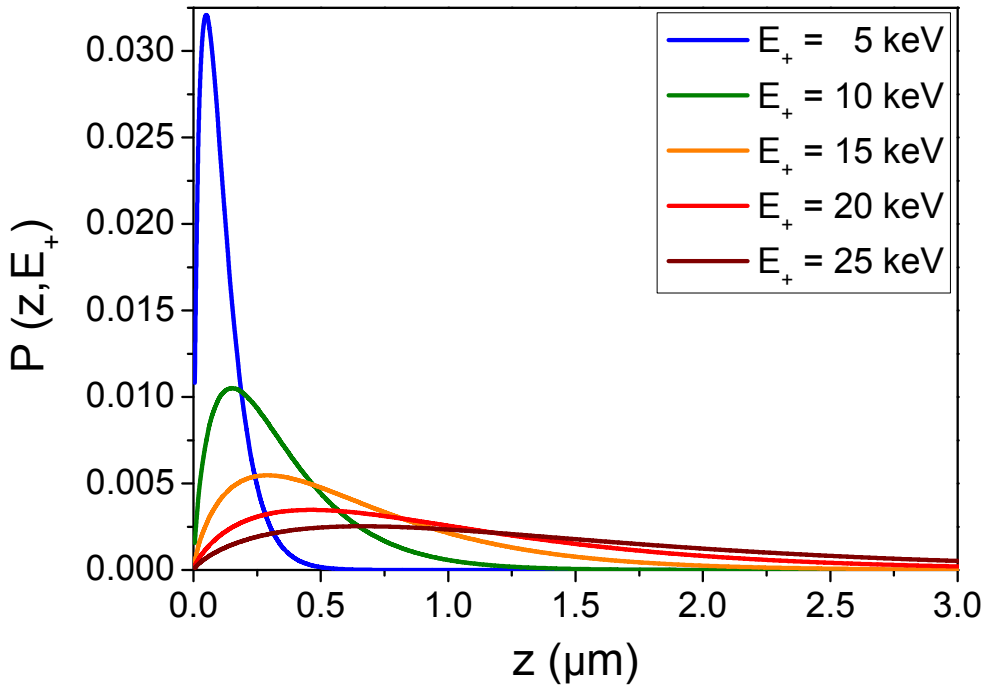

Figure 2.6: Depth distribution $P(z, E_+)$ of implanted and thermalized positrons as function of the depth z for various incident energies E_+ in Cu.

which depends on $\bar{z}$ are material dependent parameters. The so-called Makhovian parameters A, m and n are given in table 2.1 for some elements and were taken from literature [2]. Parameters for other investigated materials were obtained from a linear interpolation of these A, m and n over the mass density [21]. Typical Makhovian profiles for various E_+ are plotted for Cu in figure 2.6. Obviously, the broadening of $P(z, E_+)$ increases with E_+.

Positron Diffusion

Thermalized positrons diffuse through the solid until getting trapped in a defect or annihilating. The positron diffusion length L_+ in an ideal crystal is defined by

$$L_+ = \sqrt{D_+ \tau_\mathrm{b}} \tag{2.20}$$

with a diffusion coefficient D_+ of typically $1\,\mathrm{cm}^2/\mathrm{s}$ [7]. The diffusion is dominated by quasielastic scattering with acoustical phonons [69]. Exemplarily, L_+ is around 120 nm in annealed Cu [70] or 240 nm in a monocrystalline Si wafer [58]. When defects trap positrons at a rate $\kappa = \mu c$, the effective, reduced bulk lifetime $\tau_\mathrm{eff} = (\lambda_b + \kappa)^{-1}$ replaces τ_b in equation 2.20 and shortens the diffusion length. This enables the determination of defect concentrations from values measured for L_+.

The positron diffusion length L_+ is accessible in depth dependent DBS, where S is measured as function of the incident positron energy E_+. Thus, so-called $S(E_+)$ depth profiles are obtained which detect a transition from annihilation at the surface to annihilation in the bulk of a sample with increasing E_+. Annihilation at the surface leads to a characteristic S-parameter S_{surf}, whereas positrons in the bulk annihilate with S_{bulk}. In many cases, S_{surf} and S_{bulk} are a superposition of S-parameters characteristic for various positron states at the surface and in the bulk. The expression

$$J(E_+) = \int_0^\infty \exp[-z/L_+]\ P(z, E_+)\ \mathrm{d}z \tag{2.21}$$

describes the probability $J(E_+)$ of positrons implanted at an kinetic energy E_+ for diffusing back to the surface prior to annihilation or capture in defects [71]. At high values of L_+, i. e. in the case of defect-poor samples, this probability is maximal. Due to the back diffusion, the $S(E_+)$ depth profiles detect a superposition

$$S(E_+) = S_{\mathrm{surf}} J(E_+) + S_{\mathrm{bulk}}\,[1 - J(E_+)] \tag{2.22}$$

of the characteristic S-parameters S_{surf} and S_{bulk}. By fitting $S(E_+)$ profiles following equations 2.21 and 2.22, one can determine the positron diffusion length L_+ in order to measure defect concentrations as performed, e. g., in [72]. Equation 2.22 describes $S(E_+)$ depth profiles by only accounting for thermal positrons. For a more precise extraction of L_+, also non-thermalized positrons annihilating in the surface region can be accounted for [50], which was investigated outside the present work in previous studies [58, 70].

$S(E_+)$ depth profiles are well suited for the investigation of thin film systems as well. An investigation of topmost films thicker than around 300 nm is relatively simple because then for a wide range of low incident energies E_+ only annihilation at the surface and in the bulk of the film has to be considered. For systems consisting of several thin films the situation gets far more complex. In the case of a stack consisting of N homogeneous thin films, annihilation in several films contributes to the measured $S(E_+)$ depth profile described by

$$S(E_+) = \sum_{i=1}^{N} T_i\,(E_+)\,S_i + \left[1 - \sum_{i=1}^{N} T_i\,(E_+)\right] S_{\mathrm{surf}} \tag{2.23}$$

as superposition of S-parameters S_i characteristic for each layer i and S_{surf}. At a certain energy E_+, S is given by the implantation profile and its broadening due to diffusion with layer dependent diffusion lengths $L_{+,i}$. Thus, the fractions of positrons annihilating in the various layers T_i can be determined neglecting effects of positrons annihilating at interfaces. In the community, for a routine and quick analysis of $S(E_+)$ depth profiles the software package VEPFIT [73] is commonly used. Its application on thin film systems was comprehensively investigated in a previous work [58].

2.4.2 Probing Thin Film Systems

Element specific CDBS with a slow positron beam demonstrates the potential of depth dependent PAS for the investigation of layered structures. This was exemplarily shown in previous studies for a vapor-deposited thin film system on a Si substrate [58, 62] and is presented in the following. A 180 nm thick Au film on top of a 480 nm Cu film was prepared as described in detail in [58, 62]. CDB spectra were recorded in dependence on the incident energy E_+. The ratio curves to a Cu reference are shown in figure 2.7 as function of the longitudinal momentum component p_L and the Doppler shift ΔE. Here, only the element specific High-Momentum Area (HMA) is considered. Annihilation at Au atoms is displayed by a characteristic CDB signature relative to Cu. This Au signature, represented by the red solid line of the Au reference, has a lower intensity in the HMA, a minimum at $21 \cdot 10^{-3}\,\mathrm{m_0c}$ and a broad maximum at $36 \cdot 10^{-3}\,\mathrm{m_0c}$.

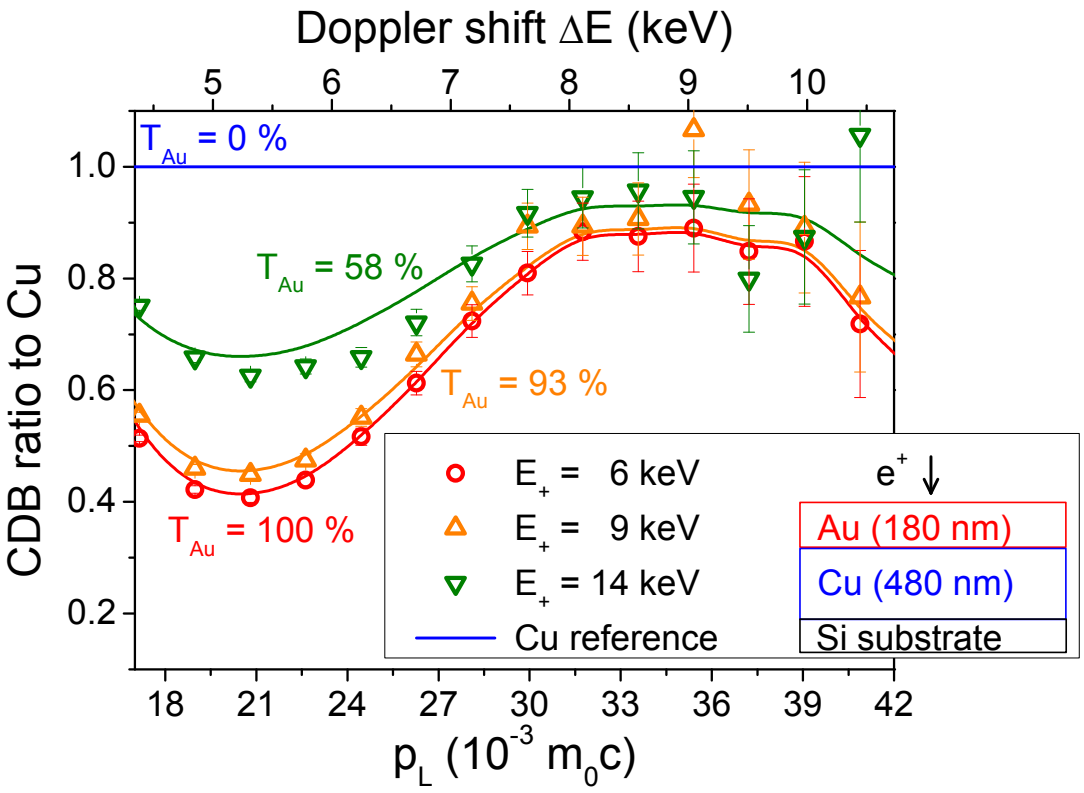

Figure 2.7: CDB ratio curves for various incident energies E_+ in the sketched bi-layer of Au and Cu; the reference is a Cu spectrum. The lines were calculated by a superposition of spectra for pure Au and Cu with the weighting factors $T_\mathrm{Au}(E_+)$ and $T_\mathrm{Cu}(E_+) = 1 - T_\mathrm{Au}(E_+)$ which are the fractions of positrons annihilating in the Au and Cu film (figure as published in [62] with minor adaptations).

For the lowest incident energies E_+ of 6 and 9 keV, quasi a pure Au signature is detected. For $E_+ = 14\,\mathrm{keV}$, the ratio curve approaches that of the Cu reference and thus, lies in between those characteristic of Au and Cu. Hence, the depth dependent behavior of the CDB spectra reflects the transition from annihilation in Au film to annihilation in a Cu film with increasing incident energy E_+. More precisely, the detected spectra are explained by the depth distribution of the annihilating positrons. This distribution determines the fractions of positrons $T_{\mathrm{Au}}(E_+)$ and $T_{\mathrm{Cu}}(E_+)$ annihilating in the Au or Cu film. These fractions could be calculated, since the positron diffusion lengths in the investigated system were known from previous studies [58, 70]. Thus, $T_{\mathrm{Au}}(E_+)$, given in figure 2.7, and $T_{\mathrm{Cu}}(E_+)$ were obtained by modeling the implantation and diffusion with VEPFIT. The implantation profile was based on a Makhovian profile which is adapted for thin film systems in order to account for the boundary condition of a continuous transmission of the positrons at the interfaces and the density dependence of the positron stopping power [73]. For all evaluated E_+, diffusion of positrons to the surface or into the substrate only plays a minor role. Using the determined fractions for superposing the Au and Cu reference spectra, which were both measured in vapor deposited films, yielded the solid lines in figure 2.7. They well describe the observed transition between the Au and Cu reference. Hence, an extended Makhovian model for layered structures as implemented within VEPFIT is well suited for describing positron implantation in layered structures. Similar findings were also reported in literature [74]. These results demonstrate the high capability of slow positron beams for probing thin film systems.

Chapter 3
3 Calculation of CDB Spectra

The interpretation of PAS experiments is facilitated and supported by the calculation of positron states in solids and their annihilation characteristics defined by the electronic structure. In order to calculate CDB spectra and positron lifetimes for the systems investigated in this thesis, the MIKA Doppler software package [6, 75] developed at Aalto University in Finland was used. In this chapter, the theoretical background of the calculations is briefly sketched. Furthermore, the principal methods of MIKA Doppler are shortly described and its application is demonstrated by the calculation of CDB spectra for pure elements as published in [76] and a bimetallic alloy as published in [62].

3.1 Theory of Electron-Positron Annihilation in Solids

In CDBS, the projection of the momentum distribution $\rho(\mathbf{p})$ of the annihilating electron-positron pair onto one dimension

$$\rho(p_{\mathrm{L}}) = \int\int \mathrm{d}p_{\mathrm{x}}\ \mathrm{d}p_{\mathrm{y}}\ \rho(\mathbf{p}) \tag{3.1}$$

leads to the observed Doppler shift $\Delta E = \frac{1}{2} p_{\mathrm{L}} c$ described in section 2.1 [2, 4]. Here, p_{x} and p_{y} denote the momentum components transversal to p_{L}. The function $\rho(\mathbf{p})$ can be calculated in the simple approximation of an Independent Particle Model (IPM) by

$$\rho(\mathbf{p}) = \sum_j \rho_{\mathrm{j}}(\mathbf{p}) = \pi \mathrm{r}_0^2 \mathrm{c} \sum_j \left| \int \mathrm{d}\mathbf{r}\ \exp(-i\mathbf{p}\cdot\mathbf{r})\ \psi_+(\mathbf{r})\psi_j(\mathbf{r}) \right|^2 \tag{3.2}$$

where $\psi_+(\mathbf{r})$ is the positron wavefunction, $\psi_j(\mathbf{r})$ the wavefunction of the occupied electron states j and the constant r_0 the classical electron radius [2]. It must be summed over all electron orbitals j in order to obtain $\rho(\mathbf{p})$. For determining positron lifetimes as measured

by PALS, the annihilation rate λ is obtained from

$$\lambda = \sum_j \lambda_\mathrm{j} = \pi \mathrm{r}_0^2 \mathrm{c} \int \mathrm{d}\mathbf{r}\; n_+(\mathbf{r})\, n_-(\mathbf{r})\, g(0, n_+, n_-) \tag{3.3}$$

as the sum over the orbital annihilation rates λ_j [2]. The electron density

$$n_-(\mathbf{r}) = \sum_{\varepsilon_j \leq \varepsilon_f} |\psi_j(\mathbf{r})|^2 \tag{3.4}$$

is given by all occupied states, i. e., with energies ε_j smaller than the Fermi energy ε_f. The positron density $n_+(\mathbf{r})$ can be calculated in an analogous way by considering

$$n_+(\mathbf{r}) = \sum_i^{N_+} |\psi_{i,+}(\mathbf{r})|^2 . \tag{3.5}$$

for all occupied positron states i. In usual experiments, only one positron exists in the sample at a given time and thus, $N_+ = 1$. Equation 3.3 already accounts for many-body electron-positron correlations within a Local-Density Approximation (LDA) by the pair correlation functional $g(0, n_+, n_-)$ at the position of the positron. The term describes effects of many-body electron-positron interactions like the screening of the positron by electrons. Thus, additional to the single-particle wavefunctions $\psi_+(\mathbf{r})$ and $\psi_j(\mathbf{r})$, a model for describing electron-positron interactions is required in order to determine the most important PAS observables in defect spectroscopy.

Basis for practical calculations is a two-component Density Functional Theory (DFT) ansatz [77], where the ground state energy $E[n_-, n_+]$ of a system of electrons and positrons is minimized as function of the electron density $n_-(\mathbf{r})$ and positron density $n_+(\mathbf{r})$ [2, 4]:

$$\begin{aligned} E[n_-, n_+] = F[n_-] + F[n_+] \quad & \overbrace{- \int \mathrm{d}\mathbf{r} \int \mathrm{d}\mathbf{r}'\; \frac{n_-(\mathbf{r}) n_+(\mathbf{r}')}{|\mathbf{r} - \mathbf{r}'|}}^{\text{electrostatic electron-positron interaction}} \\ \underbrace{+ \int \mathrm{d}\mathbf{r}\; V_\mathrm{ext}(\mathbf{r})[n_-(\mathbf{r}) - n_+(\mathbf{r})]}_{\text{interaction with external potential } V_\mathrm{ext}} \quad & \underbrace{+\; E_c^{e-p}[n_+, n_-]}_{\text{electron-positron correlation}} \end{aligned} \tag{3.6}$$

Here, the third and fourth term describe Coulomb interactions with $V_\mathrm{ext}(\mathbf{r})$ formed by the positively charged nuclei. $E_c^{e-p}[n_+, n_-]$ is the electron-positron correlation energy and incorporates many-body electron-positron interactions. In equation 3.6,

$$F[n_\pm] = T[n_\pm] \; \underbrace{+ \frac{1}{2} \int \mathrm{d}\mathbf{r} \int \mathrm{d}\mathbf{r}'\; \frac{n_\pm(\mathbf{r}) n_\pm(\mathbf{r}')}{|\mathbf{r} - \mathbf{r}'|}}_{\text{Hartree term}} \; + \; E_{xc}[n_\pm] \tag{3.7}$$

is the one-component functional of electrons and positrons as denoted by the respective superscripts. The kinetic energy $T[n_\pm]$ of non-interacting particles (of the same kind), electrostatic interactions between these particles, described by the Hartree term, and their exchange-correlation energy $E_{\mathrm{xc}}[n_\pm]$ contribute. From equation 3.6, single particle Schrödinger equations for $\psi_+(\mathbf{r})$ and $\psi_{\mathrm{j}}(\mathbf{r})$ can be derived, which are given in references [2, 4, 77]. For the positron, the respective equation is

$$-\frac{1}{2}\nabla^2\psi_+(\mathbf{r}) \;+\; V_{eff}(\mathbf{r})\psi_+(\mathbf{r}) \;=\; \varepsilon_+\psi_+(\mathbf{r}) \tag{3.8}$$

with the positron energy ε_+ and the effective potential

$$V_{eff}(\mathbf{r}) = \underbrace{\int \mathrm{d}\mathbf{r}' \frac{-n_-(\mathbf{r}') + n_+(\mathbf{r}') + n_{\mathrm{ext}}(\mathbf{r}')}{|\mathbf{r}-\mathbf{r}'|}}_{\text{Coulomb interactions}} \;+\; \frac{\delta E_{xc}[n_+]}{\delta n_+(\mathbf{r})} \;+\; \frac{\delta E_c^{e-p}[n_+, n_-]}{\delta n_+(\mathbf{r})} \tag{3.9}$$

that describes Coulomb interactions with electrons, positrons and the charge density $n_{\mathrm{ext}}(\mathbf{r})$ arising from $V_{\mathrm{ext}}(\mathbf{r})$. Moreover, the last two terms account for exchange interactions and electron-positron correlations. The Schrödinger equations and equations 3.4 - 3.5 have to be solved self-consistently for electrons and positrons. A complete treatment of the electron-positron annihilation within the two-component DFT remains challenging and thus, for calculations, which accompany experimental PAS studies on open volume defects, simplifications are commonly used such as implemented in MIKA Doppler.

3.2 Calculations with MIKA Doppler

The MIKA Doppler code calculates positron states, lifetimes and CDB spectra following the DFT ansatz described above in the limit of a vanishing positron density. Initially, the electron wavefunctions $\psi_{\mathrm{j}}(\mathbf{r})$ in the solid are calculated by a superposition of atomic wavefunctions [78], which are obtained from considering the Dirac equation for free atoms. In this simplification, electron wavefunctions are not self-consistent. Moreover, possible deformations of $\psi_{\mathrm{j}}(\mathbf{r})$ due to the positron are not accounted for. This is fully justified for a delocalized positron state. Even in the case of vacancies, which cause a high localized positron density, the simple approach can be expected to work well due to a countering behavior of the enhancement factor with increasing density [79].

The orbital annihilation rates λ_{j} are obtained by solving the Schrödinger equation 3.8 for the positron using a 3D real space solver in an IPM approximation and assuming a vanishing positron density. In the used limit, the factor $g(0, n_+, n_-)$[1] is denoted by γ and known as enhancement factor of the electron density at the positron; $\gamma = 1$ for the IPM in

[1] The dependency of $g(0, n_+, n_-)$ on the crystal momentum $\mathbf{k}$ of the electronic states is not considered, since it only plays a minor role for CDB spectra [4].

the simplest approximation. For a proper consideration of electron-positron correlations, several parametrizations for γ within LDA or the Generalized Gradient Approximation (GGA) schemes can be chosen in MIKA Doppler. This means that effects of electron-positron interactions are included after solving the Schrödinger equation for the calculation of the annihilation rate λ in equation 3.3. For all available models, the enhancement γ is evaluated as function of the local electron density. In this thesis, a GGA approach [80] was chosen for the determination of γ in most cases and a LDA approach was applied for MnSi. The used functions for γ are given in the section 'Enhancement Factors' of the appendix. Obtained values for the positron lifetime depend on the chosen model and vary in a range of around 10 ps for defect free materials and 20 ps for vacancies.

Finally, the momentum distributions $\rho(\mathbf{p})$ are calculated in order to simulate CDB spectra. For this purpose, equation 3.2, which describes $\rho(\mathbf{p})$ in an IPM, is adapted in order to include effects of the enhancement:

$$\rho(\mathbf{p}) = \sum_j \rho_\mathrm{j}(\mathbf{p}) = \pi \mathrm{r}_0^2 \mathrm{c} \sum_j u_j^2 \left| \int \mathrm{d}\mathbf{r} \, \exp\left(-i\mathbf{p}\cdot\mathbf{r}\right) \; \psi_+(\mathbf{r})\psi_j\left(\mathbf{r}\right) \right|^2 \tag{3.10}$$

For each orbital, the respective momentum distribution $\rho_\mathrm{j}(\mathbf{p})$ is weighted by the state dependent enhancement factor

$$u_j^2 = \frac{\lambda_j}{\lambda_j^{\mathrm{IPM}}} \tag{3.11}$$

obtained from the ratio of orbital annihilation rates. Here, λ_j denotes the annihilation rate in a model with enhancement, i. e. $\gamma \neq 1$, and λ_j^{IPM} is the IPM rate. In MIKA Doppler, a parametrized positron wavefunction based on an error-function of the distance from the atomic center is used for $\psi_+(\mathbf{r})$ in equation 3.10. Applying different enhancement models only slightly affects the shape of calculated CDB spectra. The simulated spectra are obtained within the MIKA package after a projection according to equation 3.1.

3.3 Case Studies with MIKA Doppler

Transition Metals

First calculations with the MIKA software for pure elements were already conducted within previous studies outside this work [58]. However, for elements with 4f electrons, e. g. Au, unrealistic results were obtained. This problem was reported to Ilja Makkonen from Aalto university, who identified a software bug and managed to fix it. Thus, MIKA Doppler could be used for the calculation of PAS observables for all investigated materials. In order to demonstrate the ability of this software for the reliable determination of the elemental specific high momentum area of CDB spectra, a case study on transition metals, namely Au, Cr, Cu, Ni, Pt and Si, was performed as published in [76]. The measured CDB

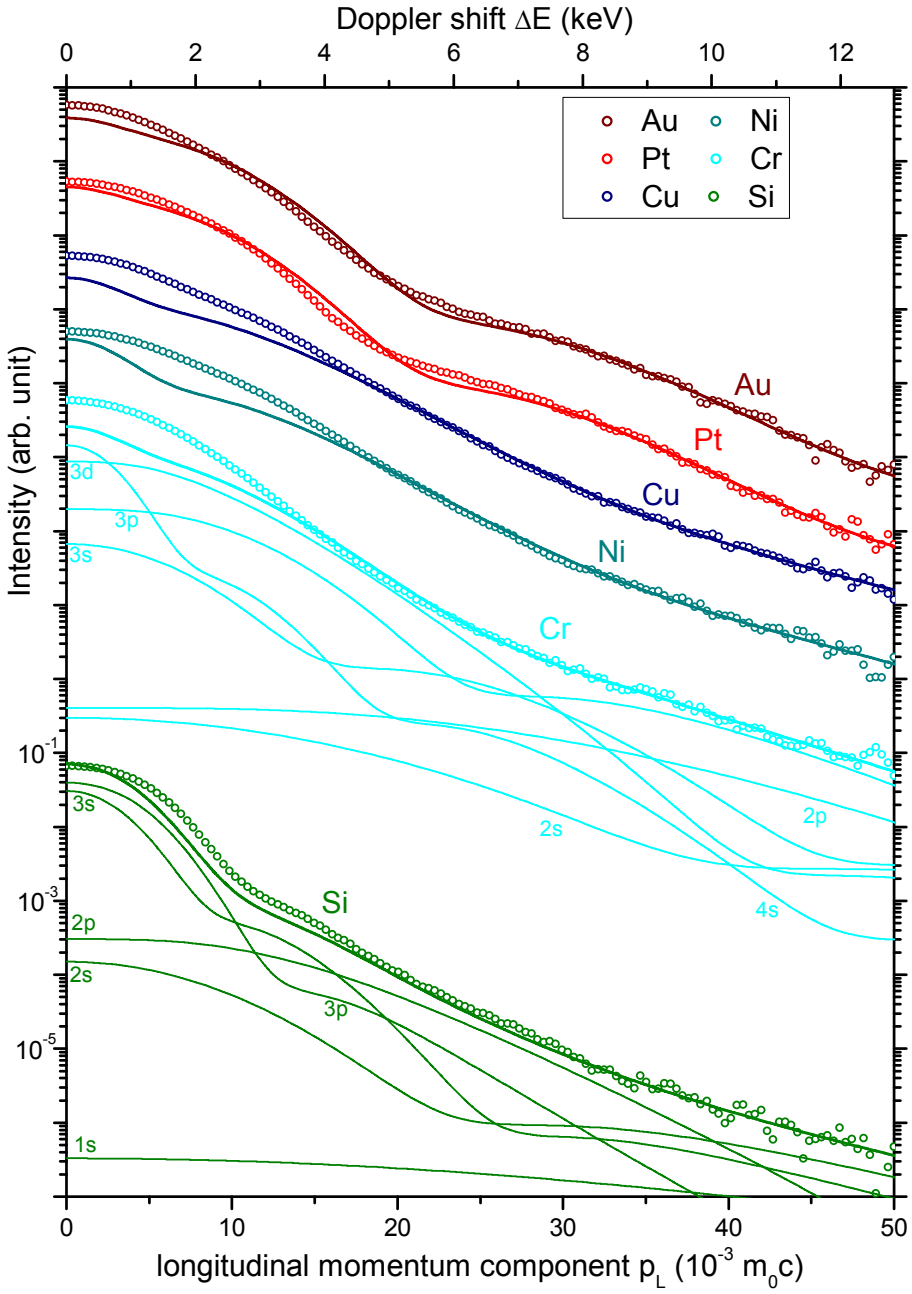

Figure 3.1: Waterfall plot of measured (∘) and calculated (–) CDB spectra for various elements. In the case of Si and Cr, for each electron orbital the respective contribution to the CDB spectra is plotted (published in [76]).

spectra were taken from previous studies [58,66]. More than 10^7 counts were accumulated in the coincident photopeak for each spectrum with an effective energy resolution of 1.0 - 1.1 keV FWHM at 511 keV. The software developed by Pikart [66, 67] was used for the

data evaluation. The proper functioning of its novel algorithm for the data analysis was demonstrated in [66], amongst other methods, by comparing experimental data to the spectra calculated within this work for Au, Cu and Si.

The measured and calculated spectra are shown in figure 3.1. The calculated ones were convolved with a Gaussian in order to account for the experimental energy resolution. Moreover, they were multiplied by a scaling factor, which was obtained by evaluating the error weighted mean ratio of measured to calculated spectra for high momenta $30 \leq p_L \leq 50 \cdot 10^{-3}\, m_0 c$ mainly caused by annihilation with inner shell electrons [81–84]. In this region, the applied superposition method for atomic electron wavefunctions is expected to work reliably. Concurring with this expectation, a good quantitative agreement is found for all elements at high momenta. For lower momenta, the higher contribution of valence electrons, which are not well described by the superposition method, leads to less agreement. In Si, e. g., this is the case for 3s and 3p-electrons: Their non-isotropic momentum distributions [85] cannot be obtained from the superposed electron wavefunctions of free atoms. Discrepancies for low momenta are also found for Cr, Cu and Ni, where on the one hand the momentum distribution is underestimated in the present calculations and on the other hand the signatures are only roughly described by the calculated spectra. For these elements, the individual contribution of the various electron orbitals is similar and

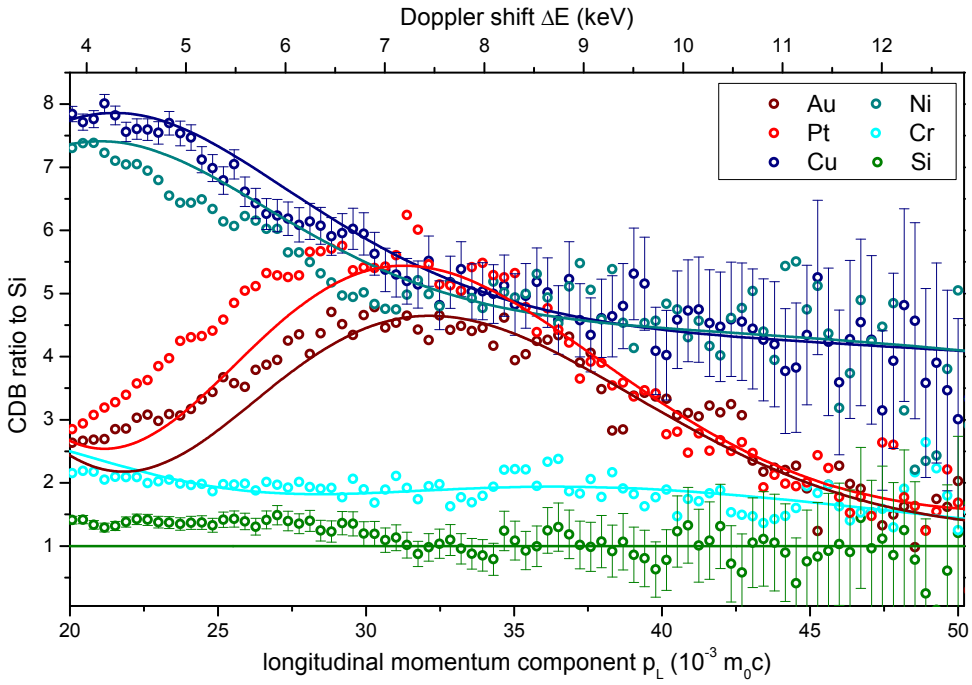

Figure 3.2: Measured (∘) and calculated (–) CDB ratio curves of various elements for high momenta. The calculated spectrum of Si was used as CDB reference (published in [76]).

exemplarily shown for Cr in figure 3.1. The calculated spectra of Au and Pt exhibit similar features as the measured ones in the whole momentum range. These features cannot be attributed to a single electronic shell, because three or more different shells contribute to a similar extent to the momentum distribution in the whole range.

In figure 3.2, the respective CDB ratio curves of all investigated elements are shown in the high momentum area. Here, the spectrum calculated for Si was used as reference. The excellent agreement for Cr, Cu and Ni between measurements and calculations is noteworthy. Exemplarily, a nearly identical decrease between $20{\cdot}10^{-3}\,\mathrm{m_0c}$ and $50{\cdot}10^{-3}\,\mathrm{m_0c}$ is found for both the measured and calculated ratio curve of Cu. A study based on band structure calculations revealed that valence orbitals are dominant for $p_\mathrm{L} < 30 \cdot 10^{-3}\,\mathrm{m_0c}$ [86]. In that study, the 3d band was attributed to the valence orbitals. Here it is seen, that the treatment of the 3d band as core orbital by the atomic superposition of the respective electron wavefunctions describes the experimental data for $p_\mathrm{L} > 20 \cdot 10^{-3}\,\mathrm{m_0c}$ very well. A similar agreement of calculations based on the superposition was reported in other studies on Cu [84,86,87]. Thus, it seems justified to treat the 3d band of Cr, Cu and Ni as core orbital in the calculation of PAS observables. For Au and Pt, the calculations cannot fully describe the data. However, theoretical and experimental ratio curves clearly show a similar signature with the characteristic maximum at around at $31 \cdot 10^{-3}\,\mathrm{m_0c}$. It is concluded that the use of the MIKA Doppler software with its approximations is well suited for the investigation of the element specific signatures at high Doppler shifts.

Au-Cu Alloy

In the second study, MIKA Doppler was used for the investigation of an Au-Cu alloy formed in a Au-Cu bilayer system (see section 2.4.2) by depth dependent CDBS. The alloying of the thin films took place during tempering as observed by in-situ CDBS [58,62]. The Au content of the alloy was estimated by analyzing the High Momentum Area (HMA) of the experimental CDB spectra and comparing it to theoretically calculated spectra. For this purpose, the disordered fcc phase $\mathrm{Au_xCu_{1-x}}$ was modeled within a supercell of $5{\times}5{\times}5$ unit cells and a mesh of $128 \times 128 \times 128$ grid points. The Au content x was varied between 0.2 and 0.9 taking into account the varying lattice parameter with data given by Okamoto [88]. Thus obtained theoretical spectra were, as routinely done, convolved with a Gaussian in order to account for the limited experimental energy resolution. Then, they were compared to the measured spectra in the HMA for $17 \leq p_\mathrm{L} \leq 42 \cdot 10^{-3}\,\mathrm{m_0c}$. The scaling factor for each theoretical spectrum was, as introduced in the previous study, obtained by analyzing the measured and theoretical spectra and calculating their respective error weighted mean ratio in the HMA. For this comparison, two experimental spectra recorded at 410 °C and 460 °C were used. In figure 3.3, the ratio curves of the latter spectrum and the calculated ones are shown using a Cu reference.

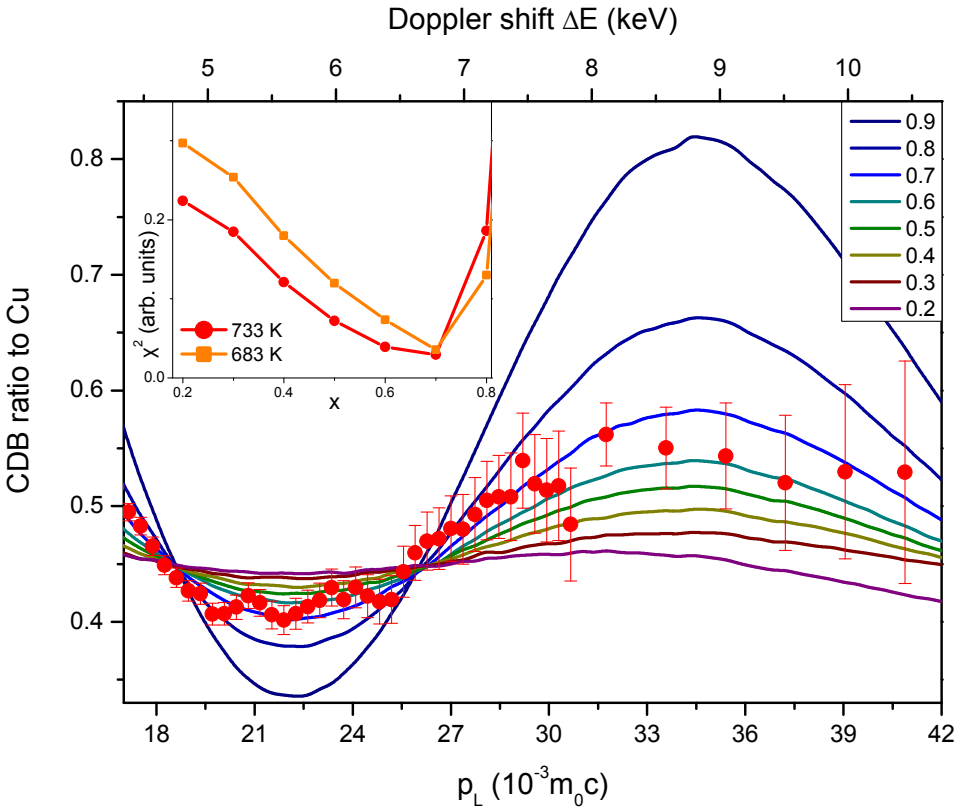

Figure 3.3: Comparison of the CDB spectra calculated for Au_xCu_{1-x} (solid lines) with the spectrum measured in a Au-Cu alloy at 460 °C (symbols). The inset shows $\chi^2(x)$ as a measure for the agreement between measured and calculated spectra. A similar result was obtained by the comparison at 410 °C (published in [62]).

For high Cu contents, a flat ratio curve without a pronounced signature compared to the Cu reference is obtained. Thus, as expected, the CDB spectrum is characteristic for Cu. With an increasing Au content, the CDB ratio curves exhibit a more and more pronounced minimum at around $22 \cdot 10^{-3}$ m_0c and a maximum at $35 \cdot 10^{-3}$ m_0c. These are most distinct for the highest Au content. They are in good agreement with the CDB spectrum of the pure Au film in the original Au-Cu bilayer shown in figure 2.7. Thus, a transition from a CDB signature characteristic for Cu to that for Au was found with increasing Au content. This finding reveals that MIKA Doppler is well suited for the calculation of CDB spectra of binary systems. The deviation of the theoretical from the experimental spectra was evaluated by the determination of χ^2, which is the error weighted sum over the square of the differences between the theoretical values and experimental data points in the HMA. As shown in the insert in figure 3.3, χ^2 as function of the Au content x exhibits a minimum at 0.7. A very similar result was obtained at 410 °C. Hence, according to the CDBS results, the Au content x in the alloy could be determined to be around 0.7.

Chapter 4

4 Coincident Doppler Broadening Spectroscopy at NEPOMUC

The NEPOMUC positron beam [9–11] at the research reactor FRM II enables unique PAS experiments due to its high intensity and brightness. Measurements can be conducted rapidly within one minute for a DBS spectrum and four hours for a CDBS spectrum with high lateral resolution. The existing apparatus, developed by Stadlbauer and Pikart [12,66], was set into re-operation in 2013 after an upgrade of the positron beam tube SR 11 at the FRM II. An important step prior to restarting the routine operation was adjusting the focusing system in the spectrometer in order to provide a high lateral resolution in the whole range of incident positron energies. With these changes, the reliable investigation of the relatively small MnSi and YBCO specimens presented in the following chapters became feasible. Moreover, a new sample heating device [14] was designed and installed in order to make a wider range of temperatures accessible for in-situ measurements with the high intensity beam. Finally, a new system of two pixelated HPGe detectors was installed and successfully run which enables the 3D detection of electron momenta for the first time.

4.1 The CDB Spectrometer at NEPOMUC

The NEPOMUC Positron Beam

The NEPOMUC positron source is installed at a beam tube of the research reactor FRM II. A sketch of the in-pile element in the reactor pool is shown in figure 4.1. At the tip of the beam tube in a cap made of highly enriched ^{113}Cd, thermal neutrons are converted into high-energetic γ-radiation. In the beam tube, the so-called 'experimental tube' is installed. This device is evacuated to UHV conditions and contains the so-called 'potential tube'. At the front of this tube, the positrons are generated in Pt foils which have a high efficiency for production of electron-positron pairs from the high-energetic γ-radiation. Only a part

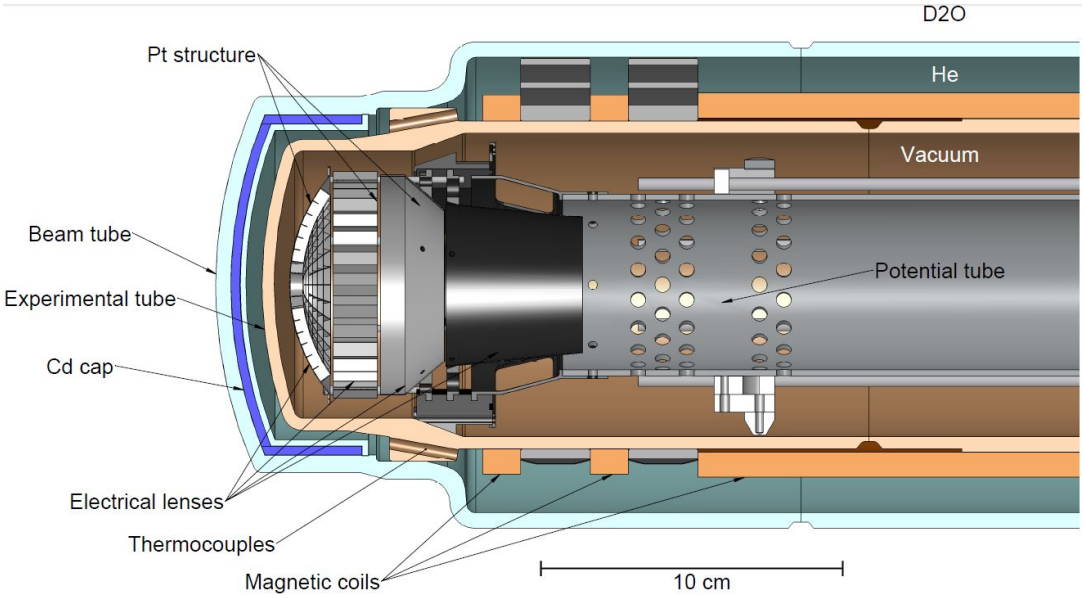

Figure 4.1: Cross-sectional, sketched view of the NEPOMUC beam tube at the research reactor FRM II (figure taken from [10]).

of the generated positrons is used for the formation of the beam; these are the thermalized or so-called moderated positrons which are emitted from Pt due to its negative positron work function [89]. In the electric field of an electrostatic lens system, these positrons enter the magnetic field of solenoids and form the NEPOMUC positron beam. The solenoidal magnetic field serves as guiding field for the positrons. The thus generated positron beam, also denoted as primary beam, has a kinetic energy of around 1 keV and an intensity of $1.1 \cdot 10^9$ moderated positrons per second, which is world record [10].

A component of high importance for further increasing the beam quality is the so-called remoderator [90, 91]. This device is located in the experimental hall of the FRM II close to the first accessible point of the positron beam line. Here, the brightness of the beam can be enhanced by the non-adiabatic technique of remoderation [54]. For this purpose, the positrons are implanted into a W single crystal where they loose almost their total kinetic energy by thermalization. A part of the thermalized positrons diffuses back to the surface as described in section 2.1 and is emitted with low kinetic energies of around 2.8 eV as given by the positron work function of W [92]. These positrons, denoted as remoderated positrons, are extracted by an elaborated magnetic field and form the remoderated beam. This beam has a kinetic energy of around 20 eV, an intensity of $3.0 \cdot 10^7$ remoderated positrons per second [10] and a brightness around 30 times higher than the primary beam [9]. The remoderated beam was used for all (C)DBS experiments presented in this thesis.

The CDB Spectrometer

The CDB spectrometer at NEPOMUC was designed by Stadlbauer [12] in order to perform depth dependent (C)DBS with high lateral resolution and within short measurement times. Figure 4.2 shows a sketch of the main part of the sample chamber, which is evacuated to UHV conditions. Positrons leave the magnetic guiding field of the beam line by passing a magnetic field termination and then enter the chamber from the top through an aperture. An electrostatic lens system installed below the aperture focuses the beam onto the specimen. The system consists of four lenses, which are biased at voltages down to -3 kV. The samples can be biased at voltages down to -30 kV which allows to vary the incident positron energy E_+ between 0.25 and 30 keV. The voltage U_4 applied at 'lens 4', which is the last one in front of the sample, is adjusted in dependence on E_+. An additionally installed component for optimizing the field geometry is the so-called potential plate, which is a circular plate of Al with an aperture in its center, located a few mm above the sample and biased at the sample voltage.

Two pairs of HPGe detectors are arranged in a collinear setup around the sample chamber for detecting the energy of the annihilation radiation in single or coincident mode. These coaxial detectors, described in detail by Pikart [66], are equipped with a transistor reset preamplifier which is designed for measurements with good energy resolution at high countrates. Their specified resolution amounts to around 1.4 keV FWHM at a γ-energy

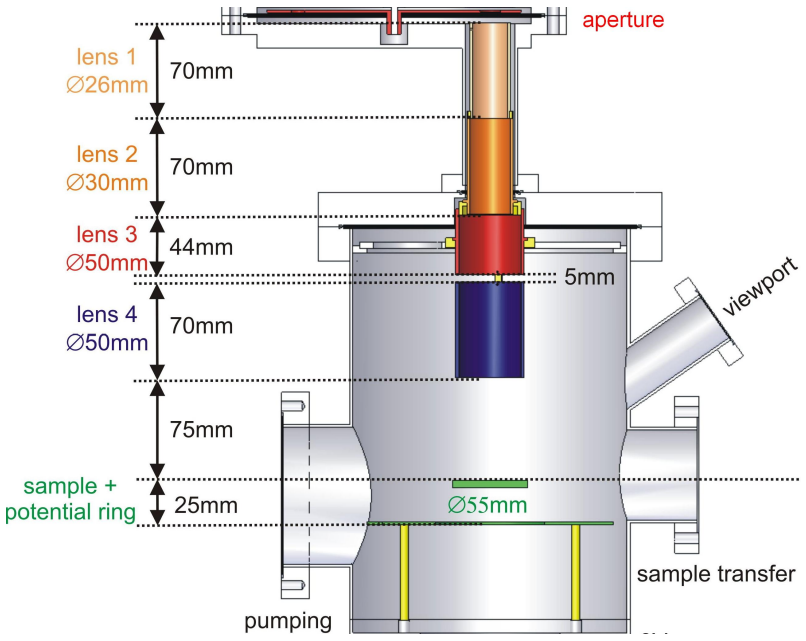

Figure 4.2: Cross-sectional sketch of the sample chamber at the NEPOMUC CDB spectrometer. Positrons enter through the aperture from the top (figure taken from [12]).

of 511 keV. During operation in the experimental hall of the FRM II, this value can be larger due to high countrates, electronic noise from neighboring instruments, ground loops or systematic errors in the detection of the γ-energy. Typical disturbances in the detected spectra are described in the section 'Data Quality' of the appendix. Within the present work, the electrostatic insulation of the detection system was improved in order to ensure the stable operation of the HPGe detectors at a high performance. The improvements included the integration of galvanically isolated COM ports for the hardware control of the spectrometer and a separate connection of the detection system to the power supply in the experimental hall of the FRM II.

A careful analysis of the recorded data allows one to minimize the influence of external disturbances on the (C)DBS spectra. During DBS measurements, the stable operation of the detection system can be tracked by the analysis of the lineshape parameters S and W. Especially the latter one is sensitive to changes in the background or the detection system. Thus, if the repetition of measurements yields the same S- and W-parameters, it is concluded that the respective data are reliable and can be further interpreted. Moreover, the evaluation of DBS and CDBS must give a consistent picture if changes are detected and both techniques are sensitive to these changes. In CDBS experiments, the effective energy resolution of the detection system is obtained within the data evaluation [66] and – as long the detection system is running stable – is constant. These indicators were applied for the identification of valid spectra in the experimental studies presented in the following chapters. In this way, high-quality data were obtained. Exemplarily, the quantitative analysis of different DBS and CDBS observables in the case of MnSi yielded results in very good agreement as can be seen in figure 5.6. Also in the case of YBCO, DBS and CDBS results are consistent. Moreover, the repetition of depth dependent DBS after nearly one year gave very similar results as shown in figures 6.7 and 6.14.

4.2 Spatially Resolved Measurements

The design of the spectrometer enables measurements at a lateral resolution of up to 0.3 mm (FWHM) [12] and thus, the positron beam can be used for imaging. This prospect of the CDB spectrometer was important for numerous studies in the past, e. g., by Stadlbauer [15], Hugenschmidt [17] and Hengstler [20]. Laterally resolved measurements are performed by the use of a positionable sample holder. The holder is connected to a positioning unit of two stepper motors which enable the motion of the samples along two axes, denoted as X and Y. Two aspects are of high importance in order to reach an optimal spatial resolution and to perform depth dependent DBS even on relatively small samples: (i) The adjustment of the voltage U_4 at 'lens 4' for the chosen incident positron energy E_+, and (ii) the compensation for the shift of the beam spot observed at low values for

Figure 4.3: Cross-sectional, principal sketch of the transition between 'lens 3' and 'lens 4' (as defined in figure 4.2) in the original (left) and new (right) design, where the electric field in the lens system is not disturbed by a gap.

E_+ [12]. After the change of the NEPOMUC beam tube at the reactor in 2011, beam characteristics were improved and a new beam line system for guiding the positrons to the CDB spectrometer was constructed. Moreover, the design of the lens system was slightly changed in order to minimize the influence of external fields. The design changes are sketched in figure 4.3: Now, 'lens 4' is longer, thinner and fixed by an insulating ring at 'lens 3'. Thus, the former gap of 5 mm between 'lens 3' and 'lens 4' is avoided. Due to the described changes, the mentioned aspects relevant for focusing of the beam were reconsidered before performing the measurements described in the following chapters.

The dependence of U_4 on E_+ was investigated by performing simulations with the COMSOL multiphysics package. In this program, electric and magnetic fields in experimental set-ups can be calculated within a finite-element method. A so-called particle tracer can be used in order to calculate the trajectories of the positrons in these fields. The current version of the CDB sample chamber with the magnetic field determination at its entrance was implemented in COMSOL as model with cylindrical symmetry. The vertical position of the focal plane of the positron beam was studied. The position can be shifted by changing U_4; e. g. increasing U_4 causes the focus to move downwards to the bottom of the chamber. For all evaluated values of E_+, U_4 was chosen in order to obtain the focus on the sample surface. Thus obtained and previously used values for U_4 can be found in the section 'Lens Voltages' of the appendix.

The values simulated for U_4 were found to be optimal settings in experiments by scanning the beam over sharp edges between Al and Cu along the X- and Y-direction. The edges were prepared by Cu tapes sticked on the Al sample holder. An aperture of 3 mm diameter was used at the chamber entrance. Exemplarily, such a scan along the X-axis is shown in figure 4.4 at $E_+ = 4\,\mathrm{keV}$. The scan was performed two times, firstly with the old value for U_4 and then with the new value simulated for the current set-up. The $S(X)$ profile exhibits a transition at $X = 10\,\mathrm{mm}$ from S_{Cu} to S_{Al}, which are the S-parameters characteristic for the Cu tape and Al sample holder. This transition is clearly sharper for the new setting of 'lens 4' which demonstrates that the spatial resolution was significantly enhanced by

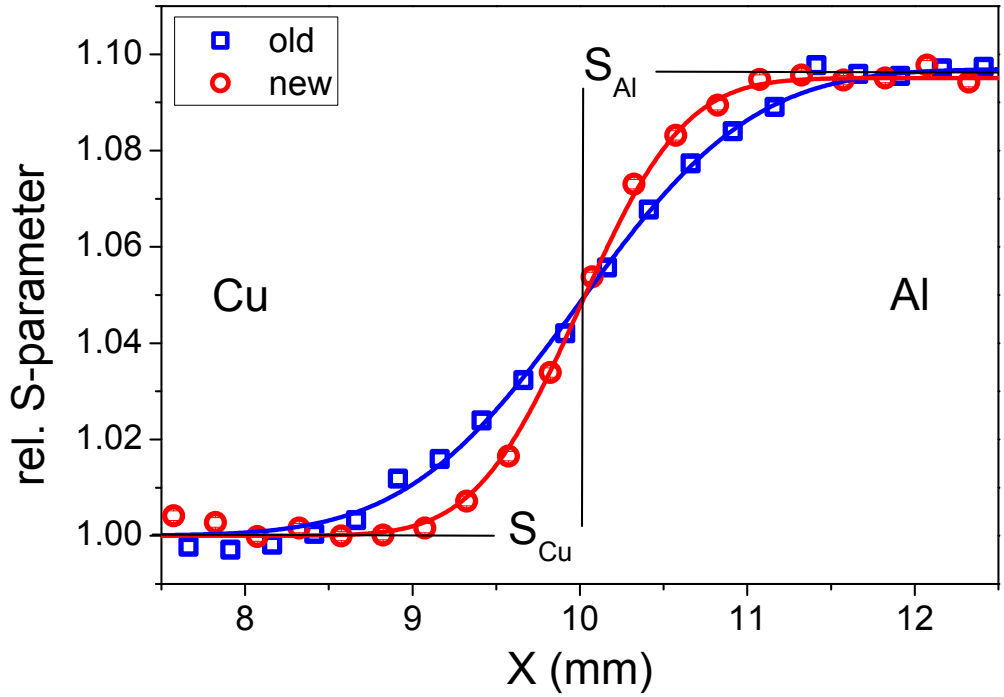

Figure 4.4: S-parameter as function of X obtained by scanning at an incident positron energy $E_+ = 4\,\mathrm{keV}$ over an edge between Cu and Al samples at $X = 10\,\mathrm{mm}$. Old and new, optimized settings of the lens system were applied. The relative S-parameters normalized to the characteristic S-parameter S_{Cu} are shown. The solid lines are fits to the data based on an error-function which yielded the beam spot diameter d_{FWHM} (figure 4.5).

the adaptation of U_4. Additionally, the scan was repeated for various values of U_4. It was confirmed that the value found by the simulations yielded the most narrow transition, which was also the case for all performed scans along X and Y at $1 \leq E_+ \leq 25\,\mathrm{keV}$.

The beam spot size d_{FWHM} was determined by performing least-square fits to the scan data. If a 2D Gaussian function describes the intensity distribution in the beam spot, then a scan over the edge between Cu and Al yields a profile with the shape of an error-function. Hence, the $S(X)$ profiles were fitted by

$$S(X) = \frac{S_{\mathrm{Al}} + S_{\mathrm{Cu}}}{2} + \frac{S_{\mathrm{Al}} - S_{\mathrm{Cu}}}{2} \cdot \mathrm{erf}\left(\frac{X - X_0}{\Delta X}\right) \tag{4.1}$$

with X_0 as X-coordinate of the edge, e. g. $X_0 = 10\,\mathrm{mm}$ for the scans shown in figure 4.4. The parameter ΔX measures the width of the transition from S_{Cu} to S_{Al} and was used for the determination of the beam spot diameter

$$d_{\mathrm{FWHM,X}} = 2\,\sqrt{\ln(2)}\;\Delta X \tag{4.2}$$

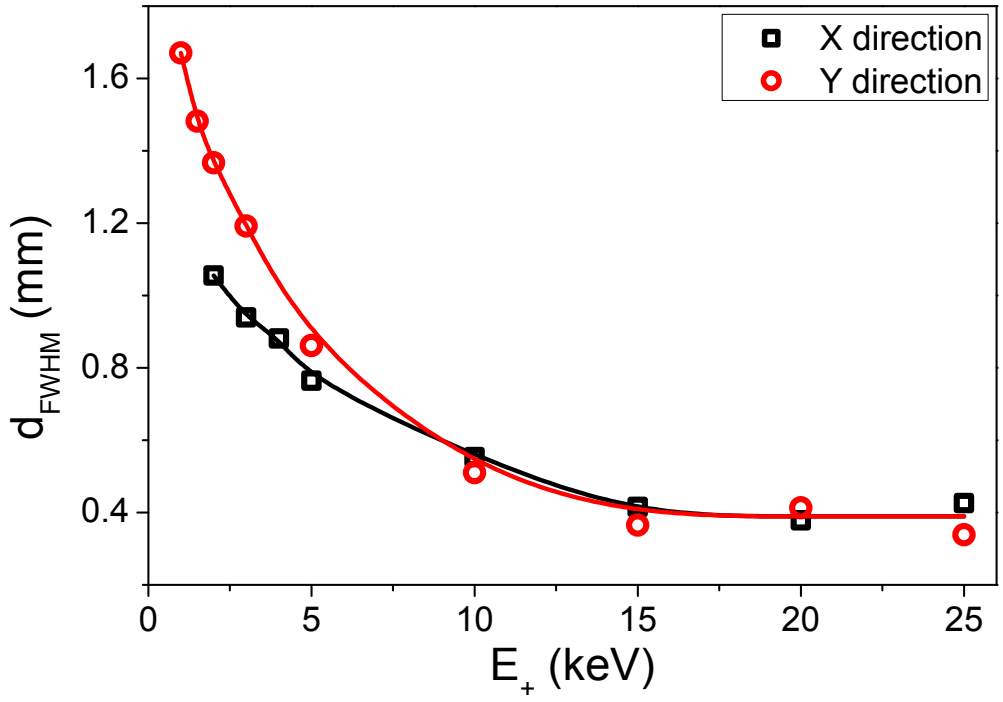

Figure 4.5: Measured beam spot diameter d_{FWHM} in the NEPOMUC CDB spectrometer along the two perpendicular axis X and Y as function of the incident positron energy E_+. The solid lines serve as guides to the eye.

along the X-axis. The resulting fits, represented by the solid lines in figure 4.5, excellently describe the measured $S(X)$ profiles. This agreement was also found for the investigated $S(Y)$ profiles which were fitted with the same procedure. Thus, the intensity distribution in the beam spot is assumed to have a Gaussian shape. The beam spot diameter on the sample is described by $d_{\mathrm{FWHM,X}}$ and $d_{\mathrm{FWHM,Y}}$, which were obtained as function of the incident energy E_+ as shown in figure 4.5. In their calculation it was additionally accounted for the fact that the beam spot follows the motion of the sample holder during scanning. This effect was quantified by measuring the width of the Cu tape in line scans and comparing the obtained value to its *true* width[1].

The found dependency of d_{FWHM} on the incident positron energy E_+ is a result of highest importance. It determines the minimum sample size for depth dependent (C)DBS at NEPOMUC. Obviously, even samples with a size of $3 \times 3\,\mathrm{mm}^2$ are measurable in a wide range of E_+. The minimal sample size is limited by the beam spot width at low E_+. In the case of small samples it was routinely proven by line scans at $E_+ = 2\,\mathrm{keV}$ that the beam spot only covers the sample. For high $E_+ \geq 15\,\mathrm{keV}$, the beam spot has an diameter of around 0.4 mm (FWHM) or even less. The presented characterization of the

[1]Scaling factors of 0.8 in X- and 0.6 in Y-direction were found.

beam spot size was done in August 2013 shortly after the operational start of the upgraded positron source NEPOMUC. At this time, the beam intensity at the CDB spectrometer was relatively low and an aperture of 3 mm diameter was used at the entrance of the CDB spectrometer. Since then, several improvements in the remoderation and transport efficiency at the beam line have increased the available countrate at the spectrometer. This has allowed to reduce the size of the aperture and currently, an aperture with 0.5 mm diameter is used. Hence, the here presented values for d_{FWHM} can be considered as upper limits for the beam spot size in the measurements presented in the following chapter.

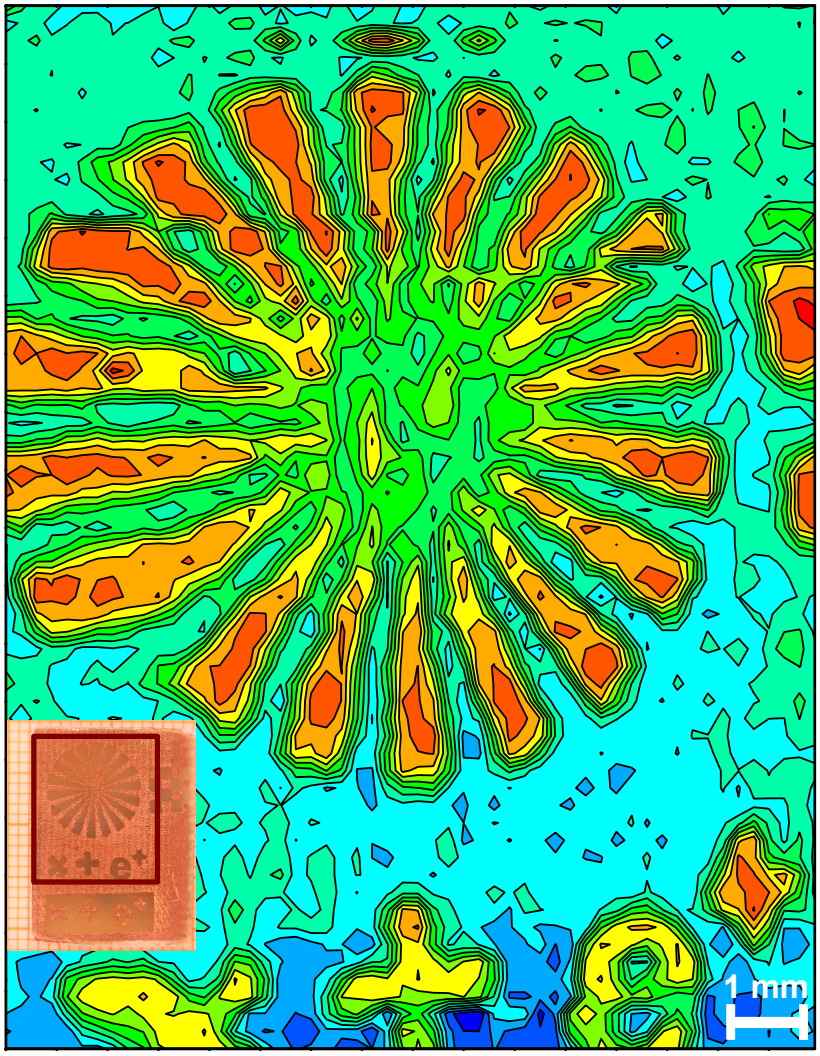

Figure 4.6: 2D S-parameter map at $E_+ = 30\,\mathrm{keV}$ of a Cu structure on a epoxy sheet, which is shown on the small photo. The map of the marked area was obtained from line scans from the left to the right with an aperture of 1 mm diameter and a magnet below the sample. Thus, structures as small as 0.4 mm are resolvable.

The beam spot can be further reduced by using smaller apertures or positioning an focusing magnet below the sample. The 2D S-parameter map of a conductor board with an elaborated design as shown in figure 4.6 was obtained by combining these approaches: An aperture of 0.1 mm diameter was applied and a small magnet installed below the sample. The map was generated from line scans in Y-direction at various values of X, the step size for both directions was 0.3 mm. The incident positron energy was set to $E_+ = 30\,\mathrm{keV}$. Evaluating the scan over the so-called Siemens star reveals that structures with a size of around 0.4 mm can be resolved in this map. This corresponds to $d_{\mathrm{FWHM}} \leq 0.2\,\mathrm{mm}$, which is lower than any other value reported for the spectrometer. It is noteworthy that the magnet only was found to reduce the beam spot at high incident energies. At lower energies, a higher lateral resolution was observed without the magnet.

The $S(X)$ and $S(Y)$ line scans, performed for investigating $d_{\mathrm{FWHM}}\,(E_+)$, displayed a beam shift for low incident positron energies E_+. This shift is attributed to residual magnetic fields in the sample chamber of the CDB spectrometer, which influence in particular the trajectories of positrons with low kinetic energies. Beyond the contribution of the magnetic field of the earth as discussed in [12], external fields could stem from neighboring experiments or components installed at the chamber, like vacuum gauges or magnetized parts. In each beam time, the shift was analyzed by line scans and corrected by adjusting the position of the sample holder when probing at low E_+. The following phenomena were observed in the recent years. The beam shift especially occurs in the Y-direction, which is orientated along the east-west direction. In this direction, at low E_+, the beam position must be corrected to smaller values in order to compensate the shift. The shift in Y is a monotonous function of E_+ and exceeds 2 mm for $E_+ < 5\,\mathrm{keV}$ and 5 mm for $E_+ < 1\,\mathrm{keV}$. In X, a shift was not always observed and anyway smaller than in Y.

4.3 In-situ (C)DBS at High Temperatures

From its beginning, the CDB spectrometer was used for (C)DBS in a wide temperature range. In order to access low temperatures, the sample holder can be mounted on the cold head of a liquid He closed-cycle cryostat as described in [12]. This cooling apparatus with the sample holder designed by Stadlbauer is currently put back into operation within a bachelor thesis. For in-situ DBS at high temperatures, a heating device for the samples was developed by Pikart [66], which is detailedly described in [93]. This device was successfully used by Oberdorfer [19], Hengstler [20] and for other previous works [58, 62, 70]. Within the present work, a new sample heater was developed in order to further increase the maximal temperature and ensure stable biasing of the heated sample at high voltage.

The constructed device, as sketched in figure 4.7, can be flanged at the bottom of the chamber. Its principal design is based on sample heaters previously used at the CDB

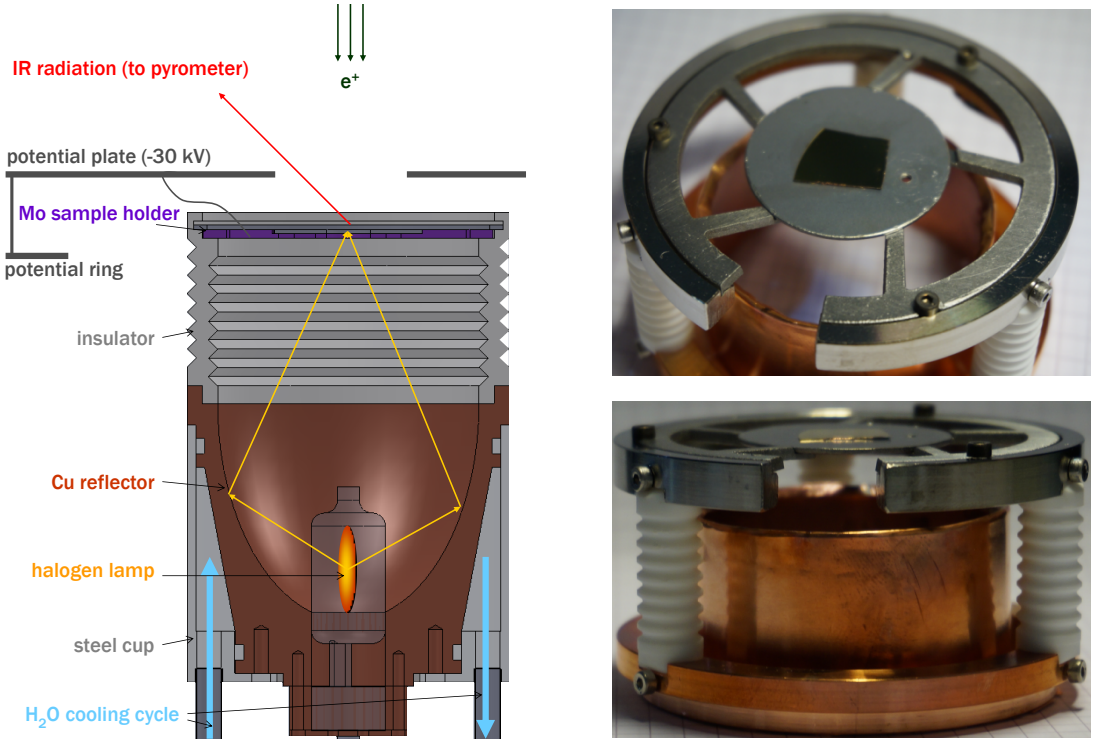

Figure 4.7: Left: Cross-sectional sketch of the new heating device for the CDB spectrometer which consists of an insulated sample holder assembly on top of a reflector (published in [14]). *Right:* Pictures of the finally used sample holder assembly with optimized insulator geometry and a Cu sheet for protecting insulators from degrading at high temperatures. Pictures were taken after several heat cycles up to 889 °C with a dummy sample on top.

spectrometer [66]. The samples are located in one of the focuses of an ellipsoidal reflector made of Cu. Thus, the light of a 250 W halogen lamp located in the opposite focus is concentrated onto the backside of the investigated samples. The samples lay on a circular Mo sheet of 3.4 cm diameter with a hole of 0.5 cm in its center, which is hold by five Mo cantilevers fixed on Macor insulators which enables biasing of the sample at high voltages. The emissivity ϵ of the Mo surface was increased by sandblasting. The reflector made of Cu is pressed in a cup made of non-magnetic steel. Water is pumped through the viton sealed space between reflector and cup for cooling this part of the assembly. Flanged at the chamber, the assembly is fixed on the positioning unit which allows to adjust the sample position within ±5 mm. The heating device is UHV compatible and pressures as low as 10^{-8} mbar are routinely reached in the chamber during operation.

During DBS measurements, the sample temperature is measured by an infrared pyrometer. It is installed outside the chamber and analyzes the thermal radiation emitted from the sample. A sapphire window at the chamber ensures a high detection efficiency for

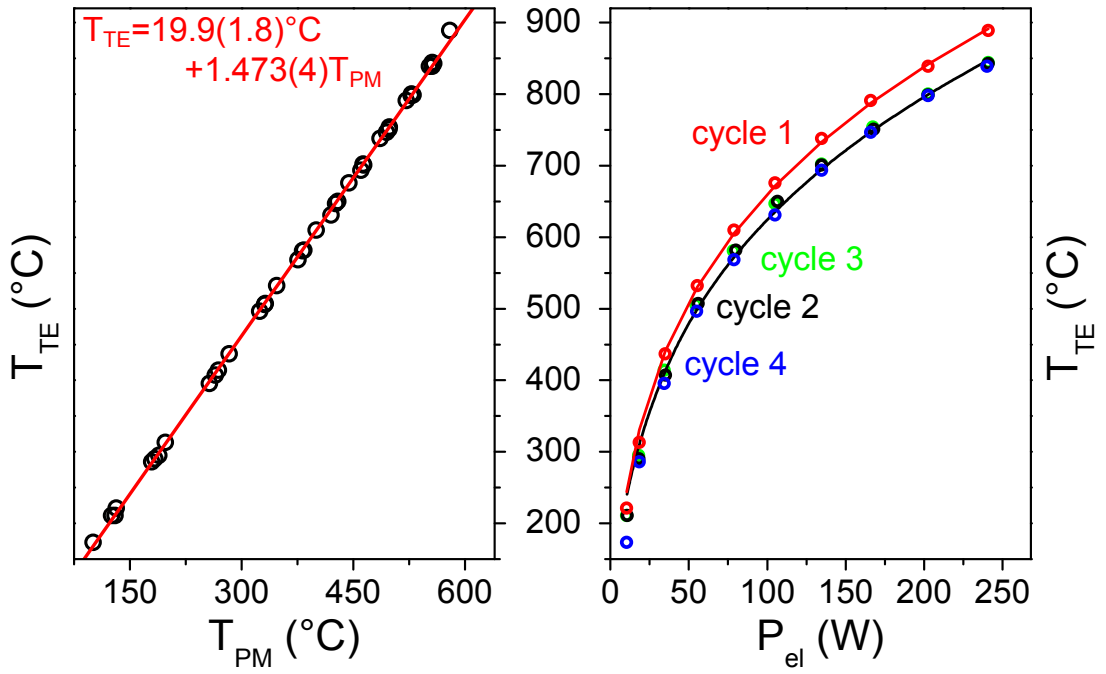

Figure 4.8: Left: Calibration curve for determining the sample temperature T_{TE} by measuring T_{PM} with a pyrometer and using the fitted equation (solid line). *Right:* The sample temperature T_{TE} as function of the electric power P_{el} consumed by the lamp (see figure 4.7). The fitted curves display a $P^{1/4}$ dependency. The drop of T_{TE} (250 W) after 'cycle 1' was caused by a sample fallen into the reflector leading to a lower reflectivity.

this infrared radiation. In order to obtain a reliable calibration, the temperature at the sample was measured by the pyrometer and by thermocouples at the same time. Two thermocouples were fixed by screws at a dummy sample and at the Mo sheet, whereas the pyrometer was focused onto a small spot next to the sample for measuring the temperature of the Mo sheet. At a constant temperature, the difference between the two values of the thermocouples was typically 5 °C, which can be considered as the measurement error. In routine calibration measurements before each beam time, the temperature T_{TE} of the thermocouple on the Mo sheet was evaluated. Calibration curves for the temperature T_{PM} as measured by the pyrometer and T_{TE} are shown in figure 4.8. T_{PM} is clearly smaller than T_{TE} due to $\epsilon < 1$ for the Mo sheet[2] and a non-ideal transmittance of the sapphire window. Various heat cycles were performed with intermediate venting of the chamber in order to simulate a typical beam time. All data points in the whole evaluated temperature range lay on a line as the linear fit shows. The fitted equation given in figure 4.8 was used for determining the sample temperature from T_{PM} during in-situ (C)DBS. Plotting T_{TE} as function of the electric power P_{el} consumed by the lamp reveals the expected $P^{1/4}$

[2] $\epsilon \approx 0.7$ can be estimated from the present results.

dependency as shown by the fitted lines plotted in figure 4.8. A maximum temperature of 889 °C was reached within these test measurements. During the other heat cycles slightly lower temperatures were achieved due to a reduced efficiency of the reflector.

Slight adjustments in the design of the sample holder assembly enabled the stable biasing of the sample at high voltages down to -25 kV or even lower above 600 °C. The cylindrical insulator as sketched in figure 4.7 was replaced by three Macor insulators with a diameter of 1 cm, which can be seen on the photos. The Macor insulators are fixed on a Cu ring laying on the reflector and carry a ring of non-magnetic steel. Between the lower ring and the reflector, a cylindrical Cu sheet is fixed which protects the surfaces of the insulators. This prevents high currents exceeding 1 mA between sample and the reflector which were observed in long-term measurements above 600 °C. With the adapted assembly, constant currents below 0.1 mA were measured at highest temperatures. Finally, for the routine use of the new heating device, the regulation of the temperature was automated within the existing spectrometer control software programmed by Pikart [66]. A PID controller was installed for reading out the temperature from the pyrometer and regulating the voltage of the power supply of the lamp. It is wired to the control computer of the CDB spectrometer via a RS 485 link. The existing control software was adapted in order to set the target temperature at the PID controller and read out the sample temperature.

4.4 CDBS with Pixelated HPGe Detectors

As previously discussed, in CDBS the longitudinal momentum component p_L of the annihilating electron-positron pair is measured. Usually, HPGe detectors are used for this purpose with a resolution of typically $1.4\,\mathrm{keV} = 5.5 \cdot 10^{-3}\,\mathrm{m_0c}$ (FWHM). The commonly used coaxial detectors do not allow the extraction of the event position in the crystal volume of the detector. Thus, no information about the transverse momentum component p_T is available. This component is measured in ACAR experiments, where both annihilation γ-quanta are detected with high angular resolution of typically $\Delta\Theta \approx 1\,\mathrm{mrad}$ $= 1 \cdot 10^{-3}\,\mathrm{m_0c}$. However, commonly used detectors in ACAR, e. g. Anger cameras or high-density avalanche chambers, do not have a high energy resolution. Thus, the Doppler shift ΔE in the energy of the annihilation quanta cannot be analyzed. Combining both approaches enables the measurement of the total momentum $\boldsymbol{p} = \boldsymbol{p}_\mathrm{L} + \boldsymbol{p}_\mathrm{T}$ for an annihilating electron-positron pair. For this purpose, in collaboration with the Universität der Bundeswehr München, two pixelated HPGe detectors were set into operation.

4.4.1 Pixelated HPGe Detectors

In the pixelated HPGe detector as shown in figure 4.9, the annihilation quanta are detected in a cuboid-shaped HPGe crystal with a size of $48 \times 48 \times 20\,\mathrm{mm}^3$. The active area of

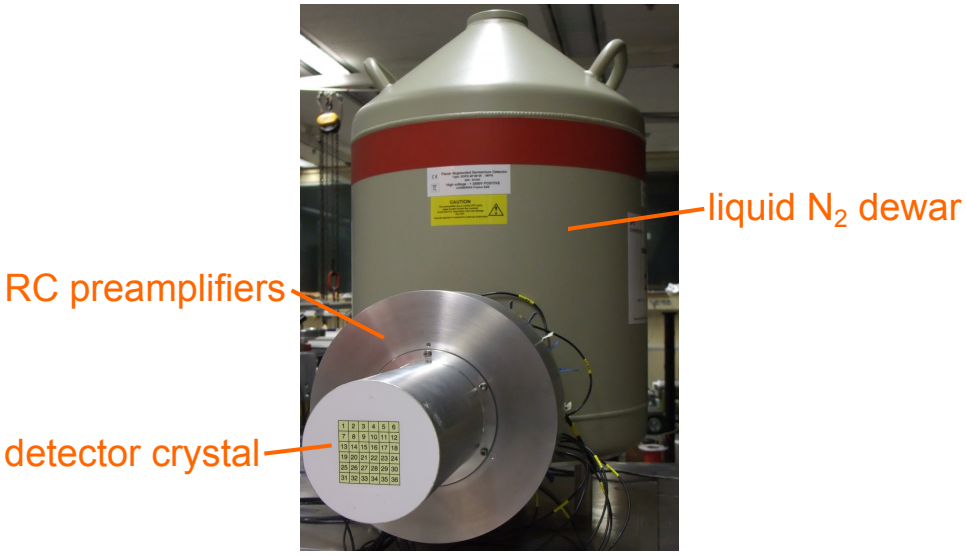

Figure 4.9: Photo of a pixelated HPGe detector (taken by Benjamin Löwe).

$48 \times 48\,\mathrm{mm}^2$ is divided into 6×6 pixels with a size of $8 \times 8\,\mathrm{mm}^2$ each. All pixels are individually contacted at their front side and wired to their own RC-preamplifiers. The specified energy resolution for these pixels is 1.3 keV (FWHM) at 662 keV for a countrate of 1000 counts per second (cps). At the back side, an electrode for the full volume of the crystal is connected to a own RC-preamplifier. Here, the energy resolution is around 2.7 keV (FWHM). In the following, it is described how the detector signals are evaluated for the energy determination and how a subpixel resolution can be achieved.

Detection of γ-Energy

For the detection of the energy of the incident γ-quanta E_γ, the detector signals from RC-preamplifiers of the pixels and the full volume contact have to be analyzed. Their output signals differ from those of the routinely used coaxial HPGe detectors with transistor reset preamplifiers. These deliver a voltage step proportional to the γ-energy as output. Their readout is comprehensively described by Pikart [66]. In the novel, pixelated detectors, the charges generated by an incident γ-quantum lead to an exponentially decaying voltage signal with a decay constant given by $RC = 50\,\mu\mathrm{s}$. This signal, as sketched in figure 4.10, is the detector output and its amplitude has to be analyzed in order to measure the energy deposited by the photon. Analog-to-Digital-Converters (ADCs), namely the SIS 3302 provided by Struck Innovative Systems, are used for digitizing the signal. These ADCs accept signals with a maximal voltage of 0.5 V.

The SIS 3302 has eight channels, which can individually sample detector signals at a rate of 100 MHz. Thus, five ADCs are required for the readout of a HPGe detector with

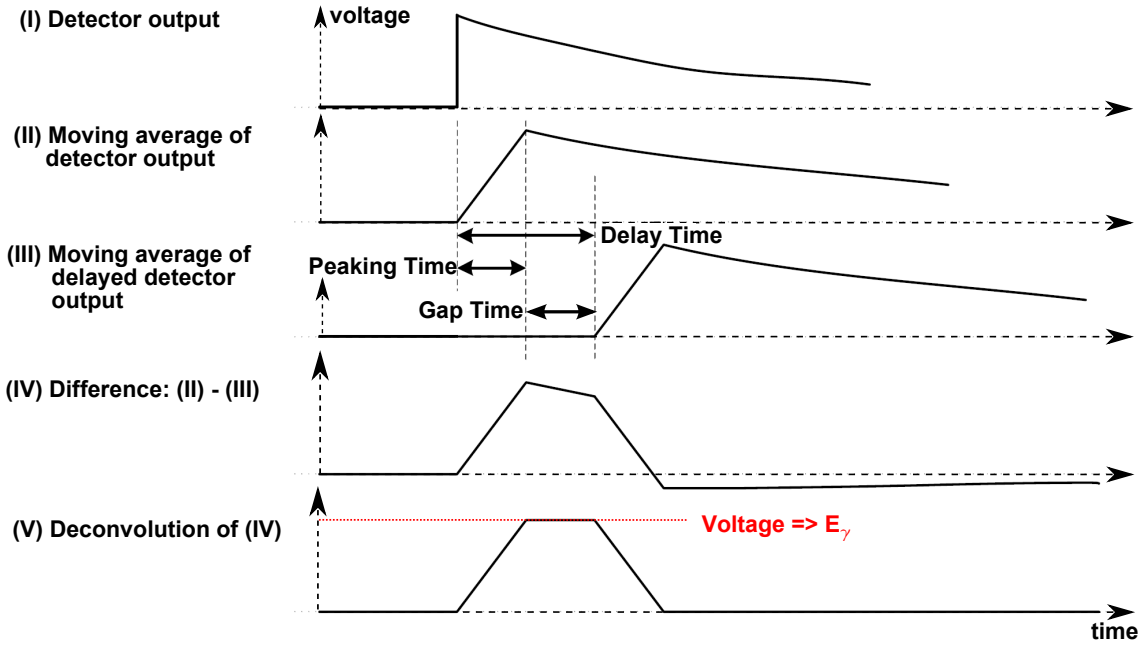

Figure 4.10: Principal steps (I) - (V) for determining energies E_γ of γ-quanta from the RC preamplifiers of the pixelated HPGE detectors with a fast 16-bit digitizer using a trapezoidal filter (sketch taken from [94] and modified).

36 pixels. The ADCs are connected via a VME bus and the data can be transmitted over a fiber link to a PC. For the data transmission, a PCIexpress to VME interface, namely the module SIS 1100e/3104, is used. In principle, the raw detector signals can be stored and analyzed at the PC which requires high memory capacity. Within the ADCs, an algorithm is implemented and thus, only a digitized value proportional to the deposited energy has to be sent to the PC. The implemented algorithm is summarized in figure 4.10. When the internal trigger of an ADC channel or an external trigger starts the acquisition, the raw data are written into a buffer and analyzed. The raw signal is denoted as signal (I) in figure 4.10. Subsequently, this signal passes the energy filter: Moving averages are evaluated for two signals, namely the original signal (II) and the delayed original signal (III) (see figure 4.10). The delay time is given as a sum of peaking and gap time, which can be set in the ADC configurations. Then, the difference of both signals, i. e. signal (IV), passes a τ-correction unit which deconvolves (IV) and hence, accounts for the decay constant. Thus, the trapezoidal signal (V) is obtained. The height of the trapeze is proportional to the deposited energy E_γ. The energy can also be measured in a conventional set-up using a spectroscopy amplifier and a Multi-Channel Analyzer (MCA). This was tested in calibration measurements with a ^{137}Cs γ-emitter (E_γ=661.7 keV [95]) where the same energy resolution was achieved as with the presented digital read-out. However, an enhanced evaluation of coincident events or signals of various pixels is not

possible using the conventional technique. The presented algorithm as implemented in the SIS 3302 allows the transmission of the event number, the raw signal, minimum, maximum, the uncalibrated 'energy' value and the timestamp of detection.

Spatially Resolved Detection

The implementation of the subpixel analysis for 2D spatially resolved detection of the incident γ-quanta was beyond the scope of this thesis and done by Benjamin Löwe. Its principles are published in [96]. Within the present work, this algorithm was successfully tested for the second pixelated HPGe detector. An exemplary measurement for demonstrating the thus reached high subpixel resolution is presented in the following.

In order to determine the precise interaction site of the incident γ-quanta in the hit

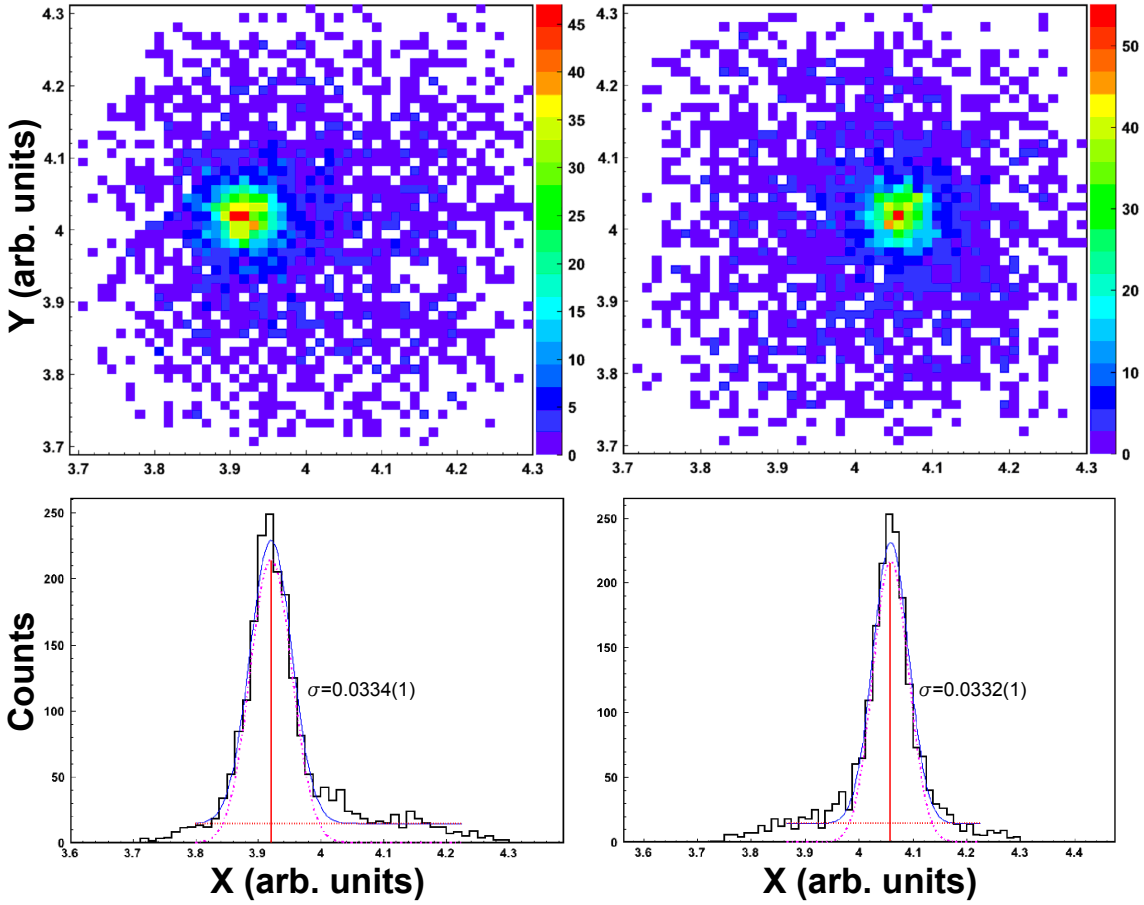

Figure 4.11: Top: 2D Spatially resolved measurement with a collimated ^{137}Cs point source at two positions on a single pixel of a pixelated HPGe detector. The color scale displays the counts. X and Y as obtained by equation 4.3 are unitless. *Bottom*: Projection along Y-direction for $3.91 \leq Y \leq 4.09$ with Gaussian fits for analyzing the subpixel resolution.

pixels, one can analyze the influenced charges in the neighboring pixels [97]. This effect was intensively investigated by B. Löwe and finally, the following algorithm was found to be optimal for the determination of the interaction position in a pixel. When a pixel is hit, the raw signals from the neighboring pixels to the left and right, i. e. in X-direction, and to the top and bottom, i. e. in Y-direction, are analyzed. The maxima I of the signals are determined after smoothing the raw signals by a moving average technique. The position (X, Y) is then given by

$$X = \log\left(\frac{I_{\text{right}}}{I_{\text{left}}}\right) \qquad \text{and} \qquad Y = \log\left(\frac{I_{\text{top}}}{I_{\text{bottom}}}\right). \tag{4.3}$$

Test measurements were made with a collimated ^{137}Cs point source. A 30 mm thick cylinder of W with a pinhole of 0.8 mm diameter along its central axis was used as collimator. The collimated source was mounted on a step motor. The source-collimator alignment was moved 2.0 mm to the right between the two measurements shown in figure 4.11. The measurements were performed on pixel (4,4). In the 2D spectra of figure 4.11, a sharp maximum is found at the position of the pinhole, where the source directly irradiates the detector. For a quantitative analysis, the projections along X and Y were evaluated. In figure 4.11, the evaluation is exemplarily performed for the projection along Y. Here, only events with $3.91 \leq Y \leq 4.09$ were considered in order to reduce the background. The projections for both measurements 1 and 2 were fitted with a Gaussian. The positions of their maxima, here given without units as obtained by equation 4.3, are $X_1 = 3.92$ and $X_2 = 4.06$. A calibration can be done easily, since $\Delta X = X_2 - X_1 = 0.14$ corresponds to a shift of 2.0 mm. It was found that a calibration over the whole area of the pixel gives the same factor for X and Y determined from equation 4.3, which is 0.070 per mm. Hence, the width of the two fitted Gaussians in figure 4.11, which amounts to 0.033 in average (σ), is 1.11 mm (FWHM). This Gaussian describes the broadening of the projection caused by both the lateral resolution of the subpixel analysis and the intrinsic width of the pinhole. Deconvolving the fitted Gaussian by the latter contribution, which is described by a root function, allows one to determine the lateral resolution to be 0.95 mm (FWHM) in X-direction. In Y-direction similar results were obtained. Hence, the interaction position can be detected with a enhanced lateral resolution of 1.35 mm (FWHM) using the described algorithm.

4.4.2 First CDBS Results at NEPOMUC

Experiment

Both pixelated HPGe detectors were installed at the NEPOMUC CDB spectrometer in a collinear alignment. The 3D electron-positron momentum distributions of Fe and Pt

were measured in well annealed, pure samples. In the following, only the respective CDB spectra obtained by analyzing the energy signal will be presented. The analysis of the 3D spectra is part of another PhD thesis.[3] The CDB spectra were compared to those measured by the conventional, coaxial HPGe detectors installed at the spectrometer.

In order to obtain a high number of events, an aperture of 5 mm diameter was used at the entrance of the CDB chamber. The pixelated HPGe detectors were positioned in a distance of 23 cm to the sample. They were run in single mode and, after the measurements, simultaneous events in both detectors were filtered by comparing the time stamp of detection. Here, events detected within a time of 5 μs were considered as valid events. For these events, the energy detected in the hit pixels was analyzed. They were only stored in the 2D-spectrum of the photopeak if in both detectors an energy of more than 400 keV was observed in a single pixel. Furthermore, a multiple interaction threshold was defined: If in an additional pixel an energy higher than 300 keV was detected, the coincident event was not considered.

The first measurements were performed on Pt. Here, the sum of peaking and gap time amounted to 11 μs. With these settings, a peak-to-background ratio of $1.0 \cdot 10^4 : 1$ was achieved. For the subsequent detection of the Fe spectrum, this time span was reduced to the half in order to suppress pile-up events. Moreover, the multiple interaction threshold was set to 50 keV. Thus, the peak-to-background ratio was increased to $1.6 \cdot 10^4 : 1$ which is a bit smaller than the $2.2 \cdot 10^4 : 1$ [4] obtained in the conventional, coaxial detectors. Possibly, the value can be further elevated by even shorter shaping times. For both applied settings, the effective energy resolution in the photopeak was 1.5 keV (FWHM). Obviously, the shorter shaping times did not deteriorate this value. In future experiments, the energy resolution will be further improved by an optimized electrostatic insulation of the pixelated detectors in order to reduce the influence of external electronic noise.

CDBS Results

The CDB ratio curves of the Fe and Pt reference samples as measured by the novel, pixelated and conventional, coaxial HPGe detectors are shown in figure 4.12. A conventionally detected Al spectrum is used as reference. In the case of Fe, both ratio curves are quasi identical. In the case of Pt, both curves show a maximum at $\Delta E = 3$ keV and an enhancement for $6 \leq \Delta E \leq 10$ keV and hence, qualitatively agree. Thus, both detector pairs principally exhibit the same elemental specific CDB signature of Pt, although this signature is less pronounced for the pixelated detectors. This difference in the intensity is attributed to long shaping times in the read-out of the pixelated detectors during the measurements on Pt. As described above, these led to a relatively high background which

[3] by Benjamin Löwe from Universität der Bundeswehr München, to be submitted within 2015
[4] This relatively low value is attributed to the high countrate during this experiment.

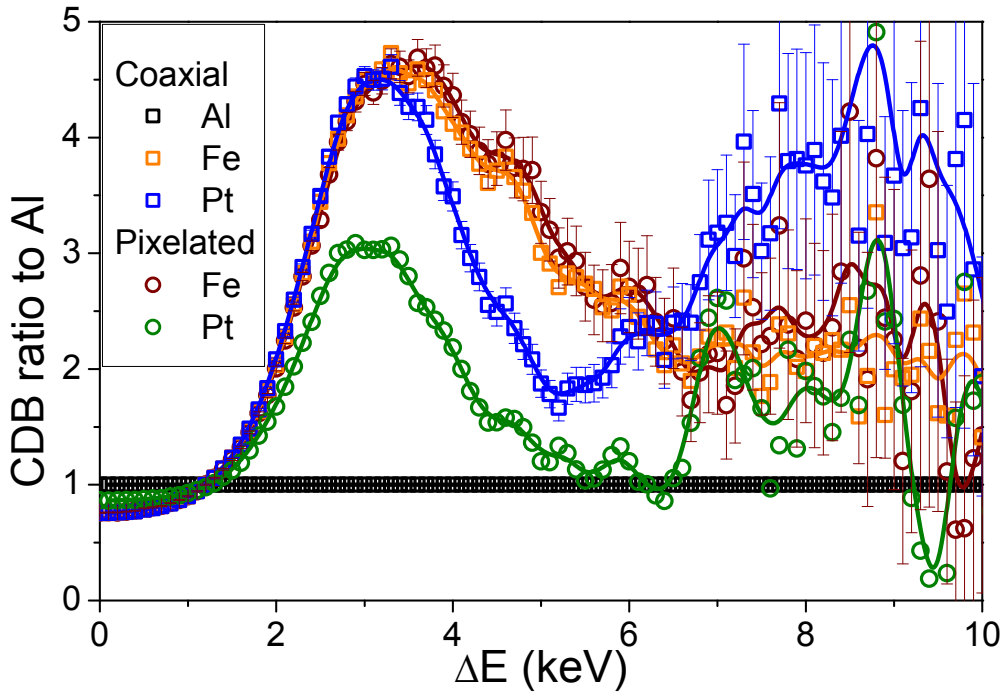

Figure 4.12: CDB ratio curves measured with pairs of conventional, coaxial HPGe detectors and novel, pixelated HPGe detectors. The CDB spectrum of Al as measured by the conventional detector pair was used as reference. The solid lines serve as guides to the eye. For a better visibility, measurement errors are only given for two measurements.

most likely causes the less pronounced CDB signature. Evidently, the described reduction of the shaping time and more rigorous suppression of the multiple interaction events for the Fe measurement was sufficient in order to detect CDB spectra with the same quality as in the conventional set-up.

Detection Efficiency

In both measurements with the pair of pixelated HPGe detectors, the countrate in the coincident photo peak was only around 1.7 % of that in a single pair of the conventional detectors. In order to understand this difference, one has to consider geometric aspects and the detection of γ-quanta in detail. The characteristic values describing the differences between both detector types are given in table 4.1.

The cuboid-shaped crystals of the pixelated detectors are clearly thinner and have a smaller effective active area than the cylinder-shaped crystals of the coaxial detectors. In table 4.1, it is already accounted for the fact that only the inner 4×4 pixels were evaluated in order to obtain valid signals from neighboring pixels for all events. Active area, thickness and total volume of the Ge crystals play an important role for the microscopic processes

	Pixelated	Conventional	Ratio
Geometry			
Active area	$32 \times 32\,\mathrm{mm}^2$	$30^2\,\pi\,\mathrm{mm}^2$	0.36
Thickness	2 cm	5.1 cm	0.39
Detection probabilities	in a single pixel	complete volume	
Interaction	0.56	0.87	0.64
Single photoelectric event	0.024	0.037	0.65
Compton scattering & photoelectric event	0.048	0.430	0.11
Total γ-energy	0.072	0.467	0.15

Table 4.1: Comparison between the conventional, coaxial and the novel, pixelated HPGe detectors; the ratios given in the last column were obtained by dividing the values for the pixelated detector by those of the coaxial one. The detection probabilities apply to γ-quanta with an energy of 511 keV and were determined in Geant4 simulations by B. Löwe.

leading to the detection of the energy of γ-quanta. The following phenomena can occur if a passing γ-quantum interacts in the crystal of a detector:

1. Deposition of the total energy in a single, photoelectric event.
2. Deposition of the total energy by a single or several Compton scattering events and a subsequent photoelectric event.
3. Deposition of a part of the energy by a single or several Compton scattering events.

The probabilities for the occurrence of these events are different for both crystals.

Geant4 [98] simulations considering the detection of γ-quanta in both detector types were conducted by B. Löwe.[5] The results of these simulations, described by the detection probabilities given in table 4.1, are shortly discussed here in order to explain the observed differences in the countrates. The probabilities were obtained by simulating γ-quanta which either hit the center of the front side of a pixel of the pixelated detector or the center of the front side of the crystal of a coaxial detector. The probability for at least one interaction with the crystal is 56 % in the first and nearly 87 % in the second case. For the coaxial detectors, 46.7 % of all incident photons deposit all their energy in the detector and thus, lead to valid event in the photopeak which can be used for (C)DBS. In the case of the pixelated detectors, this probability only amounts to 7.2 % and hence, is strongly suppressed. The reason for this is that γ-quanta with $E_\gamma = 511\,\mathrm{keV}$ are most probably

[5] See PhD thesis of B. Löwe (to be submitted within 2015).

detected by multiple Compton scattering and subsequent absorption in a photoelectric event in Ge [99]. In the pixelated detectors, such events only can be used when all processes of interaction take place in a single, relatively small pixel. Due to the small pixel volume, the probability for these events is reduced by a factor of 0.11 compared to the coaxial detectors. In contrast to this, the probability for the occurrence of any interaction or even a single, photoelectric event is only reduced by a factor of around 0.65, which is mainly caused by the smaller thickness of the crystals. Apparently, the relatively improbable detection by a single photoelectric event is favored in the pixelated detectors due to the small pixel volume: Whereas in the coaxial detectors only around 10 % of the photons, which deposit all their energy of 511 keV, are absorbed in a single photoelectric event [99], in a pixel of the novel detectors this fraction amounts to 41 %.[6]

Now it is possible to compare values for the detection efficiency of the conventional and novel detectors. For CDBS measurements, the total energy of both annihilation γ-quanta must be detected. In a pixel, the chance for this process is reduced by a factor of 0.15 compared to the conventional detector as seen in table 4.1. Moreover, the active area is smaller by a factor of 0.36 in case of the novel, pixelated detectors. Thus, their detection efficiency in coincident measurements is only $0.36 \cdot 0.15^2 = 0.008$ of that of the coaxial detectors at the same distance to the sample. Here, an absolute collinear emission of the annihilation γ-quanta is assumed. In the present CDBS measurements, this factor was around 0.017 and well compares with the theoretical value of 0.008. The discrepancy between both values is explained by different distances for the detector pairs to the sample during the measurements. Moreover, the dead time behavior of both acquisition systems is expected to be different and has to be analyzed in detail in order to determine the theoretical detection efficiency more precisely.

Conclusion

It was clearly shown that conventional (C)DBS by use of the novel, pixelated detectors works well and gives reliable results. The agreement for Fe demonstrates the high reliability in the detection of CDB spectra even at the maximal countrate available at the NEPOMUC CDB spectrometer. Compared to the conventional, coaxial HPGe detectors, the novel detectors are less efficient technique due to the low probability for the detection of photopeak events. Most importantly, detected 3D spectra of the electron-positron momentum distribution now can be safely interpreted since the working of the novel detection by the pixelated detectors and the optimized read-out algorithm for the γ-quantum energy was clearly proven by the agreement with independent measurements using conventional detectors. Thus, a new and unique technique for PAS is now available at the NEPOMUC CDB spectrometer.

[6] These values stem from Geant4 simulations of Matthias Hackenberg (Technische Universität München).

Chapter 5
5 Defect Study on MnSi Single Crystals

MnSi has been in the focus of research in solid state physics for a long time due to its exceptional magnetic properties. A set of MnSi single crystals, grown by optical float zoning, was investigated by means of PAS in order to study lattice defects. Important goals of this study were to probe the spatial homogeneity and to identify effects due to changes in the stoichiometry. Complementary CDBS and PALS were applied on a set of single crystals with a varying excess of Mn. Accompanying experimental studies involved Prompt-Gamma Neutron Activation Analysis (PGAA), which was performed at a neutron beam line of the FRM II. This study was part of a collaboration involving single crystal growth and characterization, analysis of the crystals' magnetic properties and theoretical calculations for the formation of point defects in MnSi.

5.1 The Compound MnSi

MnSi is a B20 compound with a lattice constant of 0.458 nm and crystallizes in the cubic space group $P2_13$ lacking inversion symmetry. In the 1970's and 1980's, MnSi was found to be an ideal example for a weak itinerant-electron ferromagnet [23–26]. Nuclear Magnetic Resonance (NMR) [27] and neutron scattering experiments [28] showed that electron spins in MnSi order in a helical structure along the $\langle 111 \rangle$ direction below a critical temperature of $T_c = 29.5\,\mathrm{K}$ in zero magnetic field. The first-order phase transition from the paramagnetic regime to the helimagnetic regime at T_c emerges from ferromagnetic fluctuations, which gain chiral character with decreasing temperature in a so-called Braszovski scenario [29–31]. Applying hydrostatic pressure reduces T_c and, at a critical pressure of $p_c = 14.6\,\mathrm{kbar}$ [32], the helimagnetic phase vanishes. Recently, for higher pressures a non-Fermi liquid behavior with a topological Hall effect has been observed [33]. Moreover, Small Angle Neutron Scattering (SANS) and Hall effect measurements revealed the A-phase of MnSi as a topologically stable skyrmion lattice [34, 35]. A rotation of this lattice was observed

as response to currents, which are more than five orders of magnitude smaller than those typically applied in studies on current-driven magnetization dynamics in ferromagnetic materials and semiconductors [36].

Despite these exciting magnetic properties which occur due to strong electronic correlations, the role of lattice defects in the present system has not been in the focus of attention so far. Commonly, the Residual Resistivity Ratio $RRR = \rho\,(293\,\mathrm{K})\,/\rho\,(T \to 0\,\mathrm{K})$ is used for characterizing the crystal quality [100, 101]. Here, the electrical resistivity ρ at room temperature and very low temperatures is evaluated. Interestingly, deviations in the magnetic transition temperatures determined in various MnSi crystals with different RRR were found [102]. This strongly indicates that lattice defects have an important influence on the magnetic properties. An identification of these defects is non-trivial, since – even when only accounting for point defects – four different defect types have to be considered, which are vacancies and antisite atoms on both the Mn and Si sublattice. Theoretically, the presence of these defects can be investigated by calculating their effective formation energies [103, 104]. Experimentally, their presence was studied in the present work for the first time by combining various experimental techniques for the investigation of MnSi single crystals with different chemical composition.

5.2 Investigated MnSi Single Crystals

Preparation Method

The variety of extraordinary physical phenomena highlights the importance of monocrystalline MnSi for fundamental research and possible applications. For the preparation of such high-quality samples, a procedure has been developed in the group of Christian Pfleiderer at Technische Universität München which is based on the optical float zone technique [102, 105]. This procedure involves two main steps, namely (i) the fusing of initial rods from high-purity elements (precast 4N Mn and 6N Si) in an inductively heated rod casting furnace, which are then, after remelting for several times, (ii) float zoned in a UHV compatible image furnace with counter rotating seed and feed rods [106]. All these steps are performed in a highly pure Ar atmosphere of 1.5 bar. However, out gassing of Mn can still be observed during the preparation due to its higher vapor pressure compared to Si. This suggests that stoichiometric single crystals are only obtained with a Mn excess present in the initial rods used for crystal growth. As known from to the metallurgical phase diagram of this binary alloy plotted in the appendix, MnSi is congruently melting at 1270 °C [107], which makes it well suited for the applied float zoning technique. It shows a very narrow homogeneity range. Practically, the Mn excess in MnSi single crystals is expected to lie in a range between -0.8 % and 2 % (at.).

Overview of Investigated Specimens and Applied Techniques

The investigated MnSi single crystals were prepared by Andreas Bauer (Technische Universität München) and coworkers. A photo of a typical crystal is shown in figure 5.2. The grown crystals are cylinders with a typical length of 20 mm and a diameter of around 4 mm. Their single-crystallinity is checked by X-ray Laue diffraction after preparation. The investigated specimens stem from a series of crystals, which were grown in order to investigate the influence of a crucial growth parameter on the crystal quality, namely the initial Mn excess x used for fusing the initial rod. All MnSi crystals studied by PAS as listed in table 5.1 were grown with a rate of 5 mm/h and x varying between -0.01 and 0.04 in steps of 0.01. For all crystals, discs from the begin and end of the cylinders were cut for probing the quality by measurements of the RRR as shown in section 5.3 and for characterizing the magnetic properties.

Within the present work, PGAA was used for analyzing the chemical composition of the crystals and PAS was applied for the examination of lattice defects. As substantial part of the PAS experiments, discs from the end of the crystals were probed by depth dependent (C)DBS at the NEPOMUC positron beam; the results are presented in sections 5.4 and 5.5. The same discs were used for the PGAA measurements, which are discussed in section 5.3. In a complementary study, the crystalline cylinders were investigated by PALS at the Gamma Induced Positron Source (GIPS) of the Helmholtz-Zentrum Dresden-Rossendorf as described in section 5.6. The obtained information on lattice defects are summarized and linked with the experimental and theoretical work of collaborators in section 5.7. Laterally resolved DBS for studying the homogeneity of crystal OFZ 71 is presented in section 5.8 before this chapter is concluded.

Sample	**Disc**	**Initial Mn excess x**
OFZ 65	3-3	-0.01
OFZ 66	3-3	0.00
OFZ 67	3-3	0.01
OFZ 68	3-3	0.02
OFZ 81	3-3	0.03
OFZ 83	3-2-1	0.04
OFZ 71	severals	-0.01 — 0.02

Table 5.1: Investigated MnSi single crystals. The initial Mn excess x is defined by the net weight of the two components in the initial stage of crystal growth. The discs cut from the end of crystalline cylinders were studied by CDBS at the NEPOMUC beam, the respective cylinders were probed by PALS at the GIPS facility (see figure 5.2 for a photo of a typical crystal).

5.3 Characterization by Complementary Techniques

Chemical Composition as Studied by PGAA

Prompt-Gamma Neutron Activation Analysis (PGAA) was performed at the FRM II [108] in cooperation with Petra Kudejova. The discs from the crystals' end were probed by irradiation with cold neutrons. Neutron capture in the nuclei leads to emission of characteristic γ-quanta with energies specific for the respective nuclide. Therefore, the detection of their energy spectrum by HPGe detectors allows to analyze the chemical composition of samples. Thus, concentrations for all present elements can be determined. For the MnSi crystals, the relative atomic concentration of Mn to Si was evaluated. The relative Mn excess is plotted in figure 5.1. Within the high statistical error of the data points, very similar values were found for all crystals as expected due to the narrow homogeneity range of the MnSi phase. The lowest Mn excesses was detected for $x = -0.01$ indicating Mn deficiency here. Moreover, as seen in figure 5.1, H was detected in all samples with a concentration of around 2.3 % (at.). This result is surprising, since the crystals were prepared in a high-purity Ar atmosphere as described above. Possibly, the detected H atoms have diffused into the specimens at room temperature after preparation.

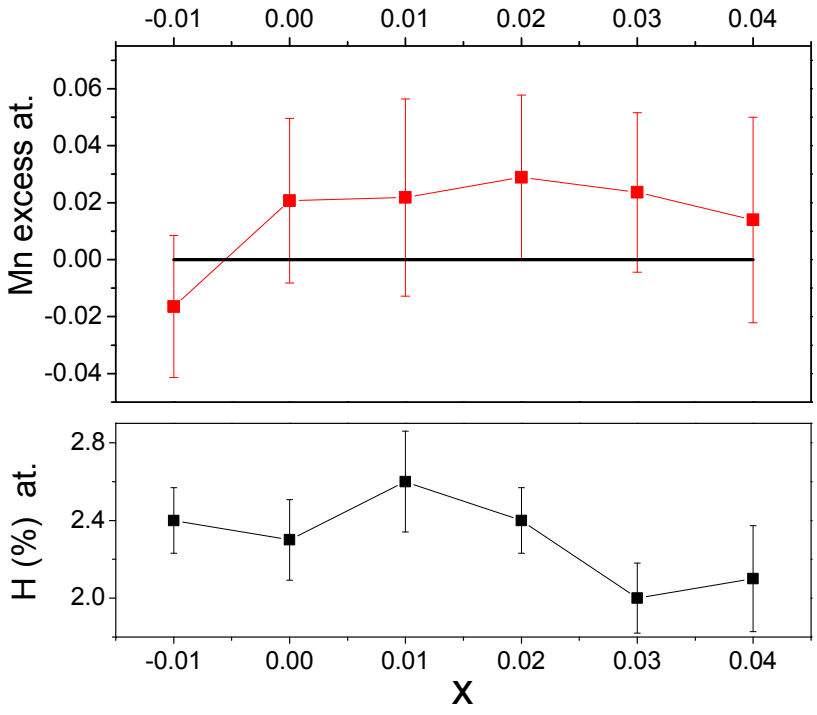

Figure 5.1: PGAA results for MnSi discs with varying initial Mn content x. *Top:* Mn excess as obtained from the relative intensities of the Mn and Si peaks. *Bottom:* Concentration of detected H atoms.

Crystal Quality as Studied by the Residual Resistivity

The RRR as function of the initial Mn excess x was obtained by measurements of the electric resistivity ρ as shown in figure 5.2. The data were obtained by the collaborators who have grown the crystals as described in [102]. $RRR\,(x)$ was measured in discs from the begin (blue data points) and end (red data points) of the crystals. As marked in the photo of a typical investigated MnSi crystal in figure 5.2, the end discs were probed by (C)DBS. For them, a maximal RRR, which indicates the highest sample quality, is found at $x = 0.01$. For $x \leq 0.00$ and $x \geq 0.03$, relatively low values of the RRR reveal a high concentration of lattice defects. For the wafers from the begin, the maximum is detected at $x = 0.02$. For $x = 0.02$ and 0.03, the RRR values at the begin of the crystals are higher than at the end. This could be caused by additional annealing since this region is at elevated temperatures for a longer time during the float zoning. A main goal of the present work was the identification of lattice defects, which lead to the observed dependency of RRR on x. Whereas in this work only crystals grown with 5 mm/h were analyzed, in figure 5.2 also the results from crystals grown with 2 mm/h are shown. Apparently, the different growth rates did not lead to significant differences.

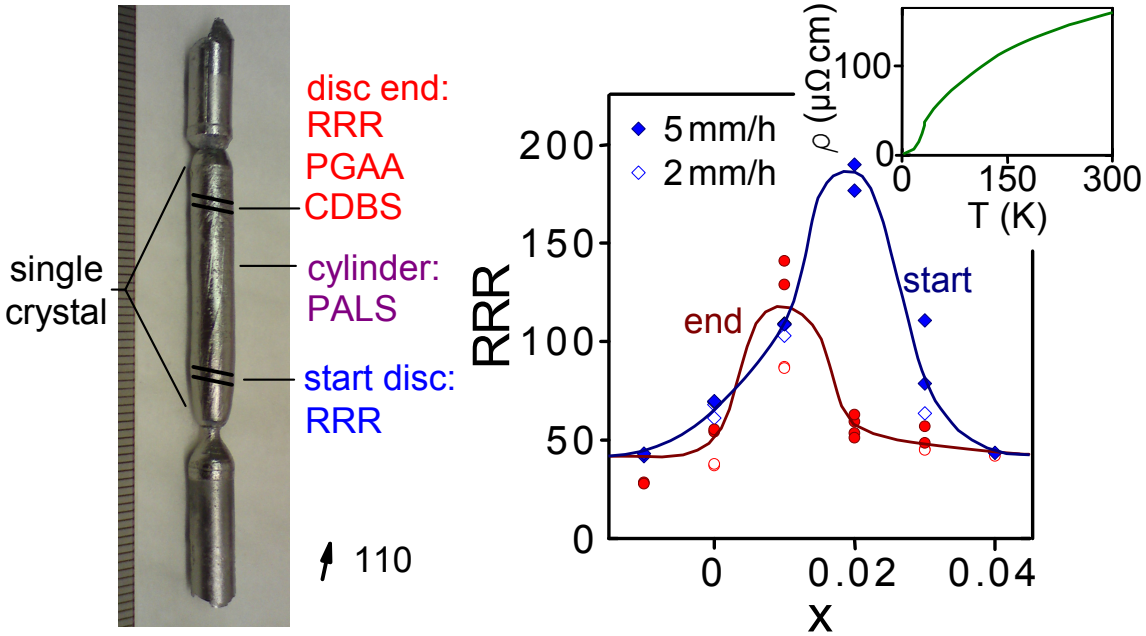

Figure 5.2: Left: Photo of a probed MnSi single crystal. Different specimens from the crystals were studied by various techniques. *Right:* Residual Resistivity Ratio $RRR = \rho\,(293\,\mathrm{K})\,/\rho\,(0\,\mathrm{K})$ as function of the initial Mn excess x for discs from the start end of MnSi crystals grown with rates of 2 and 5 mm/h. The RRR was obtained from the temperature dependency of the electrical resistivity ρ as exemplarily shown in the small inset (figure taken from Andreas Bauer [102] and modified).

5.4 (C)DBS at NEPOMUC

5.4.1 Depth Dependent DBS in MnSi Discs

The MnSi discs listed in table 5.1 were investigated in the CDB spectrometer at the NEPOMUC positron beam line. Firstly, depth dependent DBS was conducted and the $S(E_+)$ profiles shown in figure 5.3 were obtained. By use of equation 2.17 and estimating the material dependent parameters to $A = 3.67 \frac{\mu g}{cm^2} keV^{-n}$ and $n = 1.65$, the mean implantation depth $\bar{z}$ can be calculated from the incident positron energy E_+. As described in section 2.4, the material dependent Makhovian parameters were determined from the mass density by a linear interpolation. For all discs, the S-parameter is nearly constant above an incident positron energy of $E_+ \approx 22\,\mathrm{keV}$, i. e. $\bar{z} = 1.0\,\mu\mathrm{m}$. Thus, for higher E_+ all positrons probe the bulk where they annihilate with a characteristic bulk S-parameter. This bulk value is different for most of the wafers and clearly decreases with an increasing Mn excess in the initial rod before single crystal growth. This clear and strong effect will be investigated in detail in the following.

Furthermore, it was tried to estimate the positron diffusion length L_+ by fitting the

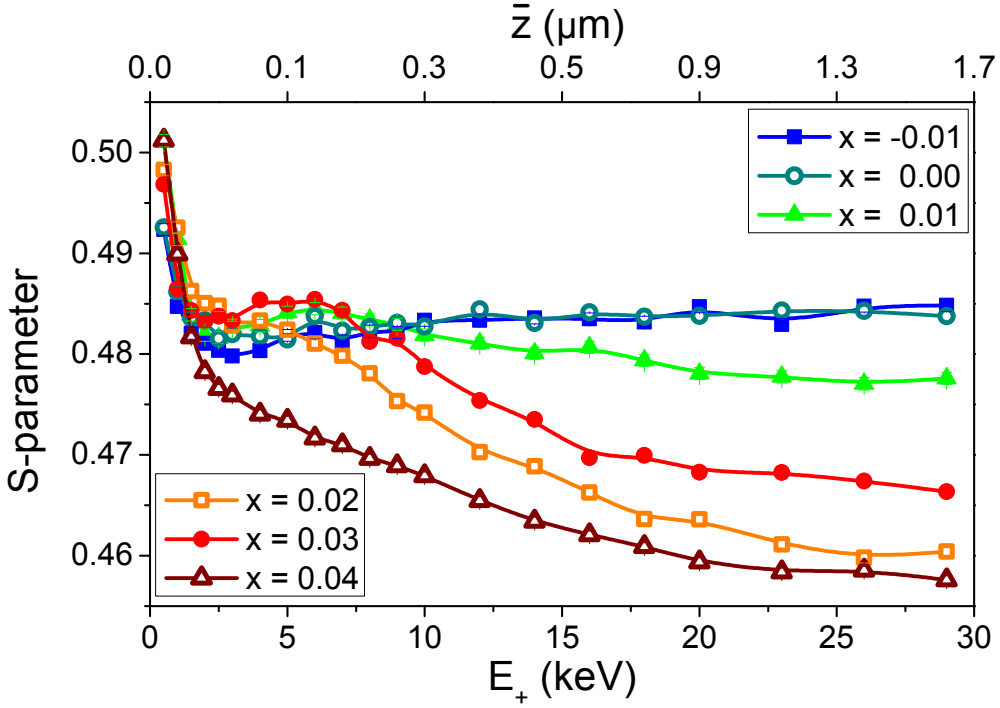

Figure 5.3: S-parameter as function of the incident positron energy E_+ and mean implantation depth $\bar{z}$ in MnSi discs with varying initial Mn excess x; solid lines are guides to the eye. The statistical error of the data points is smaller than the symbols.

$S(E_+)$ curves with the VEPFIT software [73] from the present data. L_+ can be determined by a quantitative evaluation of the positron back diffusion to the surface [7,8] by analyzing the transition from the S-parameter detected at the surface to the bulk S-parameter S_{MnSi} as described in more detail in section 2.4 or [58, 70]. In the investigated set of samples, the fitting procedure revealed that this transition is determined by two effects: Firstly, for $E_+ < 3\,\mathrm{keV}$ a steep decrease is seen, which is mainly attributed to the annihilation of non-thermalized, so-called epithermal positrons [8, 49–51, 109] and other surface effects. Secondly, close to energies of $E_+ \approx 5\,\mathrm{keV}$, for $0.01 \leq x \leq 0.03$ a clear plateau is seen. Also the other samples exhibit more or less such a plateau, but less distinct: For $x \leq 0.00$, a slightly lower S-parameter than in the bulk is detected at these energies. In the case of $x = 0.04$, a monotone decrease is exhibited by the $S(E_+)$ curve and quite linear between 3 and 15 keV. This linear behavior clearly shows that the specimen is not homogeneous in depth, because a transition from surface to bulk in homogeneous samples leads to a bent $S(E_+)$ curve, as found, e. g., for single-crystalline Si or well annealed Cu [58, 70]. The plateau-like behavior, observed in all samples, must be caused by a sub-surface layer in a depth of 100 nm, where positrons annihilate with a different S-parameter than in the bulk. Within the preparation process of these discs, the samples were mechanically polished. It is concluded that this polishing led to a damaged sub-surface layer as indicated by the plateau visible at around 5 keV in the $S(E_+)$ depth profiles. The damaged sub-surface region cannot be accounted for properly in fitting models and thus, L_+ could not be determined. Despite the lack of this information, a comprehensive investigation of vacancies was performed as shown in the following.

Characteristic DBS Lineshape Parameters

In order to further investigate the effect of the initial Mn excess x in the bulk as observed in depth dependent DBS, the characteristic lineshape parameters S_{MnSi}, as usual determined from events with $\Delta E \leq 0.84\,\mathrm{keV}$, and W_{MnSi}, which were obtained by evaluating events with $2.5 \leq \Delta E \leq 3.5\,\mathrm{keV}$, are discussed. These parameters from single spectra, recorded in coincidence with the opposite detector, were measured in the bulk of the discs with an incident positron energy of $E_+ = 25\,\mathrm{keV}$. The thus obtained S-W-plot is shown in figure 5.4 and can be interpreted as follows. Without Mn excess, i. e. $x = -0.01$ and $x = 0.00$, the obtained data points lay together and here the maximum S_{MnSi} and the minimum W_{MnSi} are detected. Hence, it is concluded that these two samples show a similar structure and have the highest concentration of open volume defects. This concentration is reduced with an initial Mn excess, since the S-parameters decrease and the W-parameters increase for $x \geq 0.01$. Moreover, the data points lie on a line, as the linear fit illustrates. This behavior is interpreted as a clear transition between only two positron states leading to correlated changes of S_{MnSi} and W_{MnSi} in dependence on x.

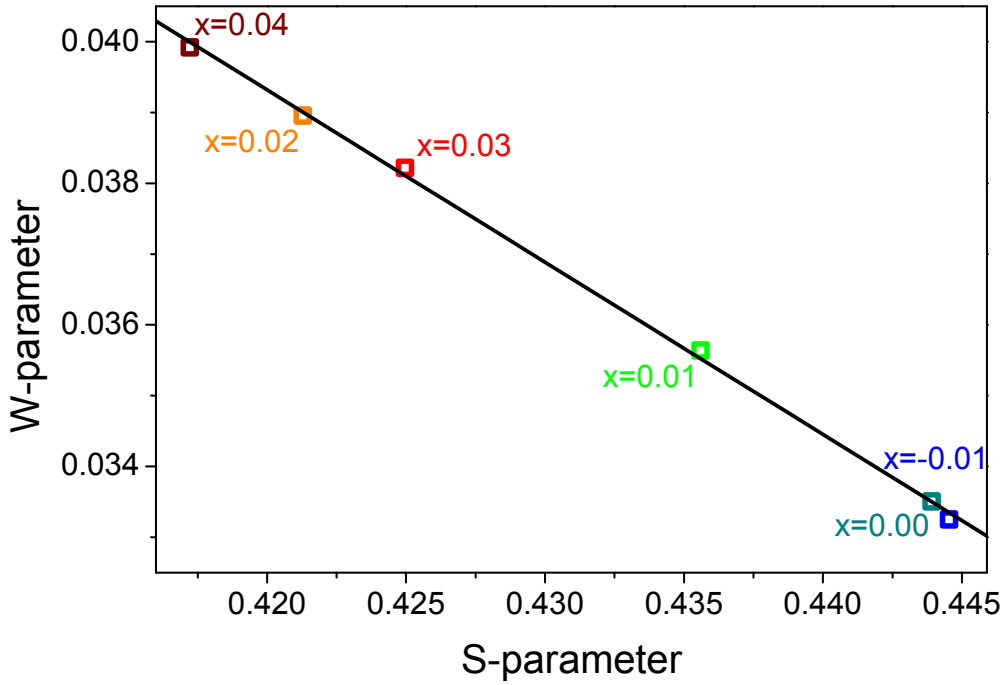

Figure 5.4: S-W-plot for MnSi discs with varying x at $E_+ = 25\,\mathrm{keV}$. The solid line is a linear fit. Statistical errors of the data points are $\Delta S = 4.7 \cdot 10^{-5}$ and $\Delta W = 1.8 \cdot 10^{-5}$.

5.4.2 CDBS in the Bulk of Discs

In order to confirm these findings and to further characterize the involved positron states, the CDB spectra denoted by $J(\Delta E, x)$ were measured at $E_+ = 25\,\mathrm{keV}$. For their interpretation, the respective CDB ratio curves $R(\Delta E, x) = J(\Delta E, x)/J(\Delta E, -0.01)$ to OFZ 65-3-3 with $x = -0.01$ were analyzed as shown in figure 5.5. The changes for low Doppler shifts $\Delta E \leq 4\,\mathrm{keV}$ reflect the behavior of S_{MnSi} and W_{MnSi} as described above. For higher Doppler shifts, which are caused by the annihilation with high momentum core electrons, the following effects can be observed: For $x = -0.01$ and $x = 0.00$, nearly the same CDB signatures were detected. With a Mn excess $x \geq 0.01$, the ratio curves show a clear and systematic enhancement, which is caused by a higher probability for the annihilation with core electrons.

Assuming a transition between exactly two positron states explains the found systematic changes in the CDB spectra: All spectra $J(\Delta E, x)$ and hence, all ratio curves $R(\Delta E, x)$ can be described by the linear superposition

$$R(\Delta E, x) = (1 - a_{\mathrm{CDB}}(x)) \cdot R(\Delta E, -0.01) + a_{\mathrm{CDB}}(x) \cdot R(\Delta E, 0.04) \tag{5.1}$$

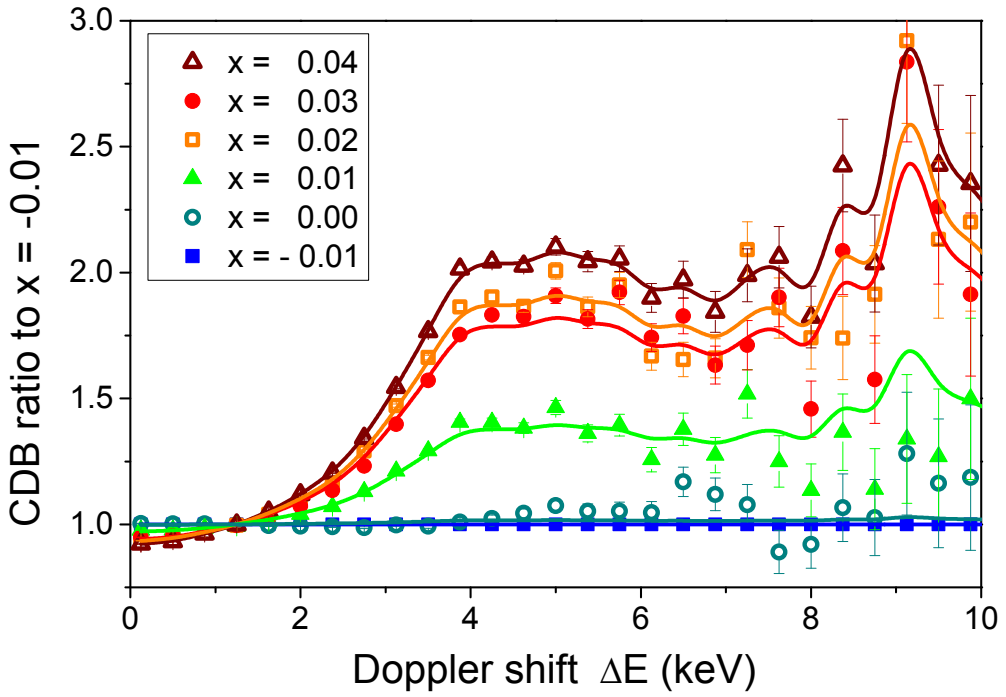

Figure 5.5: CDB ratio curves $R(\Delta E, x)$ of MnSi discs with OFZ 65-3-3 ($x = -0.01$) as reference. The solid lines are a linear superposition of the ratio curves $R(\Delta E, -0.01)$ and $R(\Delta E, 0.04)$ with the fitted weighting factor $a_{\mathrm{CDB}}(x)$ (see figure 5.6).

of the two references $R(\Delta E, -0.01)$ of OFZ 65-3-3 and $R(\Delta E, 0.04)$ of OFZ 83-3-2-1. Fitting the weighting factor $a_{\mathrm{CDB}}(x)$ to the measured curves and superposing the ratio curves of the references accordingly yielded in the solid lines in figure 5.5. Their good agreement with the measured ratio curves and the observed increase of the probability for annihilation with core electrons confirms the conclusions drawn from the conventional DBS measurements: An initial Mn excess x reduces the open volume in the samples, which leads to a transition between two dominant positron states.

5.4.3 Dependency of (C)DBS Results on Initial Mn Excess x

The detected transition, observed in all applied (C)DBS techniques, is the main result of the measurements presented in this section. For its detailed characterization, which means the identification of involved vacancy types and their respective concentrations in particular, the fitted weighting factor $a_{\mathrm{CDB}}(x)$ will be used in the following. It is plotted together with the calculated weighting factors $a_{\mathrm{S}}(x)$, $a_{\mathrm{W}}(x)$ and $a_{\mathrm{S(E)}}(x)$ in figure 5.6. The weighting factor $a_{\mathrm{S}}(x)$ was obtained from the S-parameters $S_{\mathrm{MnSi}}(x)$ as shown in

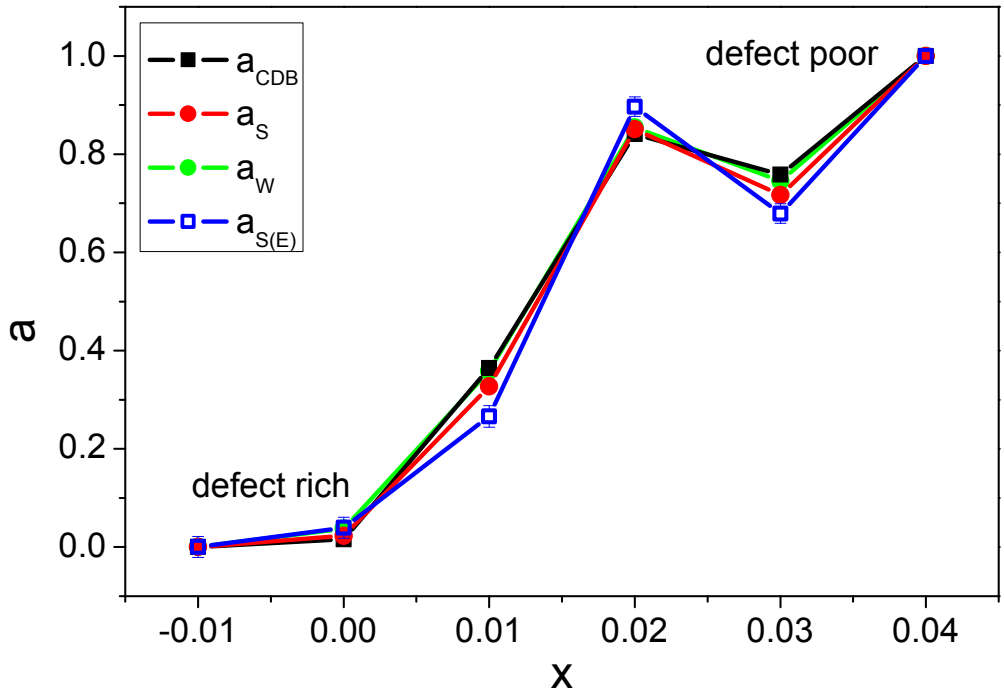

Figure 5.6: The weighting factors a_{CDB}, a_{S}, a_{W} and $a_{\mathrm{S(E)}}$ determined from the measurements shown in figures 5.3, 5.4 and 5.5 as function of the initial Mn excess x. Only for $a_{\mathrm{S(E)}}(x)$, the statistical errors of the data points are slightly larger than the symbols.

figure 5.4 by use of the following equation:

$$S_{\mathrm{MnSi}}(x) = (1 - a_{\mathrm{S}}(x)) \cdot S_{\mathrm{MnSi}}(-0.01) + a_{\mathrm{S}}(x) \cdot S_{\mathrm{MnSi}}(0.04) \tag{5.2}$$

In the same way, by analyzing $W_{\mathrm{MnSi}}(x)$ instead of $S_{\mathrm{MnSi}}(x)$, the weighting factor $a_{\mathrm{W}}(x)$ for the W-parameters was determined. Additionally, the same analysis was conducted for $S(E_+ = 29\,\mathrm{keV}, x)$ measured in the specimens within the initial depth dependent DBS profiles. All these weighting factors agree in their dependency on x. Their behavior reflects the transition from defect rich samples for $x \leq 0.00$ to defect poor samples with the lowest concentration of open volume defects at $x = 0.04$. In the defect rich samples with $x = 0.00$ and -0.01, it is assumed that all positrons annihilate in the same microscopic state, since all (C)DBS observables were identical for both samples. As shown in the following section, this microscopic state is identified as a Mn monovacancy. The agreement of the various weighting factors demonstrates that (C)DBS is an excellently suited technique for the present system in order to extract qualitative and quantitative information about the presence of open volume defects.

5.5 Enhanced Evaluation of CDBS Results

5.5.1 Identification of Vacancy Types

The most probable reason for the changes of the CDBS results in dependence of the initial Mn excess x is the reduction of the concentration of Mn vacancies V_{Mn} with increasing x. In order to confirm this explanation, CDB spectra and positron lifetimes were calculated by use of the MIKA Doppler package described in chapter 3. For this purpose, a supercell of $4 \times 4 \times 4$ unit cells was constructed and used as input for the calculations on a mesh of $128 \times 128 \times 128$ grid points. Thus, the annihilation characteristics of defect free MnSi were determined. In dependence of the applied method for modeling the electron-positron enhancement, positron lifetimes $\tau_b = 1/\lambda_b$ between 105 and 111 ps were obtained in the defect free bulk. Moreover, the two species of potential monovacancies in this system, V_{Mn} on the Mn and V_{Si} on the Si sublattice, were investigated by removing a single atom from the central part of the unit cell. This corresponds to a concentration of $c_{VMn} = c_{VSi} = 0.004$ per atom on the respective sublattice. It was checked that at these concentrations the positron is trapped in the respective vacancies by evaluating the positron probability density $|\Psi_+(\mathbf{r})|^2$. In the presented approach, a lattice relaxation around the vacancies was not accounted for. For both vacancy types the obtained theoretical lifetimes hardly differed: Typically, the positron lifetime in V_{Mn} is only 3 ps longer than in V_{Si}. Hence, V_{Mn} and V_{Si} cannot be distinguished unambiguously by PALS. The precise values for the lifetimes of positrons trapped in monovacancies were found to vary in a range between 160 and 181 ps, since the absolute value depends on the applied model for the electron-positron enhancement. Due to the best agreement with the PALS results presented in section 5.6, the enhancement was treated with a LDA approach by a parametrization proposed by Boronski and Nieminen, which is given in the appendix. The thus obtained characteristic lifetimes are $\tau_b^{th} = 111$ ps, $\tau_{VSi}^{th} = 178$ ps and $\tau_{VMn}^{th} = 181$ ps. Moreover, a Mn vacancy occupied by a H atom was considered resulting in a positron lifetime of $\tau_{VMn-H}^{th} = 144$ ps.

The theoretical CDB ratio curves $R_{b/VMn}^{th}(\Delta E)$ and $R_{b/VSi}^{th}(\Delta E)$ were obtained by dividing the calculated CDB spectrum of defect free bulk $J_b^{th}(\Delta E)$ by those characteristic for V_{Mn}, i. e. $J_{VMn}^{th}(\Delta E)$, and V_{Si}, i. e. $J_{VSi}^{th}(\Delta E)$, respectively. These theoretical CDB ratio curves are presented in figure 5.7 together with the experimental ratio curve $R(\Delta E, -0.01)$. The comparison between calculated and experimental ratio curves enables to identify the defect type which exists at lower concentrations at high x: Obviously, $R_{b/VSi}^{th}(\Delta E)$ fails to explain the experimental the measured ratio curve $R(\Delta E, 0.04)$ which exhibits a clearly stronger enhancement than caused by the extinction of V_{Si}. Contrariwise, the behavior of $R(\Delta E, 0.04)$ is well explained by the ratio curve $R_{b/VMn}^{th}(\Delta E)$. The differences for Doppler shifts $\Delta E < 3.8$ keV are caused by mainly two simplifications used within the calculations: As investigated for vacancies in Al by Calloni et al. [83], at

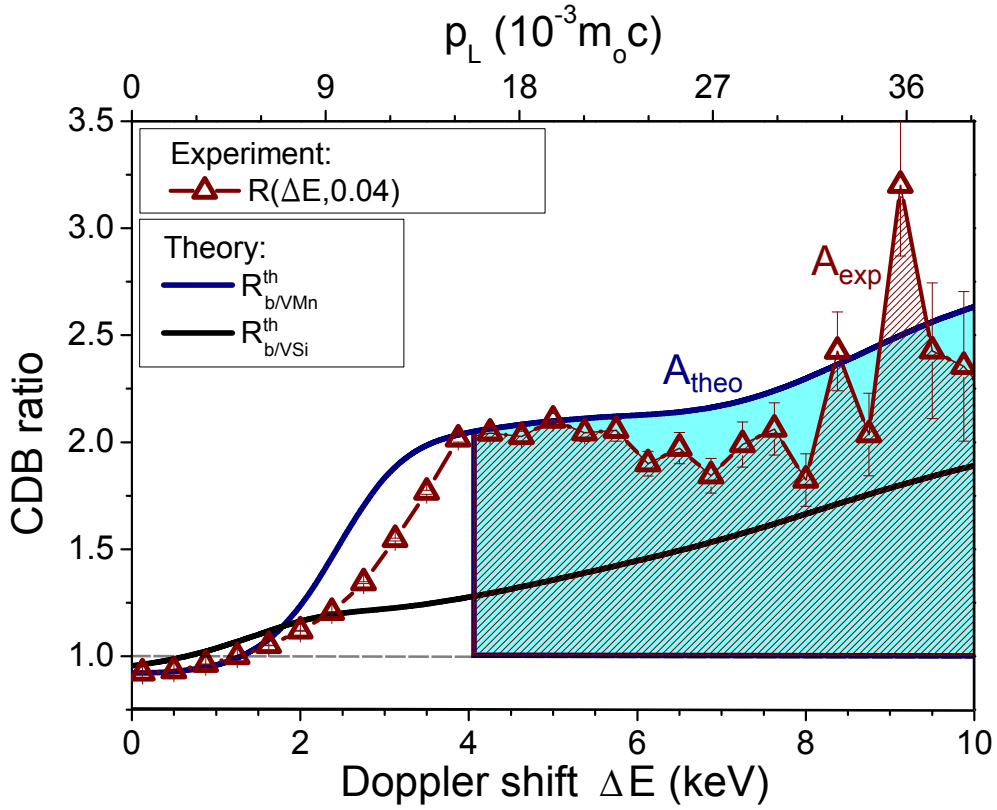

Figure 5.7: The experimental CDB ratio curve $R(\Delta E, 0.04)$ of OFZ 83-3-2-1 ($x = 0.04$) to OFZ 65-3-3 ($x = -0.01$) (see figure 5.5) in comparison with calculated CDB ratio curves. The calculated ratio curves $R^{\mathrm{th}}_{b/VMn}(\Delta E)$ and $R^{\mathrm{th}}_{b/VSi}(\Delta E)$ for annihilation in defect free MnSi were divided by two different theoretical reference spectra corresponding to annihilation in $\mathrm{V_{Mn}}$ and $\mathrm{V_{Si}}$, respectively. The ratio of the hatched to the colored area $A_{\mathrm{exp}}/A_{\mathrm{theo}} = 0.926$ was used for the determination of the concentration c_{VMn}.

these low Doppler shifts the exact treatment of valence electrons within band structure calculations and an accurate modeling of the lattice relaxation around vacancies have to be accounted for in order to precisely describe CDB spectra. For $\Delta E > 4\,\mathrm{keV}$ the annihilation with core electrons gets dominant, which generally are well described by the applied atomic superposition method [76, 81, 82, 84, 86]. The small differences between the calculated and experimental ratio curves for this high momentum area of the CDB spectra are mainly attributed to different probability for the annihilation with core electrons due to a residual concentration c_{VMn} in OFZ 83-3-2-1 with $x = 0.04$. It is concluded that c_{VMn} decreases with increasing x. For $x \leq 0.00$, i. e. in OFZ 65-3-3 and OFZ 66-3-3, all positrons annihilate in $\mathrm{V_{Mn}}$ due to saturation trapping caused by high values of c_{VMn}. For higher x, an increasing fraction of the positrons annihilates in defect free bulk of MnSi.

5.5.2 Concentration of Mn Vacancies Determined by CDBS

The previous results suggest to apply the commonly used trapping model as introduced in section 2.2. Since a transition between only two positron states was detected by CDBS, it is assumed that a fraction η_v of the positrons annihilates in $\mathrm{V_{Mn}}$ and the remaining fraction $\eta_\mathrm{b} = 1 - \eta_\mathrm{v}$ in defect free bulk MnSi. Following equation 2.9, η_b is given by

$$\eta_\mathrm{b}(x) = \frac{\lambda_\mathrm{b}}{\lambda_\mathrm{b} + \kappa_\mathrm{v}(x)} \tag{5.3}$$

with $1/\lambda_\mathrm{b} = 1/\lambda_\mathrm{b}^\mathrm{th} = 111\,\mathrm{ps}$ as obtained by MIKA Doppler and the trapping rate κ_v of positrons into $\mathrm{V_{Mn}}$. This trapping rate is directly proportional to the concentration of Mn vacancies c_VMn and given by

$$\kappa_\mathrm{v}(x) = \mu_\mathrm{v} \cdot c_\mathrm{VMn}(x) \tag{5.4}$$

with μ_v as trapping coefficient, which in case of a monovacancy amounts to typically $10^{14} - 10^{15}$ 1/s [8, 57]. In the following, $\mu_\mathrm{v} = 5 \cdot 10^{14}$ 1/s will be used as approximation. Consequently,

$$c_\mathrm{VMn}(x) = \frac{\lambda_\mathrm{b}}{\mu_\mathrm{v}} \left(\frac{1}{\eta_\mathrm{b}(x)} - 1 \right) = 1.80 \cdot 10^{-5} \left(\frac{1}{\eta_\mathrm{b}(x)} - 1 \right) \tag{5.5}$$

can be directly calculated after the determination of $\eta_\mathrm{b}(x)$. This could be easily done if two reference samples are measured. One of these should contain such a high amount of defects that all positrons are trapped in $\mathrm{V_{Mn}}$ and annihilate there. In this sample, a reference CDB ratio curve $R_\mathrm{v}(\Delta E)$ for the vacancy state is obtained. The other reference should be a quasi defect free sample, so that all positrons annihilate in the bulk with the characteristic ratio curve $R_\mathrm{b}(\Delta E)$. According to equation 2.12, the CDB ratio curve $R(\Delta E, x)$ of any other sample with an arbitrary c_VMn in between those of the references and fully described by the superposition

$$R(\Delta E, x) = (1 - \eta_\mathrm{b}(x)) \cdot R_\mathrm{v}(\Delta E) + \eta_\mathrm{b}(x) \cdot R_\mathrm{b}(\Delta E) \tag{5.6}$$

with the weighting factor $\eta_\mathrm{b}(x)$. Thus, a determination of $c_\mathrm{VMn}(x)$ using equation 5.5 becomes possible by fitting $\eta_\mathrm{b}(x)$ following equation 5.6.

For the present set of samples it is concluded that $R(\Delta E, -0.01)$ corresponds to annihilation in $\mathrm{V_{Mn}}$ and hence, in the following evaluation

$$R_\mathrm{v}(\Delta E) \stackrel{!}{=} R(\Delta E, -0.01) \tag{5.7}$$

will be assumed. From the present experimental data it is not straightforward to determine $R_\mathrm{b}(\Delta E)$. Since in OFZ 83-3-2-1 with $x = 0.04$ the lowest defect concentration c_VMn was

observed, one could assume $R_\mathrm{b}(\Delta E) \approx R_\mathrm{MnSi}(\Delta E, 0.04)$ in a first approach, which would imply $\eta_\mathrm{b}(x = 0.04)$=1. However, it is not possible to conclude directly that all positrons annihilate in the defect free bulk of MnSi in that sample. For a valid estimation of $\eta_\mathrm{b}(0.04)$ in OFZ 83-3-2-1, the experimental ratio curve $R(\Delta E, 0.04)$ was compared to the calculated one $R^\mathrm{th}_{b/VMn}(\Delta E)$. As can be seen in figure 5.7, both these ratio curves envelope additional areas compared to the reference spectrum which are marked and denoted as A_theo and A_exp, respectively. Here, only the high momentum area of the CDB spectra is considered, i. e. Doppler shifts $4 < \Delta E < 10\,\mathrm{keV}$, where the calculations can be expected to work with high reliability as previously discussed. It is assumed that the differences in the enveloped areas is only caused by a different probability for annihilation with high momentum core electrons due to a small fraction $\eta_\mathrm{v}(0.04)$ of positrons annihilating in $\mathrm{V_{Mn}}$ with a concentration $c(\mathrm{V_{Mn}}, 0.04)$. The areas were evaluated in order to determine $\eta_\mathrm{b}(x = 0.04)$ to

$$\eta_\mathrm{b}(0.04) = \frac{A_\mathrm{exp}}{A_\mathrm{theo}} = 0.926 \pm 0.049 \tag{5.8}$$

which means that 7.4 % of the positrons annihilate in $\mathrm{V_{Mn}}$ in the defect-poor sample OFZ 83-3-2-1. This estimation possibly yields values too high for $\eta_\mathrm{v}(0.04)$ and thus too low for $\eta_\mathrm{b}(0.04)$ since the lattice relaxation in the vicinity of the vacancies was not accounted for. Most likely, a possible lattice relaxation at a vacancy leads to an increased overlap of the positron wavefunction with core electrons from neighboring atoms [83]. This effect, besides the assumed different core electron annihilation probability, would lead to a less enhanced calculated ratio curve $R^\mathrm{th}_{b/VMn}(\Delta E)$. Thus, it would envelope a smaller area A_theo leading to a potential underestimation of $\eta_\mathrm{b}(0.04)$ in the current approach.

Finally, it is possible to obtain the vacancy concentration c_VMn as function of x for all investigated MnSi discs. For the required determination of $\eta_\mathrm{b}(x)$, the experimentally determined CDB weighting factors $a_\mathrm{CDB}(x)$ are used. Following the discussion above

$$\eta_\mathrm{b}(-0.01) = 0.000 \qquad \text{and} \qquad \eta_\mathrm{b}(0.04) = 0.926 \tag{5.9}$$

are assumed and, due to the definition of the CDB weighting factor $a_\mathrm{CDB}(x)$ in equation 5.1,

$$a_\mathrm{CDB}(-0.01) = 0.000 \qquad \text{and} \qquad a_\mathrm{CDB}(0.04) = 1.000 \tag{5.10}$$

are given. This enables the calculation of $\eta_\mathrm{b}(x)$ with the linear relation

$$\eta_\mathrm{b}(x) = 0.926 \cdot a_\mathrm{CDB}(x) \tag{5.11}$$

which then can be used in equation 5.5. The thus obtained values for $c_\mathrm{VMn}(x)$ are shown in figure 5.11, where they are directly compared to results of PALS measurements in the cylinders.

5.6 Complementary PALS at GIPS

5.6.1 Probing Cylinders with PALS

Complementary PALS experiments were conducted on the MnSi cylinders with the diameter of around 5 mm and length of around 20 mm. In standard positron experiments working with a slow positron beam like NEPOMUC or a radioactive nuclide such as a ^{22}Na, the probed sample volume is limited by the kinetic energy of the positrons. Even in the case of β^+-emitters with positron energies of several 100 keV, the mean implantation depth is limited to several 100 μm. Thus, only small volumes close to the surface can be probed. This disadvantage can be overcome at electron accelerators by use of high-energetic bremsstrahlung which generates positrons by pair production. The radiation has excellent penetrability as demonstrated by Selim et al. in strained steels [110–112].

The present experiments were carried out at the GIPS facility [113–115], which is located at the superconducting linear electron accelerator ELBE (Electron Linac for beams with high Brilliance and low Emittance) at the Helmholtz-Zentrum Dresden-Rossendorf. ELBE provides electron bunches with a repetition frequency of 26 MHz and durations < 5 ps, which is a well suited time structure for measuring the positron lifetime. The electrons pass a radiator with an elaborated design [116], which generates bremsstrahlung with an γ-energy E_γ of up to 16 MeV. This radiation passes a beam hardener that discriminates γ-quanta with $E_\gamma < 2$ MeV before entering the experimental chamber with the set-up sketched in figure 5.8. Four pairs of HPGe detectors and time resolving BaF_2 detectors are aligned collinearly around the specimen, which is fixed with a nylon filament. Inside the specimen, positrons are generated by the penetrating γ-quanta. In order to eliminate the high background of γ-quanta, which is a drawback of the applied method, the coincident detection of both γ-quanta is necessary. The present study at GIPS was conducted together with the team of Andreas Wagner after the approval by an international scientific advisory committee. The lifetime spectra, which are analyzed in the following, were obtained by evaluating the time difference between the start signal provided by the linac for events, where both annihilation γ-quanta were detected. In order to suppress the background, only events in a narrow energy range around m_0c^2 were considered.

Thus obtained lifetime spectra are shown in figure 5.10 from a single BaF_2 detector which was run in coincidence with a HPGe detector. One of the four HPGe detectors showed results which clearly disagreed from those of the other ones and hence, only three pairs were considered in the evaluation. The complete quantitative analysis was made for all these detectors separately. The final results are summarized by their average values, e. g., in figures 5.9, 5.10 and 5.11. The given errors are always the standard deviations from these averaged mean values. In the lifetime spectra, the increase for times $t < 0$ ns is determined by the time resolution function which is a single Gaussian in the simplest

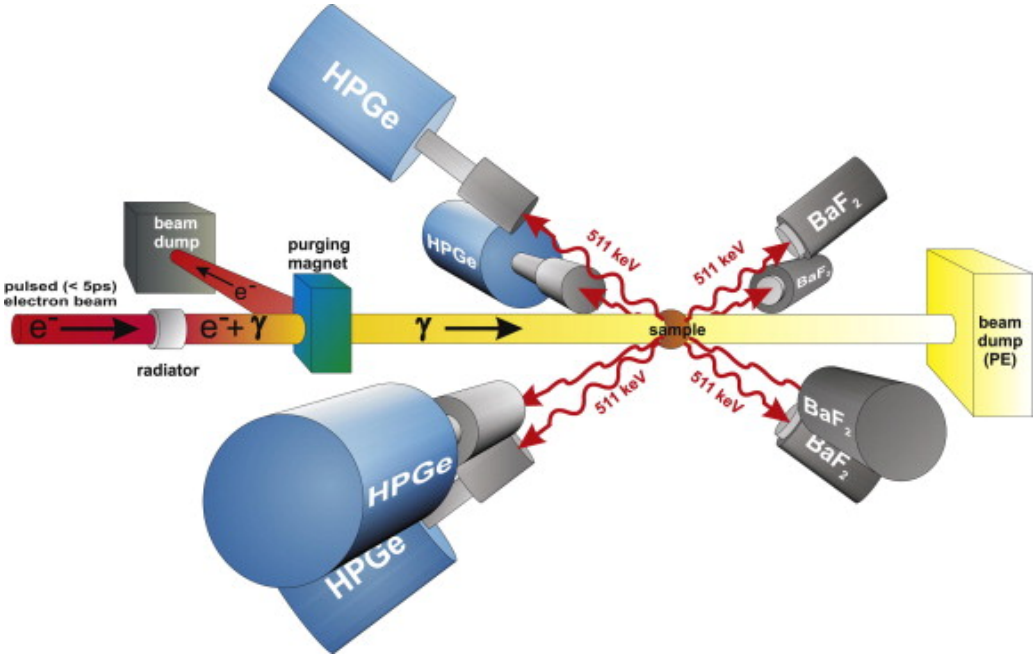

Figure 5.8: Experimental set-up for probing MnSi cylinders by PALS. Positrons were generated in the samples by pair production after implantation of high-energetic bremsstrahlung from a pulsed electron beam. Up to four pairs of HPGe and BaF_2 detectors can be used for a coincident detection of annihilation γ-quanta (figure reprinted from [117]).

case or mostly a sum of Gaussians as described in section 2.3.3. Within the fit model applied for the present spectra, the resolution function was chosen as simple as possible. A superposition of three Gaussians was necessary in order to obtain fits which describe the data in an acceptable way. Their widths, intensities and time zeros were fitted for each specimen individually, since the time resolution at GIPS is well known to depend on the sample size as described by Butterling [118]. Approximately, the time resolution is given by two dominant Gaussians with widths of around 200 and 240 ns.

5.6.2 Concentration of Mn Vacancies Determined by PALS

All detected PALS spectra are shown in figure 5.10 and their respective mean positron lifetimes τ_{mean} in dependency of the initial Mn excess x are plotted in figure 5.9. The observed $\tau_{\mathrm{mean}}(x)$ dependency can be characterized as follows. For OFZ 65 and OFZ 66, i. e. $x \leq 0.00$, nearly identical values are detected, then a decrease is exhibited by $\tau_{\mathrm{mean}}(x)$ until the minimal value is reached at $x = 0.04$ in OFZ 83. This decrease corresponds to a lower concentration of open volume defects and hence, the general behavior of $\tau_{\mathrm{mean}}(x)$ well agrees with the (C)DBS results discussed in the previous sections. Thus, the behavior in the cylinders is also caused by a decrease of c_{VMn} with increasing x.

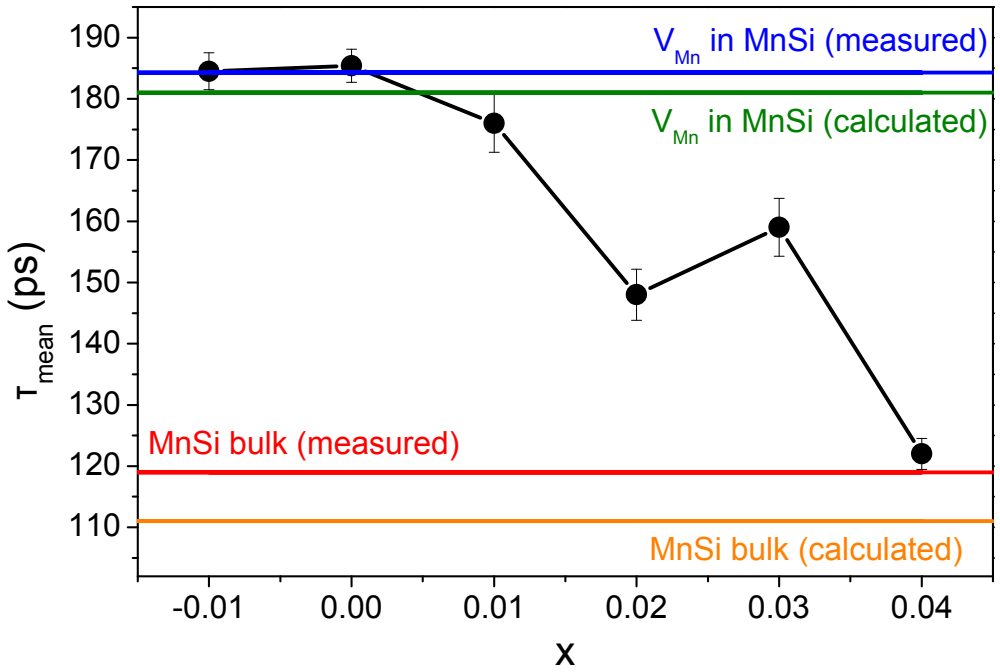

Figure 5.9: Mean positron lifetimes τ_{mean} as function of the initial Mn excess x in MnSi cylinders measured at the GIPS facility. The experimental values were obtained from the fits shown in figure 5.10. The experimental and calculated characteristic positron lifetimes for defect free MnSi and V_{Mn} are plotted, too.

Vacancy-rich and Vacancy-poor Specimens – OFZ 65, OFZ 66 and OFZ 83

For the further evaluation of the lifetime spectra, the LT10 program [119–121] was used for fitting. As seen in figure 5.10, the exponential decay of positrons in OFZ 65 and OFZ 66 ($x = -0.01$ and 0.00, respectively) only exhibits one slope and hence, all positrons annihilate with the same characteristic rate λ. A fit for OFZ 65 yields a value of $\frac{1}{\lambda} = \tau = 184.5 \pm 3.0\,\text{ps}$, which well agrees with the calculated value of $\tau_{\text{VMn}}^{\text{th}} = 181\,\text{ps}$ reported in section 5.5.1. It is concluded that all positrons in OFZ 65 annihilate in V_{Mn} and $\tau_{\text{VMn}}^{\text{exp}} = 184.5 \pm 4.3\,\text{ps}$. Evaluating the lifetime spectra of OFZ 66 in the same way, yields in a quasi identical characteristic lifetime of $\tau = 185.4 \pm 2.7\,\text{ps}$. Thus, also in this sample all positrons annihilate in V_{Mn}.

The spectrum of OFZ 83 with $x = 0.04$ exhibits a faster decay and there, positrons annihilate with a higher rate than in OFZ 65 or OFZ 66, which leads to a much lower value of $\tau_{\text{mean}} = 122 \pm 2.5\,\text{ps}$. However, the spectrum for $x = 0.04$ cannot be fitted with a single component. A two-component fit reveals that a short lifetime of $\tau_1 < \tau_{\text{mean}}$ clearly dominates the spectrum. Annihilation with $\tau_{\text{VMn}}^{\text{exp}} = 184.5\,\text{ps}$ additionally contributes, but only with an intensity of $I_2 = 8.5 \pm 4.4\,\%$. According to the trapping model, as described

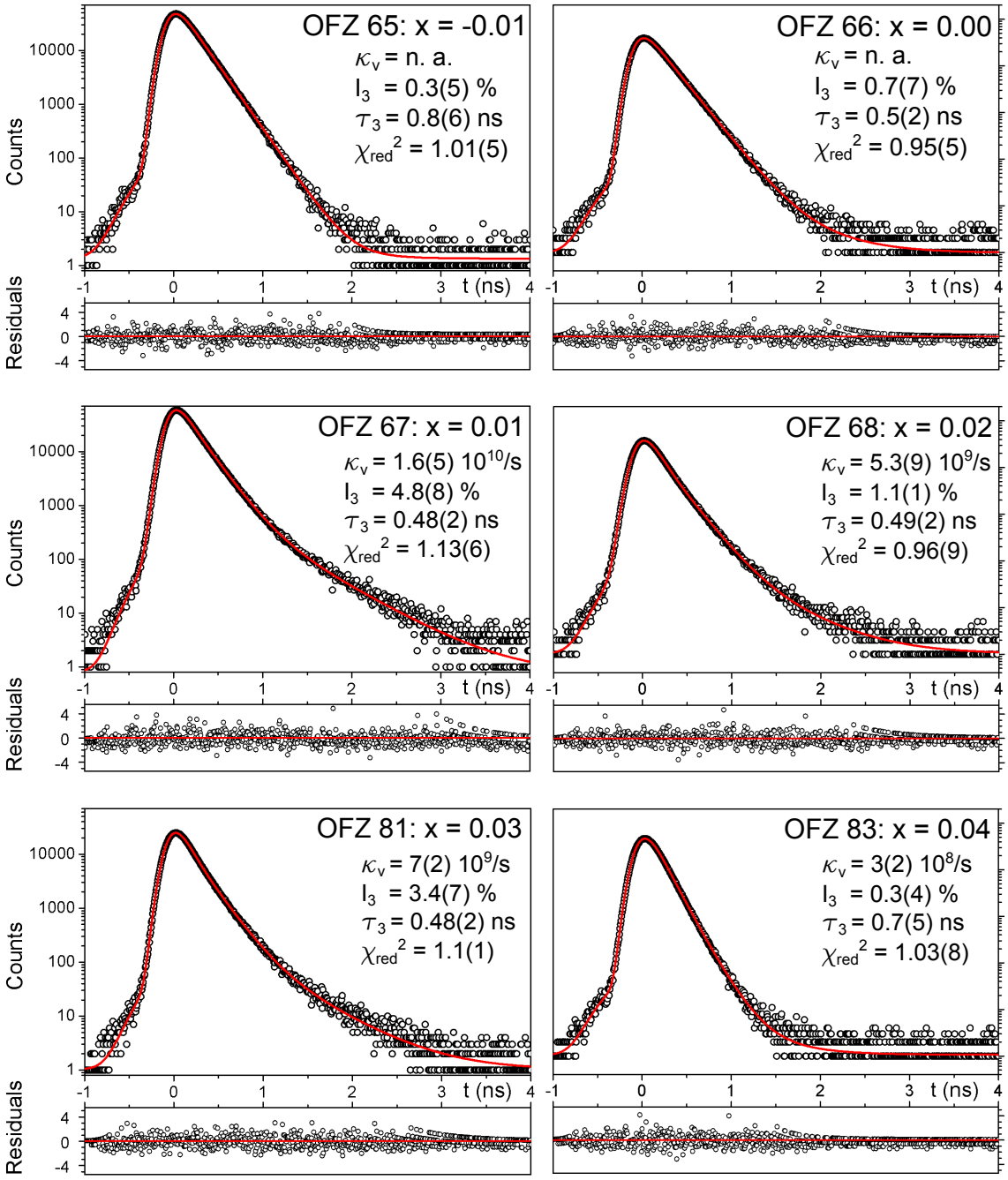

Figure 5.10: Positron lifetime spectra, measured by a single detector, of MnSi cylinders with varying x: Solid lines are fits to the data; the respective residuals are shown below the PALS spectra. The values yielded by the fits given in the plot, including χ^2_{red}, are means obtained after averaging over the results of all three detectors used in this experiment.

in section 2.2, the experimentally detected lifetime

$$\tau_1(x) = \frac{1}{1/\tau_\mathrm{b} + \kappa_\mathrm{v}(x)} \tag{5.12}$$

is characteristic for positrons annihilating in defect free MnSi. It is shorter than the actual bulk lifetime τ_b due to the trapping of positrons into $\mathrm{V_{Mn}}$ with the characteristic rate κ_v defined in equation 5.4. Commonly, τ_1 is notated as reduced bulk lifetime. With a fit based on the trapping model as implemented in LT10, $\tau_\mathrm{b}^\mathrm{exp} = 119.0 \pm 2.7\,\mathrm{ps}$ and $\kappa_\mathrm{v} = (3.1 \pm 2.3) \cdot 10^8/\mathrm{s}$ were obtained. The measured $\tau_\mathrm{b}^\mathrm{exp}$ fairly well agrees with the calculated $\tau_\mathrm{b}^\mathrm{th} = 111\,\mathrm{ps}$. The difference between both is most likely caused by small systematic errors in the PALS experiments. With $\mu_\mathrm{v} = 5 \cdot 10^{14}\ 1/\mathrm{s}$ as assumed in section 5.5.2 and following equation 5.4, one can calculate

$$c_\mathrm{VMn}(x) = \frac{\kappa_\mathrm{v}(x)}{5 \cdot 10^{14}/\mathrm{s}} \tag{5.13}$$

which yields $c_\mathrm{VMn}(0.04) = (6.3 \pm 4.7) \cdot 10^{-7}$ for OFZ 83. Positron trapping in the vacancies $\mathrm{V_{Mn}}$ with the detected rate κ_v leads to the observed contribution of $\tau_\mathrm{VMn}^\mathrm{exp}$ to the lifetime spectra with the intensity I_2. For OFZ 65 and OFZ 66 no contribution of the annihilation in bulk could be detected and hence, it is not possible to extract values for κ_v and c_VMn. Moreover, in the fits of OFZ 65, 66 and 83, a potentially present longer-living component τ_3 with an intensity I_3 was accounted for, which resulted in the values given in figure 5.10. This component, however, did not affect all the other results presented above due to the low values of I_3 compatible with zero with respect to the high scattering of I_3 and τ_3.

Specimens of the Transition Range – OFZ 67, OFZ 68 and OFZ 81

Obviously, the raw spectra for $0.01 \geq x \geq 0.03$ reveal contributions of several positron sates, where positrons annihilate with different rates. For $t > 1.5\,\mathrm{ns}$ a long-living lifetime component is clearly visible. In the analysis of OFZ 67, OFZ 68 and OFZ 81, the applied fit model is based on the trapping model and accounted for annihilation in defect free bulk of MnSi with a characteristic lifetime τ_b and annihilation in Mn vacancies $\mathrm{V_{Mn}}$ with τ_v. Therefore, the values $\tau_\mathrm{VMn}^\mathrm{exp} = 184.5\,\mathrm{ps}$ and $\tau_\mathrm{b}^\mathrm{exp} = 119.0\,\mathrm{ps}$ measured in OFZ 65 and OFZ 83 respectively, were fixed in the fitting procedure. The trapping rate κ_v was a free parameter of the fit. Additionally, a third component was considered due to the long-living component visible in the respective lifetime spectra. The intensity of this component I_3 and the respective lifetime τ_3 were free parameters of the fit. The thus obtained fits are shown in figure 5.10 together with the respective χ^2_red and the main results, i. e. κ_v, τ_3 and I_3. By use of equation 5.13, $c_\mathrm{VMn}(x)$ was determined and will be discussed in the following section. Although small, the origin of the third component remains unclear. Such a long-

living component would imply the presence of clusters of more than 15 vacancies [57]. The presence of such clusters in the melt zoned crystals would not be expected. A similar component was observed in well annealed, defect free Fe at the same set-up [114] and thus, these long-living components are most likely an artifact in the measurements.

5.7 Concentration of Mn Vacancies and Mn Content

The concentration $c_{\mathrm{VMn}}(x)$ of Mn vacancies, as measured by CDBS in the discs and by PALS in the cylinders and shown in figure 5.11, is analyzed. As already mentioned, for $x \leq 0.00$ quasi all positrons annihilate in $\mathrm{V_{Mn}}$. A tiny difference between $x = -0.01$ and $x = 0.00$, namely an increase of the (C)DBS weighting factors at $x = 0.00$ seen in figure 5.6, enables to determine $c_{\mathrm{VMn}}(0.00) \approx 1 \cdot 10^{-3}$ per atom which is a lower limit for $c_{\mathrm{VMn}}(-0.01)$. At $x = 0.01$, a drop of c_{VMn} by more than one order of magnitude is observed. With further increasing x, c_{VMn} decreases and finally approaches the lower sensitivity limit of PAS at $x = 0.04$. The concentrations $c_{\mathrm{VMn}}(x)$ measured in the discs and cylinders are very similar. Thus, the distribution of V_{Mn} is homogeneous in the crystals.

The macroscopic $RRR(x)$ shown in figure 5.2 can be further interpreted based on the PAS results. Discs from the end, which were investigated by (C)DBS, showed a maximal RRR at $x = 0.01$ corresponding to a minimal absolute concentration of lattice defects. At $x = 0.01$, $c_{\mathrm{VMn}}(x)$ exhibits no minimum, but – compared to the crystals grown with $x \leq 0.00$ – a strongly reduced concentration of Mn vacancies. It is assumed that the highest crystal quality with a composition close to stoichiometry is obtained at $x = 0.01$. For lower x, the crystals are strongly Mn deficient as revealed by the high concentration of Mn vacancies. These are even detected – at relatively small concentrations – for Mn-rich samples. For these, the RRR reduces whereas $c_{\mathrm{VMn}}(x)$ decreases with increasing x. Moreover, the changes of $c_{\mathrm{VMn}}(x)$ in this regime are relatively small. Hence, the low RRR values are attributed to Mn antisite atoms on the Si sublattice or even more complex kind of defects which lead to an increased Mn content in the lattice. Si vacancies were not found in this regime and hence, are unlikely to influence the RRR.

This interpretation of the $RRR(x)$ and $c_{\mathrm{VMn}}(x)$ is corroborated by the theoretical effective formation energies of point defects in MnSi [102], which were calculated by Michael Leitner (Technische Universität München). In non-stoichiometric regimes, antisite atoms on the sublattices of the deficient elements are energetic favorable: Either, for low x, Si antisite atoms on the Mn sublattice or, for high x, Mn antisite atoms on the Si sublattice are present. In any configuration, i. e. for Mn deficiency, stoichiometry and Si deficiency, the effective formation energies for monovacancies on the Mn sublattice are lower than on the Si sublattice. In the regime of Mn deficiency, the effective formation energy of $\mathrm{V_{Mn}}$ amounts only to 0.5 eV. The formation energy increases to 1.3 eV in stoichiometric crystals

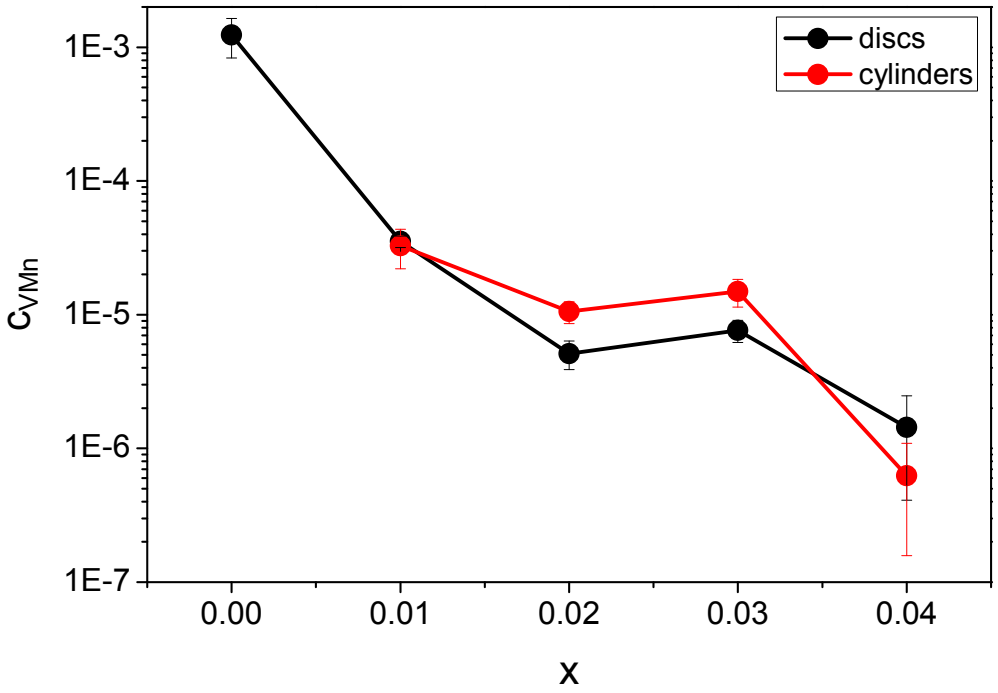

Figure 5.11: Concentration of Mn vacancies c_{VMn} per atom as function of the initial Mn excess x in MnSi crystals. Discs were investigated by CDBS and cylinders by PALS.

and 2.0 eV in Si deficient crystals. This behavior explains the high values of $c_{\mathrm{VMn}}(x)$ for $x \leq 0.00$ and its decrease for $x \geq 0.01$. Moreover, the drop of $c_{\mathrm{VMn}}(x)$ at $x \geq 0.01$ is interpreted as transition from Mn deficiency to a more or less stoichiometric crystal. For Si vacancies, the effective formation energy is at least 2.4 eV and hence, these vacancies could not be detected in the performed experiments. H atoms, which were found in all samples with a similar concentration by PGAA, apparently do not occupy Mn vacancies, since the positron lifetime of 144 ps calculated for this case was not observed in the experiments. Presumably, they are located on interstitial sites or only at the edges of the crystals.

For $x = 0.02$ and $x = 0.03$, at the crystal begin, which was at elevated temperatures for a longer time during preparation, a higher $RRR(x)$ than at the end was found. Thus, one could expect a lower concentration of $\mathrm{V_{Mn}}$ in the cylinders which were probed by PALS than in the end discs. However, $c_{\mathrm{VMn}}(x)$ is even slightly higher in the cylinders. Apparently, the longer annealing at the start did not reduce the vacancy concentration. Thus, the higher RRR at the start suggests that Mn atoms gas out from antisite defects on the Si sublattice during annealing. Presumably, the vacant sites are then occupied by Si atoms leading to a locally high stoichiometry. Such annealing processes did obviously not play a role in crystals with a lower Mn content exhibiting a homogeneous RRR.

5.8 Spatial Homogeneity of Single Crystals

An specifically prepared MnSi single crystal, the so-called gradient crystal OFZ 71, was examined by spatially resolved DBS in order to probe its spatial homogeneity. The initial rod used for the crystal growth of OFZ 71 originally was produced from two different rods with unequal chemical composition. These were fused together in the preparation process of the initial rod, which thus had a Mn excess of $x = -0.01$ at its begin and $x = 0.02$ at its end. From the grown monocrystalline cylinder three discs were analyzed by spatially resolved DBS. OFZ71-3-2-1 was cut longwise the cylinder, OFZ 71-3-1 and OFZ 71-3-3 were cut from the begin and the end of the cylinder, respectively.

Spatially resolved DBS with $E_+ = 29\,\mathrm{keV}$ was conducted according to a mean implantation depth of $1.6\,\mu\mathrm{m}$ and yielded 2D S-parameter maps of the specimens. For each of them, the mean S-parameter S_{avg} was determined by averaging the respective maps. Then, all S-parameters were normalized by S_{avg} (OFZ 71-3-2-1) and thus, the S-parameter maps in figure 5.12 were generated. The absolute S-parameters of OFZ 71-3-2-1 correspond to

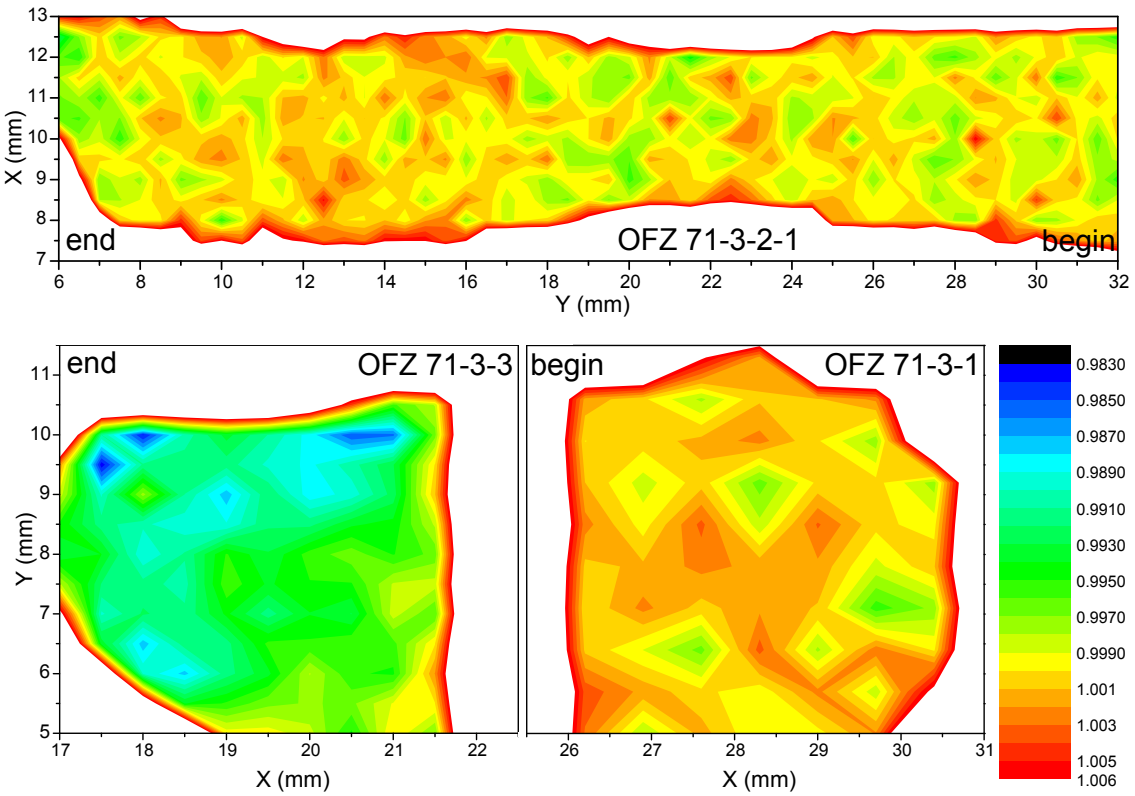

Figure 5.12: 2D S-parameter maps of the gradient crystal OFZ 71 ($E_+ = 29\,\mathrm{keV}$): Discs cut alongside the cylinder (OFZ 71-3-2-1), from its begin (OFZ 71-3-1) and from its end (OFZ 71-3-3) were investigated; the statistical error for S is $\sigma_{stat} = 1.8 \cdot 10^{-3}$.

Sample	Position	x	S_{avg}	$\sigma_{\mathrm{S,avg}}$
OFZ 71-3-1	begin	-0.01	1.0004(2)	$1.9 \cdot 10^{-3}$
OFZ 71-3-2-1	longwise	-0.01 – 0.02	1.0000(2)	$1.9 \cdot 10^{-3}$
OFZ 71-3-3	end	0.02	0.9937(4)	$4.0 \cdot 10^{-3}$

Table 5.2: Investigated discs stemming from the gradient crystal OFZ 71: Their means S_{avg} and according standard variations σ_S were determined from the maps in figure 5.12.

$x = 0.005$ when comparing to the S-parameters measured in the other MnSi crystals. In order to analyze the spatial variation, the standard deviation $\sigma_{\mathrm{S,avg}}$ from this mean S_{avg} was calculated for each sample; the results are given in table 5.2. In these measurements, the statistical error of a single S-parameter σ_{stat} was $1.8 \cdot 10^{-3}$, which was obtained from a series of measurements at constant X,Y and E_+.

Both samples OFZ 71-3-2-1 and OFZ 71-3-1 exhibit an equal S_{avg} within the statistical error. All detected S-parameters scatter in a range of 1.000 ± 0.005. The respective standard deviation $\sigma_{\mathrm{S,avg}}$ was calculated from all points measured on the respective discs. This fluctuation is merely attributed to the statistical variation, since the respective standard deviation $\sigma_{\mathrm{S,avg}}$ is nearly the same as the statistical error σ_{stat}. Hence, both discs show a homogeneous S-parameter distribution. Due to the applied preparation process one might expect a spatial dependency of S in the fusing zone with its non-constant x. This zone is located at around $16 < Y < 26\,\mathrm{mm}$ in between the two different initial rods with $x = -0.01$ and $x = 0.02$. But even in this region, S is absolutely homogeneous. Compared to these samples, S_{avg} is significantly lower in OFZ 71-3-3 with $\sigma_{\mathrm{S,avg}}$ twice as large. Moreover, the according S-parameter map reveals a spatial inhomogeneity: A larger variation, in a range between 0.983 and 1.003, than in the other samples is seen. Moreover, S clearly decreases towards one edge of the wafer in the region at $X \approx 18$ and $20.5\,\mathrm{mm}$ and $Y \approx 9.5\,\mathrm{mm}$. Thus, one would expect a decrease of the S-parameter in OFZ 71-3-2-1 towards the end of the rod. However, this disc was found to show a spatially homogeneous S-parameter. There is only a tiny hind for an systematic decrease of S at the end of OFZ 71 3-2-1, where in a small region $X \approx 11.5\,\mathrm{mm}$ and $Y \approx 6.0\,\mathrm{mm}$ several relatively low S-parameters around 0.995 were measured at the edge of the scan area. This could indicate the transition to OFZ 71-3-3, which was cut from the cylinder close to that region and hence, leads to a consistent result of the spatially resolved DBS measurements.

Apparently, no spatial variation of S was detected even though inhomogeneities could be expected in the probed gradient crystal. These were only detected to a small extent at the end of the crystal and probably caused by edge effects. Thus, it is concluded that V_{Mn} have homogeneously distributed which is quite surprising. From the previous results,

a high concentration of V_{Mn} is expected at the Mn deficient start ($x = -0.01$) of OFZ 71. At the Mn-rich end ($x = 0.02$), the concentration of V_{Mn} should be clearly reduced. In contrast to S, the RRR showed a spatially differing behavior: $RRR \approx 50$ at the begin and $RRR \approx 100$ at the end of OFZ 71 were measured. According to the $RRR\,(x)$ data in figure 5.2, this observation indicates Mn deficiency at the begin and nearly stoichiometry at the end of OFZ 71. Due to the previously found $RRR\,(x)$ dependency, one would expect a similar, relatively low RRR for the begin and the end caused by either Mn deficiency or Mn excess, respectively. In deed, at the begin the RRR is low and in agreement with the observed $RRR\,(x)$ behavior. However, at the end, the RRR is relatively high and indicates a more or less stoichiometric crystal there. This observation suggests that Mn atoms have left from antisites on the Si sublattice at the crystal end. Possibly, this process was accelerated by the relatively high, homogeneous concentration of V_{Mn} also observed at the Mn rich end. Either these Mn atoms might have reduced the total concentration of V_{Mn} or diffused out during float zoning leading to stoichiometry at the end.

5.9 Conclusion

MnSi crystals prepared by optical float zoning have been investigated by PAS using PALS and (C)DBS in order to reveal the role of point defects in this important system. Various crystals were analyzed with a varying Mn content in the first step of preparation. A slight, initial Mn excess was expected to lead to stoichiometric crystals, since out gassing of Mn is observed during the crystal growth by optical float zoning. Actually, DBS and CDBS results revealed a reduction of the concentration of open volume defects with increasing Mn content. These defects could be clearly identified as Mn vacancies by comparing experimental and calculated CDB spectra. The initial Mn excess in the crystal preparation suppresses the presence of Mn vacancies and does not lead to the formation of Si vacancies. The concentration of Mn vacancies as measured by CDBS in end discs was in excellent agreement with the PALS results from cylinders of the crystals. Hence, the spatial distribution of the Mn vacancies is homogeneous. This was even the case for crystals grown from initial rods with different chemical composition at their begin and their end. The comparison of these PAS results with studies of coworkers, namely measurements of the residual resistivity ratio and calculations on the formation of point defects, revealed that the observed reduction of the Mn vacancy concentration corresponds to a transition from Mn deficient to Mn rich crystals. A drop of this vacancy concentration with increasing Mn content and a homogeneously high residual resistivity ratio appear to display a state close to stoichiometry in MnSi crystals. Thus, the enhanced interpretation of the residual resistivity ratio, which serves as routine quality check for MnSi crystals, with respect to point defects leads to an improved understanding of single crystal growth.

6 Chapter 6
Oxygen Deficiency in Thin YBCO Films

$YBa_2Cu_3O_{7-\delta}$ (YBCO) [37–39] is a prominent representative of the large class of oxides based on the perovskite structure such as $SrTiO_3$ (STO) [122, 123] or $LaAlO_3$ [124, 125]. Such materials are of high interest and great importance due to their outstanding electric and magnetic properties. These properties are often defined by the oxygen content in the system like it is the case for YBCO, which exhibits High-Temperature Superconductivity (HTSC) when a certain amount of oxygen is present in the crystal. With the emergence and ongoing improvement of the Pulsed Laser Deposition (PLD) technique [126] for thin film growth, the routine preparation of single-crystalline films of such complex materials became feasible. Thus obtained high-quality specimens facilitate the basic understanding of complex phenomena and open a wide range of applications, for example power transmission through superconducting wires [43] or fault current limiters [44] and as important component in high field magnets [45].

In the present work, monocrystalline thin YBCO films grown by PLD were studied by (C)DBS using the NEPOMUC positron beam. Theoretical and experimental studies were combined in order to investigate the microscopic behavior of positrons in the complex crystal structure and to examine their potential for probing oxygen deficiency. The variety of experimental features – in particular the high countrate, the small beam spot size and the wide accessible temperature range as described in chapter 4 – at the NEPOMUC CDB spectrometer was used for a comprehensive study. The performed experiments involved investigations of the interface to the substrate by (C)DBS depth profiling, of the lateral homogeneity by spatially resolved DBS measurements and of the high-temperature behavior during in-situ DBS at elevated temperatures.

6.1 The High-Temperature Superconductor $YBa_2Cu_3O_{7-\delta}$

6.1.1 Role of the Oxygen Deficiency δ

The crystal structure of the cuprate $YBa_2Cu_3O_{7-\delta}$ depends on the oxygen deficiency δ which lies in a range $0 \leq \delta \leq 1$. The unit cell of superconducting $YBa_2Cu_3O_7$ is orthorhombic ($a = 0.383\,\text{nm}$, $b = 0.388\,\text{nm}$, $c = 1.168\,\text{nm}$ [127]) and can be described as stack of three perovskite structured cells, which are stapled along the c-axis: A single $YCuO_3$ cell is sandwiched by two $BaCuO_2$ cells as can be seen in fig. 6.1. Their lower oxygen content results in the formation of CuO chains in the basal plane between the Ba cells instead of the CuO_2 planes which sandwich the Y cell. Increasing δ above $\delta \approx 0.7$ leads to a tetragonal and antiferromagnetic phase, where the O atoms in the basal plane rearrange and randomly distribute along the a- and b-axis between the Cu atoms. This plane becomes completely oxygen deficient in insulating $YBa_2Cu_3O_6$, where the lattice parameters are $a = b = 0.386\,\text{nm}$ and $c = 1.182\,\text{nm}$ [128].

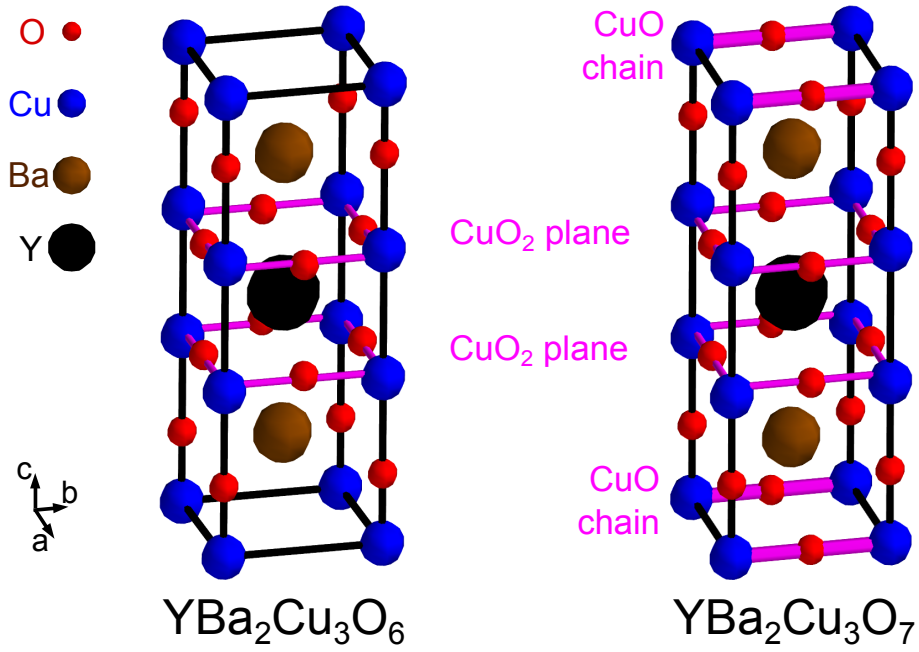

Figure 6.1: Unit cells of the insulating tetragonal $YBa_2Cu_3O_6$ and the superconducting orthorhombic $YBa_2Cu_3O_7$ phase: The additional oxygen atoms preferably occupy sites along the b-axis by forming of CuO chains.

Superconductivity with a critical temperature T_c above $92\,K$ was found in the YBCO system [37,38] shortly after the discovery of HTSC in cuprates [39]. The dependence of T_c on δ in the YBCO films investigated in this study is plotted in figure 6.2. It well coincides

with dependencies reported in literature, e. g., by Zaleski et al. [129]. For a low δ of around 0.2, a maximal $T_c = 90\,\mathrm{K}$ is found in the investigated thin film samples. Between δ=0.5 and δ=0.7, T_c exhibits a plateau at 60 K. For further increasing δ, T_c decreases until the superconductive behavior vanishes. In figure 6.2, data of Cava et al. [130] are shown for comparison. These were obtained in sintered bulk YBCO samples and show a similar qualitative behavior. However, the plateau at 60 K is shifted to lower values of δ. In order to understand the dependency of T_c on δ, one must consider the origin of the HTSC in YBCO. Its occurrence is explained by the formation of Cooper pairs [131, 132] from holes in the CuO_2 planes [133]. The dependence of T_c and the hole doping p, which denotes the number of holes per Cu atom in the CuO_2 plane, is commonly described by an empirical formula [134]:

$$\frac{T_c}{T_{c,max}} = 1 - 82.6(p - 0.16)^2 \tag{6.1}$$

The hole doping p in the CuO_2 planes depends on both the oxygen deficiency and ordering in CuO chains (e. g. [129, 135, 136]). Moreover, HTSC seems to be intertwined to a Charge-Density-Wave (CDW) order [40] as it is strongly indicated by the recent discovery of CDW in high quality YBCO bulk crystals [41, 42]. This complexity of the HTSC phase in YBCO leads to an ambiguous correlation between T_c and δ. Hence, the understanding of underlying processes and phenomena requires a comprehensive characterization of the

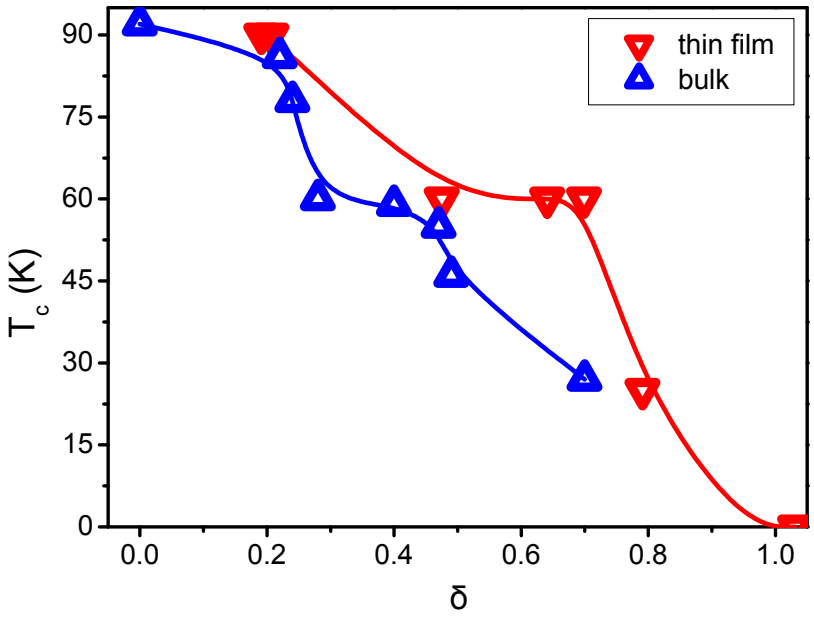

Figure 6.2: Dependency of the critical temperature T_c on the oxygen deficiency δ in sintered bulk $YBa_2Cu_3O_{7-\delta}$ (data from [130]) and the investigated thin film samples. The solid lines serve as guides to the eye.

oxygen deficiency δ in high quality YBCO samples. The amount of oxygen vacancies is a decisive material parameter for HTSC in YBCO but also in other materials based on cuprates ($T_c > 130\,K$ in $HgBa_2CuO_{4+\delta}$ [137]) or on iron-oxypnictides (T_c=55 K for $SmO_{1-x}F_xFeAs$ [138, 139]).

6.1.2 PAS on YBCO - Short Overview of Previous Studies

Positrons have been widely used in order to study YBCO bulk materials at the end of the 1980s and in the beginning of the 1990s (see e. g. review by Puska and Nieminen [2]). The main focus of these studies was to confirm the existence of a theoretically predicted Fermi surface [140–142] by 2D-ACAR measurements [143–148]. However, only slight anisotropies were found in the 2D-ACAR spectra and hence, it was concluded that electrons from the Fermi surface only weakly contribute to the positron annihilation. A further goal of PAS in YBCO was to identify changes in the electronic structure related to the transition to superconductivity. This would possibly allow a deeper understanding of the mechanism leading to this transition. However, no conclusive results were found there.

Since the YBCO system exhibits a complicated crystal structure, it is crucial to combine experiments with theoretical considerations for a proper interpretation of experimental data. Thus, numerous publications treat the positron annihilation in YBCO theoretically. The consideration of the positron trapping in metallic and oxygen vacancies as done in a few studies, e. g. in [149–151] is of high interest for the present study. From these investigations, it is known that metallic vacancies form deep potential wells for positrons with binding energies of around 1.0 eV or more. Moreover, delocalized positrons favor the region in the basal plane between the Cu(O) chains in the defect free lattice.

Combining these theoretical results with experimental studies demonstrates that positrons are very sensitive to the oxygen content in YBCO. This is obvious from calculated and experimental positron lifetimes summarized by Puska and Nieminen in their review article [2]. As seen in figure 6.3, the positron lifetime decreases with increasing oxygen content. The high affinity of the positrons to the CuO chains with their variable oxygen content causes the dependency. This phenomenon also leads to a high sensitivity of DBS results on the oxygen deficiency [143, 144, 152, 153]. It is known from PALS (e. g. [149, 150, 154, 155]) and DBS (e. g. [152, 153]) measurements that the sample quality and the applied method of preparation strongly influence PAS results in YBCO. In sintered YBCO bulk samples, e. g., positrons are trapped in various kinds of crystal imperfections, like grain boundaries and metallic vacancies. Such effects have to be investigated separately for the present set of high-quality thin film samples.

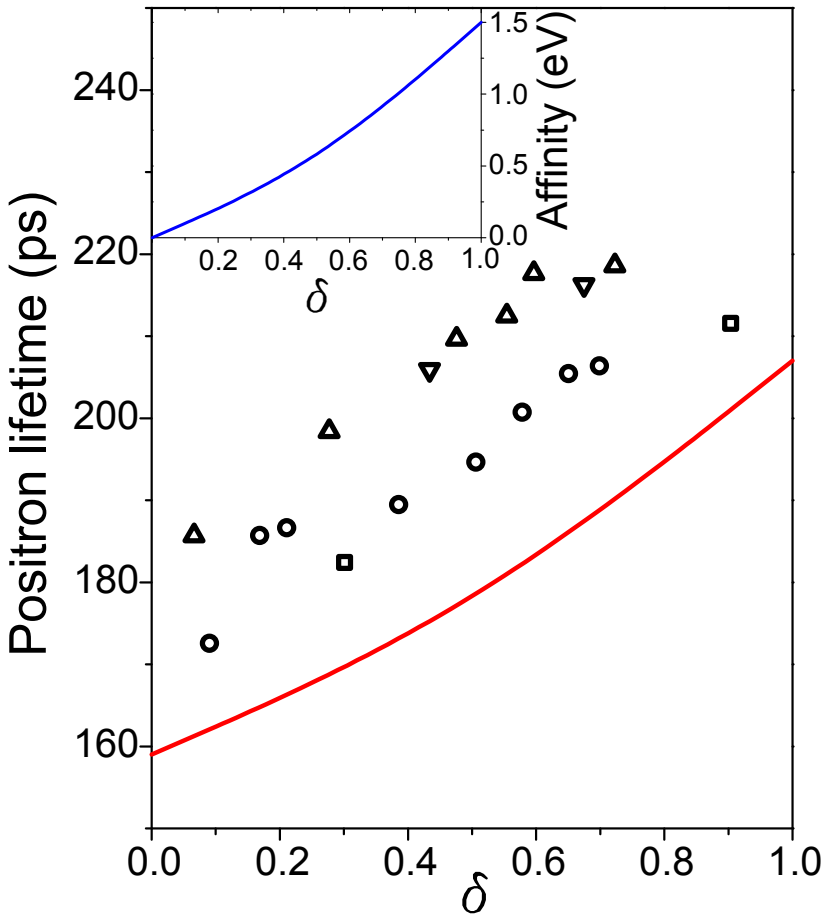

Figure 6.3: Calculated (line) and experimental positron lifetimes (data points) in $YBa_2Cu_3O_{7-\delta}$ as function of the oxygen content. The inset shows the calculated affinity of positrons to the basal plane of $YBa_2Cu_3O_{7-\delta}$ in dependence of the oxygen concentration. Data are taken from [2] and summarize various studies.

6.2 Calculation of Positron States in YBCO

Previous theoretical studies considering the positron annihilation in YBCO were focusing on positron lifetimes or ACAR spectra. Thus, these could not be used directly for the current study with its focus onto the (C)DBS technique. In order to obtain a broad set of theoretical CDB spectra for a reliable interpretation of the experimental data, firstly positron states in the YBCO system were calculated by use of the MIKA Doppler software described in chapter 3. The annihilation in $YBa_2Cu_3O_6$ and $YBa_2Cu_3O_7$ was systematically investigated. Results for the positron lifetime and the Doppler broadening of the annihilation radiation were evaluated. The calculations also enable visualizing the positron behavior on a microscopic level.

Defect Free YBCO – Influence of Oxygen Deficiency and Positron Mobility

For a start, the positron annihilation in defect free $YBa_2Cu_3O_6$ and $YBa_2Cu_3O_7$ was considered. Supercells of $3 \times 3 \times 1$ unit cells were modeled under the approximation of a tetragonal phase. Then, calculations of the positron wavefunction $\Psi_+(\mathbf{r})$ were performed on a mesh of $128 \times 128 \times 128$ grid points. The thus obtained positron probability densities $|\Psi_+(\mathbf{r})|^2$ are shown in figure 6.4 by plots of their isosurfaces. Obviously, the positron occupies a planar state in the basal plane of defect free YBCO with its varying oxygen deficiency δ. This state is also depicted in figure 6.5 by a 2D plot of $|\Psi_+(\mathbf{r})|^2$ in the basal plane. The found behavior is in agreement to previously published results [2, 143, 150, 151, 156–158]. In table 6.1, the respective lifetimes of the positron states in these ideal lattice structures are given. In $YBa_2Cu_3O_6$, the positron lifetime is nearly 50 ps longer than in $YBa_2Cu_3O_7$. This clear increase with δ is caused by the larger open volume in the completely oxygen deficient basal plane of $YBa_2Cu_3O_6$. It qualitatively well agrees with the increase from 160 to 210 ps calculated by Nieminen et al. [149, 150] as shown in figure 6.3. Quantitative differences are attributed to a different treatment of the electron-positron enhancement. Hence, the applied calculational method yields reasonable results and is well suited for detailed investigations. The respective theoretical CDB spectra will be discussed within section 6.4.2 together with the experimental results.

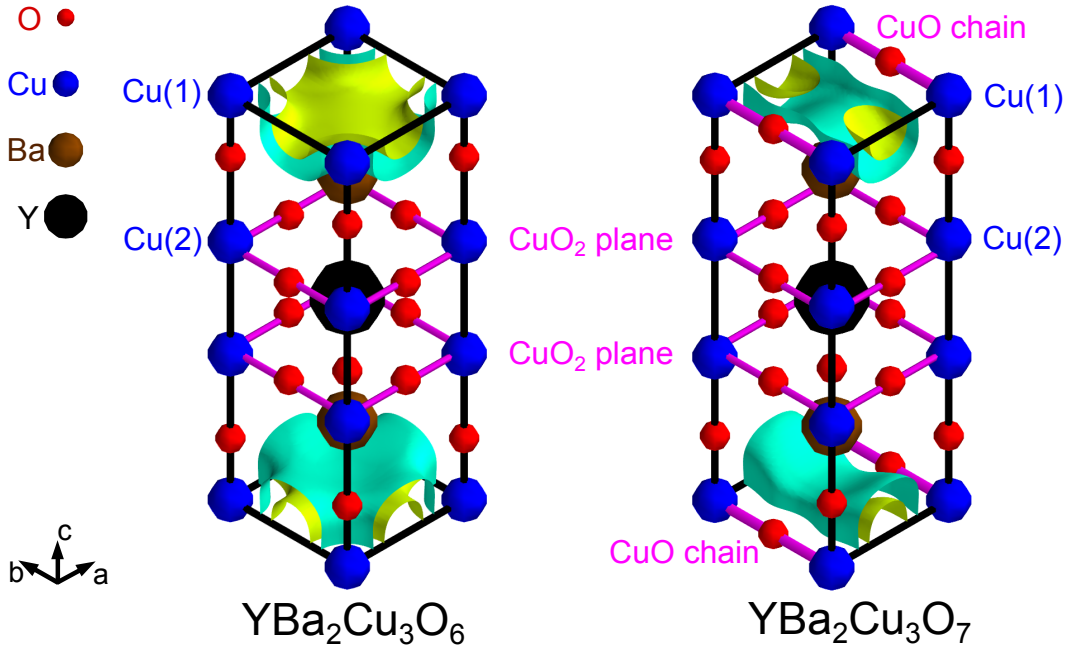

Figure 6.4: Calculated 3D isosurfaces of the positron probability density in $YBa_2Cu_3O_6$ and $YBa_2Cu_3O_7$ (linear scale of the contours) reveal a delocalized positron state in the basal plane with its varying oxygen content.

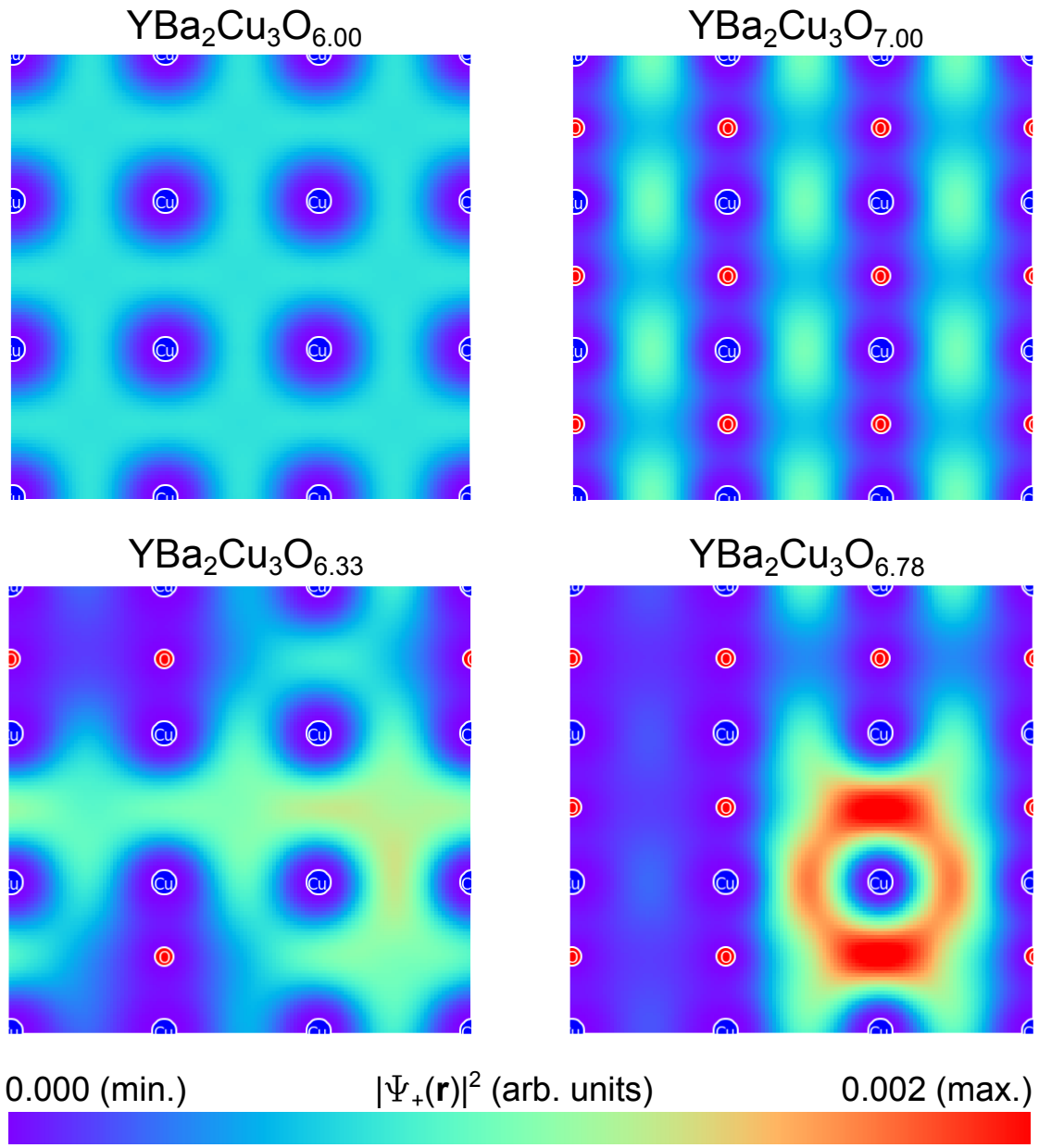

Figure 6.5: Positron probability density in the $YBa_2Cu_3O_{7-\delta}$ basal plane for various oxygen contents. In this plane, positrons probe oxygen deficient sites, which makes them a sensitive nanoprobe for oxygen deficiency.

In order to derive a precise δ dependency from these calculations, configurations in a wide range of δ between 0 and 1 were modeled. In the respective supercells, the δ dependency of the lattice constants was accounted by a linear interpolation of the lattice parameters of $YBa_2Cu_3O_6$ and $YBa_2Cu_3O_7$. All obtained positron lifetimes and CDB

spectra were in between those of $YBa_2Cu_3O_6$ and $YBa_2Cu_3O_7$. The existence of a more or less delocalized state in the basal plane was confirmed for any investigated value of δ. The scattering of the results for various YBCO supercells with a fixed δ but different positions of the oxygen vacant sites was as large as the difference between the results for YBCO supercells with unequal δ. It seems that the used supercells of $3 \times 3 \times 1$ unit cells are too small for a reliable calculation of the δ dependency of PAS observables. For this purpose, larger supercells should be treated with a random distribution of oxygen atoms in the basal planes. Single oxygen vacancies do not trap positrons with high efficiency due to their trapping potential with a shallow depth of around 0.1 eV [149–151]. However, the 2D plot for the basal planes of $YBa_2Cu_3O_{6.33}$ and $YBa_2Cu_3O_{6.78}$ in figure 6.5 reveals that $|\Psi_+(\mathbf{r})|^2$ is clearly enhanced at such vacancies. A random agglomeration of unoccupied oxygen sites will effectively deform $|\Psi_+(\mathbf{r})|^2$ and reduce the positron mobility. In the present study, which only involves experiments at or even above room temperature, $|\Psi_+(\mathbf{r})|^2$ can be expected to be further smeared than in the plots of figure 6.5.

The observed planar delocalization has to lead to a very small positron mobility along the *c*-axis compared to the perpendicular directions. In contrast to $YBa_2Cu_3O_6$, where a quite isotropic mobility in the basal plane is expected, in $YBa_2Cu_3O_7$ the mobility along the *a*-axis is likely to be lower than along *b*. These anisotropies of the positron mobility clearly show that the classical picture of positron diffusion in metals as a 3D random walk, like illustrated in [21], is not valid in YBCO. This is of great importance for interpreting depth dependent PAS in the YBCO system, since the positron diffusion length L_+ cannot serve as observable for defect concentrations as in metals or semiconductors. Only measurements with the positrons implanted along the *c*-axis were evaluated. Thus, even in the case of absolutely defect free single-crystalline specimens, L_+ can be expected to be in the range of the lattice constant *c*. Hence, it is extremely short compared to the typical value of 100 nm in defect free metals.

State	**$YBa_2Cu_3O_6$**	**$YBa_2Cu_3O_7$**
ideal lattice	230 ps	183 ps
V_{Ba}	337 ps	317 ps
$V_{Cu(1)}$	277 ps	230 ps
$V_{Cu(2)}$	230 ps	205 ps
V_Y	253 ps	260 ps

Table 6.1: Calculated positron lifetimes in $YBa_2Cu_3O_6$ and $YBa_2Cu_3O_7$ for an ideal, defect free lattice and for saturation trapping of positrons in one species of metallic vacancies V_{Ba}, V_{Cu} or V_Y. See figure 6.4 for the position of Cu(1) and Cu(2).

Impact of Metallic Vacancies

Finally, the positron annihilation in $YBa_2Cu_3O_6$ and $YBa_2Cu_3O_7$ was considered under the presence of metallic vacancies V_{Ba}, V_{Cu} and V_Y. These were modeled in the previously described supercells by removing single atoms of the respective elements from sites in the center of the supercell. Two different vacancy types $V_{Cu(1)}$ and $V_{Cu(2)}$ were considered for Cu. Their two sites are marked in figure 6.4: $V_{Cu(1)}$ is a vacancy in the basal plane with its Cu(O) chains and $V_{Cu(2)}$ in the CuO_2 plane. The obtained CDB spectra will be discussed later in section 6.4.2, the positron lifetimes are given in table 6.1. In most cases, the lifetime for a positron trapped in a vacancy is longer than in the defect free lattice. Exemplarily, a localized positron state with an increased lifetime, caused by trapping in $V_{Cu(2)}$, is shown for $YBa_2Cu_3O_7$ in figure 6.6.

It is particularly noteworthy that for $V_{Cu(2)}$ in $YBa_2Cu_3O_6$ the same lifetime as in the defect free configuration was found. Visualizing $|\Psi_+(\mathbf{r})|^2$ in figure 6.6 reveals that this vacancy does not trap positrons. In contrast to this, $|\Psi_+(\mathbf{r})|^2$ localizes at $V_{Cu(2)}$ in $YBa_2Cu_3O_7$. Hence, a clear difference between the according positron lifetimes in $YBa_2Cu_3O_6$ and $YBa_2Cu_3O_7$ was obtained. This surprising phenomenon is explained by the larger attractive open volume in the completely oxygen deficient basal plane in $YBa_2Cu_3O_6$. In $YBa_2Cu_3O_7$, this open volume is smaller and hence, the more attractive $V_{Cu(2)}$ traps the positron. Concurrent with this explanation, Nieminen found in his calculations that the affinity of the basal plane is maximal for $YBa_2Cu_3O_6$ [150]. Moreover, in $YBa_2Cu_3O_7$, the binding energy of $V_{Cu(2)}$ is only around 0.6 eV [149, 151]. Thus, $V_{Cu(2)}$

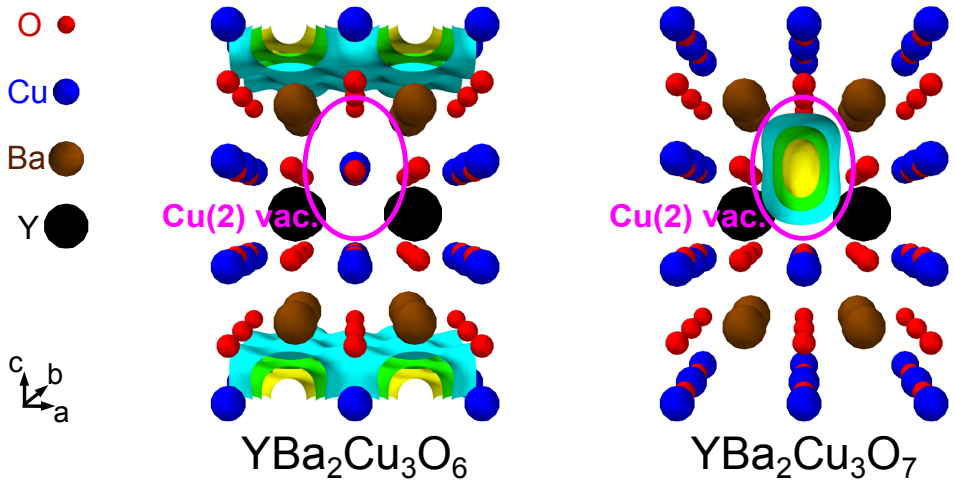

Figure 6.6: Calculated 3D isosurfaces of the positron probability density at a single vacancy $V_{Cu(2)}$ in $YBa_2Cu_3O_6$ and $YBa_2Cu_3O_7$ (linear scale of the contours). The completely oxygen deficient basal plane of $YBa_2Cu_3O_6$ is even more attractive to a positron than $V_{Cu(2)}$. Contrariwise, in $YBa_2Cu_3O_7$, the positron is trapped in $V_{Cu(2)}$.

is the most shallow positron trap formed by metallic vacancies in YBCO.

Similar to the case of defect free YBCO, the obtained positron lifetimes for $YBa_2Cu_3O_7$ show good qualitative agreement to previously published results [149, 150]. Positrons localized in V_{Ba} or $V_{Cu(1)}$ show a longer lifetime for $\delta = 1$ than for $\delta = 0$ and hence, an increasing oxygen content in the basal plane leads to a higher positron annihilation rate. The effects are quite large and, due to this, even positrons trapped in these vacancies probe the oxygen deficiency. Only when positrons are trapped in V_Y with largest distance from the basal plane, their lifetimes for $YBa_2Cu_3O_6$ and $YBa_2Cu_3O_7$ hardly differ. In this case, PAS is not sensitive to changes of the oxygen deficiency δ anymore.

6.3 Investigated Thin Monocrystalline YBCO Films

Preparation with Pulsed Laser Deposition (PLD)

The investigated thin YBCO film samples were produced and characterized in the group of German Hammerl at the Universität Augsburg. In order to grow monocrystalline YBCO films, PLD on a $SrTiO_3$ (STO) substrate was applied. In PLD [126, 127], thin films are physically vapor deposited in order to achieve both epitaxial and stoichiometric growth. For this purpose, a high-power pulsed laser beam is focused onto the surface of a target inside a vacuum chamber. Thus, the target material is vaporized from the surface region forming a plasma plume and then deposited on the substrate. An important requirement for the reproducible production of high-purity and -quality thin film systems is the adjustment of various process parameters, such as the choice of a proper substrate material and temperature, an adequate ambient pressure and a suitable repetition frequency of the laser pulse. For the deposition of the investigated films, a KrF laser with a laser fluence of $2\,J/cm^2$ and a frequency of 5 Hz was used. Prior to the deposition process, commercially available $10 \times 10\,mm^2$ STO wafers were cut into four pieces and routinely cleaned. During deposition, which took place under identical conditions for all samples, the approximately $5 \times 5\,mm^2$ STO substrates were heated up to around 760 °C at an ambient oxygen pressure of 0.25 mbar. After deposition, the films were annealed at 400 °C in a 400 mbar O_2 atmosphere. Typical temperature sequences for the described procedure are given in [127, 159]. Subsequently, the films were individually heat treated in order to alter their oxygen deficiency; details of this process are described below.

Characterization by Complementary Techniques

After the deposition and the individual heat treatment, several experimental techniques were applied for a routine check of the quality and properties of the thin YBCO film samples. Electric transport measurements were used to prove the superconductivity in the films and to determine of the critical temperature T_c. These results already allow a rough

estimation of the oxygen deficiency δ. Moreover, the single-crystallinity of the produced films was confirmed by X-Ray Diffraction (XRD). Additionally, the oxygen deficiency δ of the films was precisely determined by evaluating the lattice parameter c in Θ-2Θ XRD-scans, using a linear equation determined by Benzi et al. [160]. Electron microscopy was applied for the determination of the film thickness for some of the samples, which was found to be $210 \pm 10\,\mathrm{nm}$.

Overview of Investigated Specimens

In the positron measurements, two sets A and B of YBCO specimens were studied. An overview of the investigated samples and their characteristics is given in table 6.2. For both sets, one sample was left in the as-deposited state; these are A1 and B1 respectively with $\delta \approx 0.2$. In order to increase δ, the other films were treated at an elevated temperature of $T \approx 400\,^{\circ}\mathrm{C}$ under different conditions after their growth. For each sample, the residual pressure p_{temp} during the heat cycle or its duration t_{temp} were varied. The time dependent evolution of T is described by a monotonous increase to the maximal $T = 400\,^{\circ}\mathrm{C}$, which is held for only a few minutes, and a subsequent monotonous cooling down; t_{temp} denotes the total cycle time including the phases of heating and cooling. Obviously, more oxygen is removed when the samples are tempered for a longer time in UHV. This procedure allows one to increase the oxygen deficiency δ in a wide range and thus, to decrease T_{c} or even extinct HTSC as it is the case of sample B3.

Sample	$\boldsymbol{\delta}$	$\boldsymbol{T_{\mathrm{c}}}$ **(K)**	$\boldsymbol{t_{\mathrm{temp}}}$ **(min)**	$\boldsymbol{p_{\mathrm{temp}}}$ **(mbar)**
A1	0.19	90	n.a.	n.a.
A2	0.48	60	30	$2{\cdot}10^{-2}$
A3	0.64	60	30	10^{-7}
A4	0.79	25	50	10^{-7}
B1	0.21	90	n.a.	n.a.
B2	0.70	60	10	10^{-7}
B3	1.03	n.a.	20	10^{-7}

Table 6.2: Investigated $YBa_2Cu_3O_{7-\delta}$ films: The samples were grown and characterized at Universität Augsburg. δ was determined by XRD and T_{c} from electrical resistivity measurements. The samples were individually heat treated with different tempering times t_{temp} and residual pressures p_{temp}.

6.4 Characterization of YBCO Films by (C)DBS

In a first experiment, the samples were investigated by depth dependent DBS. Characteristic lineshape parameters of the YBCO films were determined from these measurements. Additionally, optimal values for the positron implantation energy E_+ could be chosen for accompanying CDBS and later experiments. The CDBS results were interpreted by use of the theoretical spectra obtained from the calculations presented in section 6.2.

6.4.1 DBS Depth Profiling

The $S(E_+)$ depth profiles as function of the incident positron energy E_+ are shown in figure 6.7. All curves exhibit a steep decrease for $E_+ < 3\,\mathrm{keV}$, which is caused by annihilation at the surface. In the range of $3 \leq E_+ \leq 7\,\mathrm{keV}$, the $S(E_+)$ curves of the various samples show different behaviors. For $E_+ > 7\,\mathrm{keV}$, the S-parameters decrease with increasing E_+

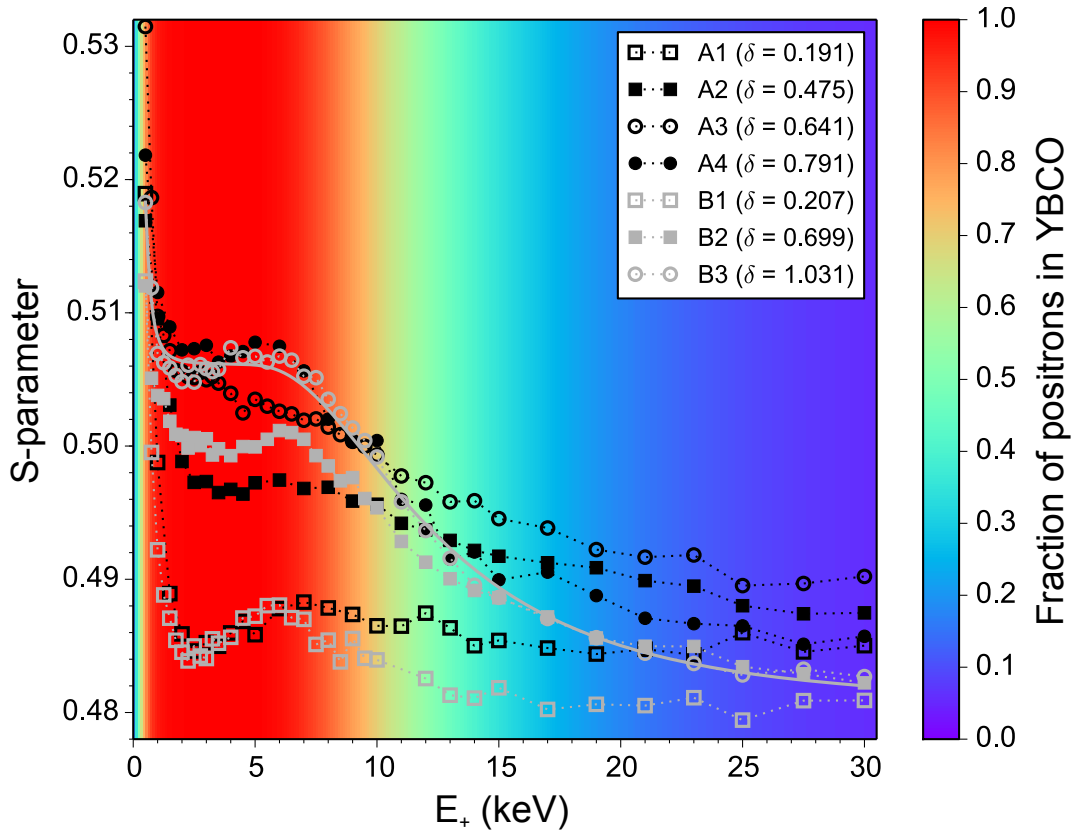

Figure 6.7: The S-parameter as function of the incident positron energy E_+ in thin $YBa_2Cu_3O_{7-\delta}$ films: The incident energy dependent fraction of positrons annihilating in the $YBa_2Cu_3O_{7-\delta}$ films is displayed by the color scale, which was obtained by a fit of the data of sample B 3 (gray solid line).

and the $S(E_+)$ curves of the various samples converge. At $E_+ = 30\,\mathrm{keV}$ the S-parameters of the sample of set B lie very closely together, whereas for set A small but significant differences are found. At such high incident energies nearly all positrons annihilate in the STO substrate. Hence, these differences do not play a role for the analysis of the YBCO films, nevertheless they will be treated in more detail within section 6.5.

The $S(E_+)$ depth profiles were analyzed by use of the VEPFIT software [73] for least square fits of the data. Its application for depth dependent DBS on thin (metallic) films is described in detail in [70]. Within the fit model, the implantation of positrons into this material was described by Makhovian implantation profiles (see section 2.4 for details) with $A = 3.76 \frac{\mu\mathrm{g}}{\mathrm{cm}^2}\mathrm{keV}^{-n}$, $m = 1.853$ and $n = 1.64$. In the simplest possible approach, the two-layer system of the 210 nm YBCO film on the STO substrate was modeled. The respective S-parameters and positron diffusion lengths L_+ of both layers were treated as free parameters. Additionally, the S-parameter at the surface S_{surf} was fitted. Exemplarily, the fit obtained for sample B 3, which yielded the solid line in figure 6.7, is shortly discussed in the following. According to this fit, the plateau in the $S(E_+)$ between and 1.7 and 7 keV is caused by the annihilation of all positrons in the thin YBCO film with a characteristic S-parameter $S_{\mathrm{YBCO}} = 0.5061(1)$. Positrons in the STO substrate annihilate with an characteristic S-parameter $S_{\mathrm{STO}} = 0.4805(1)$.[1] As mentioned above, positron back diffusion is only observed for relatively small implantation energies $E_+ < 3\,\mathrm{keV}$, where other surface effects, like the annihilation of non-thermalized positrons, cannot be neglected. Hence, a reliable separation of real back diffusion and surface effects, as demonstrated in [70], is not possible but not relevant for this study as further explained at the end of the next paragraph. The positron diffusion length $L_{+\mathrm{YBCO}}$ was found to be 0.7 nm, which is extremely low. Due to the described uncertainties, this value is an upper limit for $L_{+\mathrm{YBCO}}$. An important fit result is the fraction of positrons annihilating in the YBCO film, which is displayed in the color map of figure 6.7. It is mainly given by the implantation profile, which is additionally broadened due to the positron diffusion. This fraction as function of the incident energy will be used in the following data treatment.

The described fit model was also used for the analysis of the $S(E_+)$ curves of the other samples. Thus obtained fits showed quite good agreement for the tempered YBCO films, but could not satisfactorily describe the $S(E_+)$ depth profiles in non-tempered YBCO films. The reason for that is obvious as can be seen for samples A1 and B1 in figure 6.7: S varies with E_+ within the YBCO film and takes a minimum at around $E_+ = 3.5$ keV and a maximum at around $E_+ = 6.5\,\mathrm{keV}$. Similar behavior, but less distinct, is also exhibited by the $S(E_+)$ depth profiles of samples A2, B2 and B3. The behavior in sample A3 with a continuous decrease of S for increasing E_+ is also remarkable. These features are attributed to interface effects or inhomogeneities in depth, which will be investigated in

[1] Errors are uncertainties of the fit as given by VEPFIT.

the following sections 6.4.2 and 6.6. Nevertheless, values for the positron diffusion length $L_{+\mathrm{YBCO}}$ were determined for all samples by use of the presented fit model. In all films, $L_{+\mathrm{YBCO}}$ was found to be smaller than 5 nm in the evaluated c-direction. Possibly, these values are too high due to the influence of surface effects or a S that is not constant in depth. As discussed in section 6.2, values not larger than a few nm are even expected in defect free YBCO films due to the localization of the positron in the basal plane. Hence, $L_{+\mathrm{YBCO}}$ is not a suitable measure for the film quality and thus, the lineshape parameters and CDB spectra will be investigated in the following.

Characteristic DBS Lineshape Parameters

In order to determine characteristic lineshape parameters S_{YBCO} and W_{YBCO} from depth dependent DBS, the fraction of positrons annihilating in the YBCO film as shown in figure 6.7 was used. According to this, for incident energies $1.25 \leq E_+ \leq 6.25\,\mathrm{keV}$ more than 98 % of the positrons annihilate in the YBCO film. S_{YBCO} and W_{YBCO} were obtained by averaging the respective values from depth dependent DBS in this energy range. For the present system, the W-parameter was obtained from Doppler shifts $1.77 \leq \Delta E \leq 3.54\,\mathrm{keV}$.

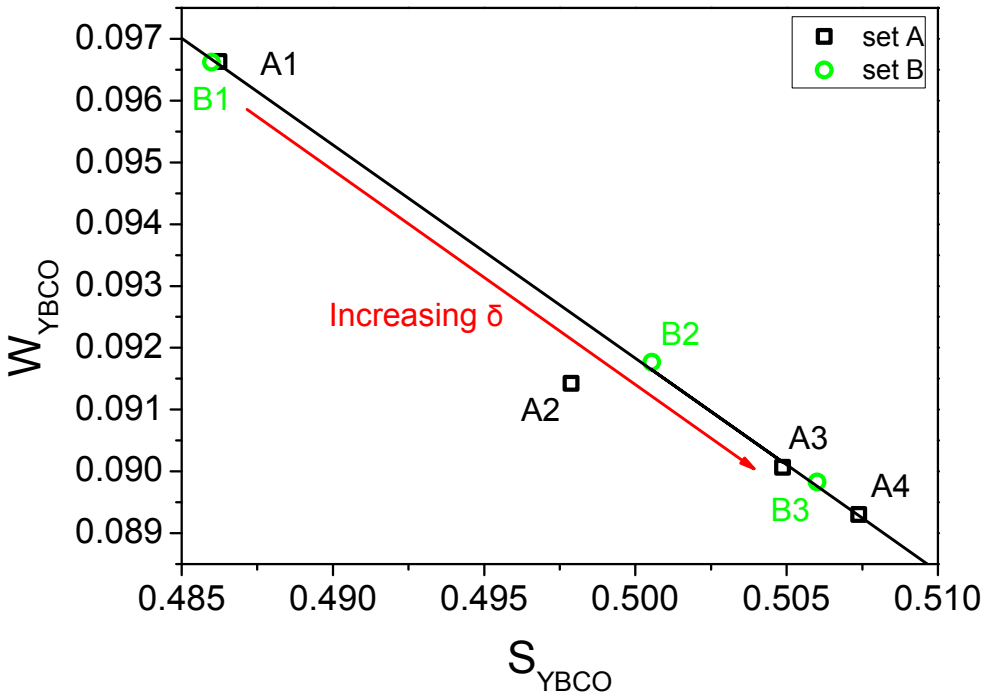

Figure 6.8: S-W-plot for $YBa_2Cu_3O_{7-\delta}$ films: S_{YBCO} and W_{YBCO} were obtained by averaging of depth dependent DBS results (figure 6.7) for $1.25 \leq E_+ \leq 6.25\,\mathrm{keV}$. The solid line is result of a linear fit. Statistical errors of the data points are $\Delta S = 1.5 \cdot 10^{-4}$ and $\Delta W = 8.5 \cdot 10^{-5}$.

As always, the range $\Delta E < 0.84\,\mathrm{keV}$ was considered for the S-parameter. The resulting S-W-plot is shown in figure 6.8.

A very clear effect of the varying oxygen deficiency δ in the investigated specimens is seen: With increasing δ, W_{YBCO} reduces and S_{YBCO} increases. Nearly all data points lie on a line and are well described by a linear fit yielding the solid line in figure 6.8. The found linear dependency of S_{YBCO} and W_{YBCO} strongly indicates that positrons are mainly sensitive to one effect which is the variation of the oxygen deficiency δ in the investigated specimens.

The fit did not account for sample A2, which is not described by the straight line, since it exhibits a relatively low W_{YBCO} and is not lying on a line with the other data points. In the subsequent CDBS measurements, A2 did not show such an extraordinary behavior in the respective range of ΔE. Hence, the observed discrepancy seems just to be an outlier. This interpretation was supported by evaluating the relative lineshape parameters to the bulk, i. e. dividing S_{YBCO} and W_{YBCO} by the S- and W-parameters detected at maximal implantation energies $E_+ \geq 25\,\mathrm{keV}$. The obtained relative lineshape parameters lie on a line, which clearly shows that the observed discrepancy for A2 is caused by external influence on the measurement signal, e. g., a short-term variation of the electronic noise at the CDB-spectrometer in the experimental hall of the FRM II.

6.4.2 CDBS Results

CDB spectra were taken in set A at $E_+ = 4\,\mathrm{keV}$ for investigating the found impact of the oxygen deficiency on DBS results in more detail. As it can be seen from depth dependent DBS, at this incident energy a depth region is probed where surface or interface effects only play a negligible role. The sample A4 with a maximum δ was used as a reference for obtaining the CDB ratio curves shown in figure 6.9. The same experiment was performed for the specimens of set B, which yielded the ratio curves in figure 6.10(a) where the spectrum of sample B3 was used as CDB reference. In this set, CDBS was also conducted at $E_+ = 7\,\mathrm{keV}$, where most of the positrons annihilate at the interface region between YBCO film and STO substrate, which resulted in the ratio curves shown in figure 6.10(b).

For all probed samples and incident energies, the ratio curves of oxygen-rich samples exhibit significant and systematic features. With increasing oxygen content, the signatures of the spectra approach the calculated ratio curve of $YBa_2Cu_3O_7$ with respect to $YBa_2Cu_3O_6$. The following features indicate a high oxygen content: (i) Weakening for Doppler shifts $\Delta E < 1\,\mathrm{keV}$, (ii) a pronounced peak in the range $1 < \Delta E < 4\,\mathrm{keV}$ and (iii) an enhancement for $\Delta E > 5\,\mathrm{keV}$ due to a higher probability for annihilation with core electrons. The detected features (i) and (ii) reflect in more detail the behavior of S_{YBCO} and W_{YBCO} shown in figure 6.8. Absolutely, the CDB ratio only varies between 0.93 and 1.30 and hence, the observed effect is relatively small compared e. g. to the differences between

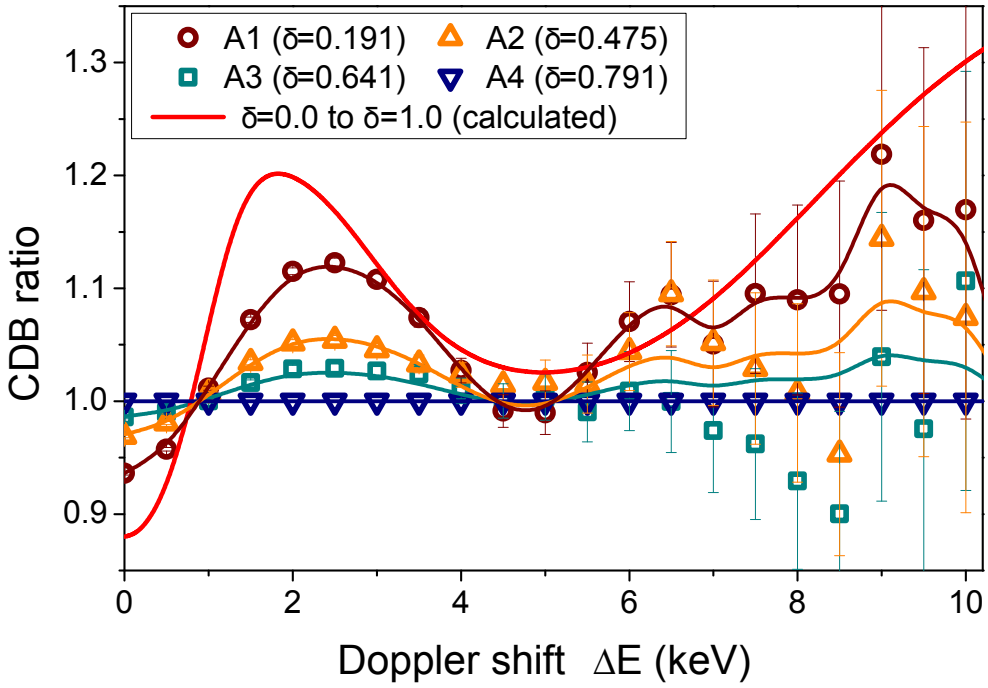

Figure 6.9: CDB ratio curves of set A at $E_+ = 4\,\mathrm{keV}$ with A4 as reference. The thin solid lines were obtained by a linear superposition of the curves of A1 and A4. The calculated ratio curve (red line) is that of $YBa_2Cu_3O_7$ with $YBa_2Cu_3O_6$ as reference.

CDB spectra of various elements as shown in figure 3.2. It is noteworthy that $E_+ = 7\,\mathrm{keV}$, i. e. at the interface, a very similar dependency as in the films is observed. This confirms that positrons probe the oxygen deficiency throughout the complete depth of the films even at the interface, where vacancies possibly are present with a higher concentration as discussed at the end of this section.

In order to quantitatively analyze the observed changes in the CDB ratio curves, the detected ratio curves $I(\Delta E)$ were fitted by a linear superposition of two reference spectra. In case of set A, these were the ratio curves of A1 with the minimal and of A4 with maximal δ. Hence, the weighting factor x_{CDB} as defined by

$$I(\Delta E) = (1 - x_{\mathrm{CDB}}) \cdot I_{A1}(\Delta E) + x_{\mathrm{CDB}} \cdot I_{A4}(\Delta E) \tag{6.2}$$

was fitted. This analysis was analogically done for the ratio curves of set B in separate fits for $E_+ = 4\,\mathrm{keV}$ and $E_+ = 7\,\mathrm{keV}$. In figures 6.9 and 6.10, the solid lines represent the fitted ratio curves. They well agree with the detected ratio curves for all measurements, especially for Doppler shifts $\Delta E \leq 7\,\mathrm{keV}$. Even at higher Doppler shifts, the fitted ratio curves describe the measured ones in the most cases despite the relatively large statistical error of the data and the quite small differences between the spectra. The CDB ratio curve

of specimen A2, which showed a slightly deviant value of $(S_{\mathrm{YBCO}}, W_{\mathrm{YBCO}})$ in figure 6.8, is also well described by this linear superposition. Thus, it is concluded that it behaves in accordance to the other specimens. Hence, CDBS confirmed that positrons in the

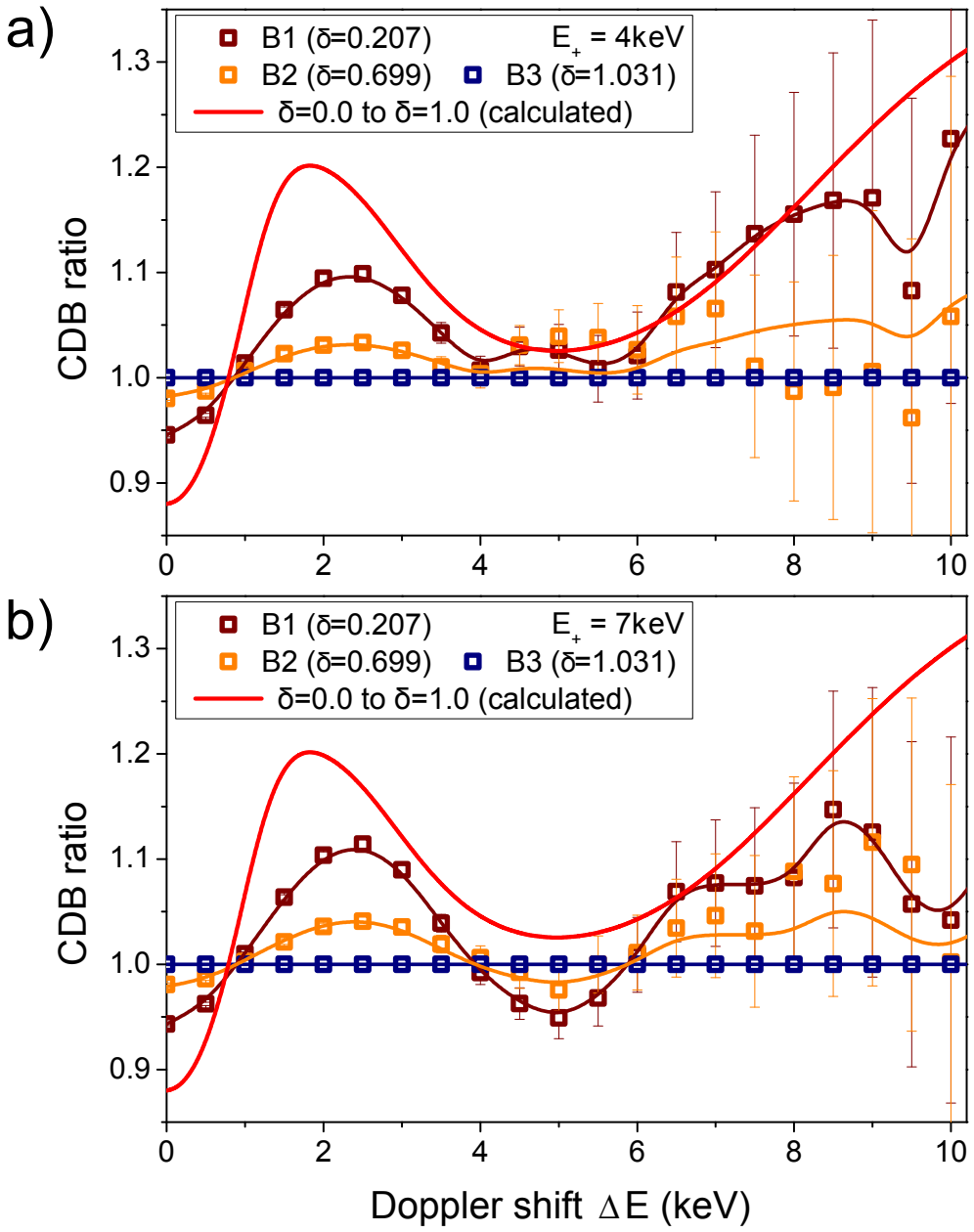

Figure 6.10: CDB ratio curves of set B at (a) $E_+ = 4\,\mathrm{keV}$ and (b) $7\,\mathrm{keV}$ with B3 as reference. The thin solid lines were obtained by a linear superposition of the curves of B1 and B3. The calculated ratio curve (red line) is that of $YBa_2Cu_3O_7$ with $YBa_2Cu_3O_6$ as reference.

YBCO films – even at the interface to the substrate – are sensitive on the varying oxygen deficiency δ. Other differences between the samples, if present at all, only slightly affect PAS results.

Interpretation of CDB Results – Oxygen Deficiency and Role of Metallic Vacancies

For a deeper understanding of the found sensitivity, the measured CDB ratio curves of A1 and B1 with the minimal oxygen deficiency δ are compared with the theoretical ratio curves of $YBa_2Cu_3O_7$ to the reference $YBa_2Cu_3O_6$ in figure 6.11. Their calculation is described in section 6.2. As mentioned, the calculations accounted for annihilation in defect free YBCO and positrons trapped in metallic vacancies V_{Ba}, $V_{Cu(1)}$, $V_{Cu(2)}$ and V_Y. The theoretical ratio curves determined for the defect free state, V_{Ba} and $V_{Cu(1)}$ exhibit very similar signatures as the experimental ones. They show the same features described above, i. e. (i) weakening for low ΔE, (ii) pronounced peak at around $\Delta E = 2\,\mathrm{keV}$ and (iii) higher core annihilation probability for $\Delta E > 5\,\mathrm{keV}$. Compared to these theoretical curves,

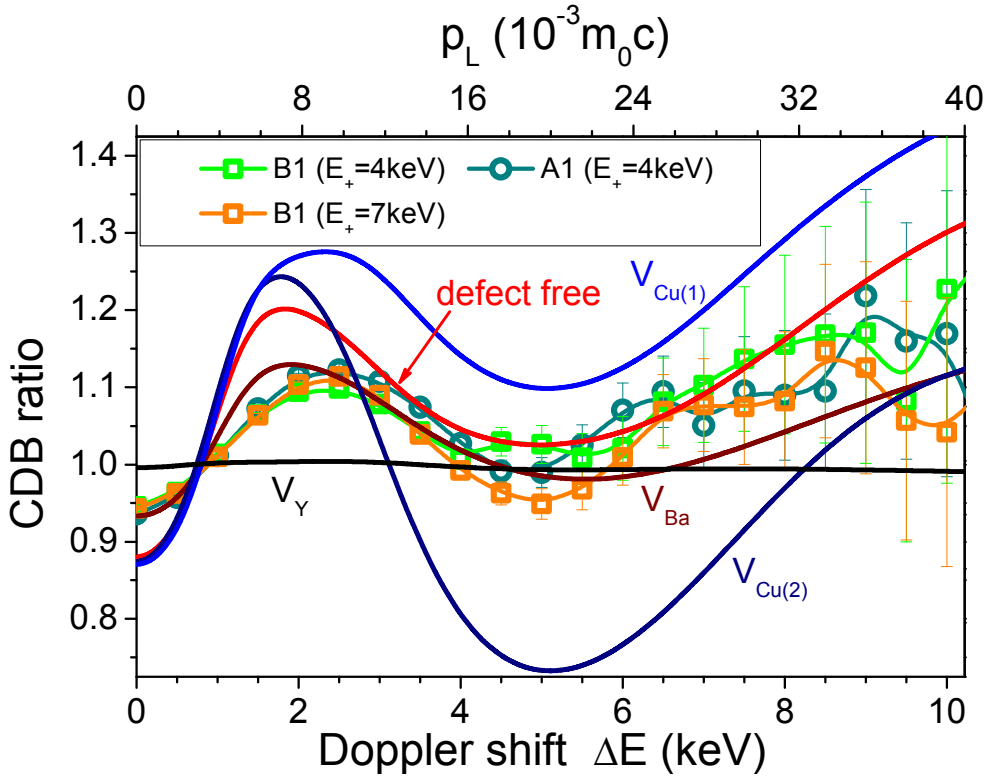

Figure 6.11: Calculated ratio curves of $YBa_2Cu_3O_7$ with $YBa_2Cu_3O_6$ as reference and measured ratio curves from figures 6.9 and 6.10. Annihilation in defect free YBCO and in metallic vacancies potentially present was considered in the calculations as described in section 6.2.

the ratio curve calculated for $V_{Cu(2)}$ shows a similar behavior but a strongly pronounced minimum at $\Delta E = 5\,\mathrm{keV}$ taking values below 0.8. This difference is attributed to the surprising behavior of the positron if this kind of vacancy is present. As illustrated in figure 6.6, $V_{Cu(2)}$ only acts as trapping center in $YBa_2Cu_3O_7$. In agreement with the calculated lifetimes given in table 6.1, the CDB signature for V_Y does not show any significant deviations from unity and hence, in this state positrons are not sensitive to the oxygen deficiency.

The comparison with the calculated CDB spectra reveals that the CDB signature observed in the experiments is clearly caused by the different oxygen deficiency δ of the films. The results allow to exclude the presence of a high amount of V_Y, since trapping of positrons in these would lead to an extinction of the sensitivity on δ. Possibly, such vacancies might exist in set B, because the ratio curve of sample B1 with reference B3 exhibits a slightly less pronounced signature as that of A1 with reference A4. Since the difference in δ is larger between B1 and B3 (see table 6.2), a higher fraction of positrons that annihilates in V_Y in set B could well explain this finding. The ratio curve calculated for V_{Ba} describes the measured ones best, which, however, does not allow to conclude that positron annihilation only takes place there. Also a contribution of various positron states such as annihilation in defect free bulk and V_{Ba}, $V_{Cu(1)}$, $V_{Cu(2)}$ or V_Y, which leads to a superposition of their respective ratio curves, can explain the experimental signatures. Moreover, the differences between these are quite small and their signatures could also be influenced by the applied simple calculational scheme.

Interface Effects

As mentioned in the discussion of depth dependent DBS, some samples showed a behavior which is attributed to inhomogeneity of the YBCO films with depth. Most likely, these features are caused by interface effects. Especially the small lattice mismatch $< 2\,\%$ between STO substrate and YBCO films could lead to a higher concentration of vacancies close to the interface. An adapted evaluation of the already presented CDB spectra of set B enables to extract further information about vacancies in this region. For this purpose, for each sample, the ratio curves of the CDB spectra measured at $E_+ = 7\,\mathrm{keV}$ to those of $E_+ = 4\,\mathrm{keV}$ are shown in figure 6.12. Obviously, depth dependent effects are quite small and a systematic behavior exhibited by all samples is not found. A CDB ratio with values < 1 for Doppler shifts in the range of $3 < \Delta E < 7\,\mathrm{keV}$ reflects a significant change of the signature. However, it is not possible to attribute this feature to a certain kind of vacancy by comparison with the calculated spectra. Hence, it must be caused by the superposition of various defect types. The composition is expected to differ for the various samples, since the observed feature is not identical in the measured ratio curves. As it was shown by the CDBS analysis of set B in section 6.4.2, also when implanted close to the interface,

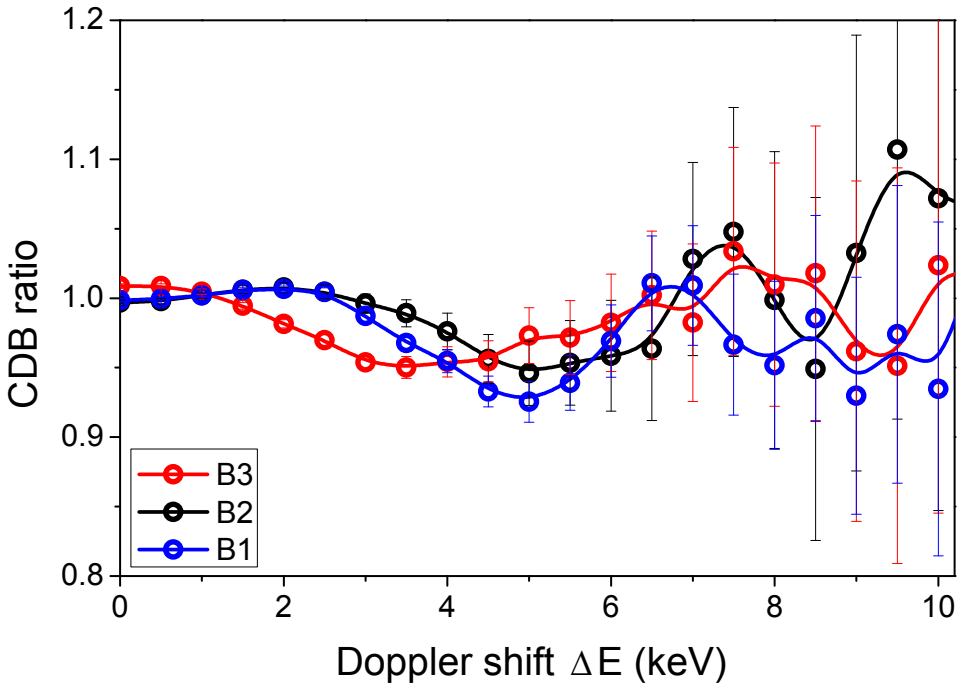

Figure 6.12: CDB ratio curves measured in various YBCO films at $E_+ = 7\,\mathrm{keV}$, i.e. at the interface region. The spectra measured at $E_+ = 4\,\mathrm{keV}$ in the respective samples were used as references. The CDB signatures only show slight deviations from unity, so potentially present vacancies at the interface cannot be identified. The solid lines are guides to the eye.

positrons are mainly sensitive to the oxygen deficiency and possibly existent defects do not significantly affect this behavior.

6.4.3 Correlation between (C)DBS Results and Oxygen Deficiency

For a characterization of the quantitative dependency of (C)DBS results on the oxygen deficiency δ, the CDBS weighting factor x_{CDB} and S_{YBCO} obtained from DBS are plotted over δ in figure 6.13. In set A, the dependency of the CDB weighting factor x_{CDB} on δ is well described by the linear fit shown in figure 6.13. Also the respective S_{YBCO} derived from conventional DBS with lower peak-to-background ratio exhibits a similar behavior, in particular for $\delta < 0.65$. The respective solid line was obtained by an error-weighted fit. In set B, S_{YBCO} and x_{CDB} also show a monotonous correlation to δ. The dependency of S_{YBCO} is quite linear but weaker in set B, e. g. S_{YBCO} of B2 is clearly lower than that of A3 despite a similar δ. Furthermore, x_{CDB} only roughly exhibits a linear behavior. Here, x_{CDB} was evaluated for both measurements in the film and at the interface shown in figure 6.10. The weaker dependency of S_{YBCO} in set B could be explained by a higher amount of

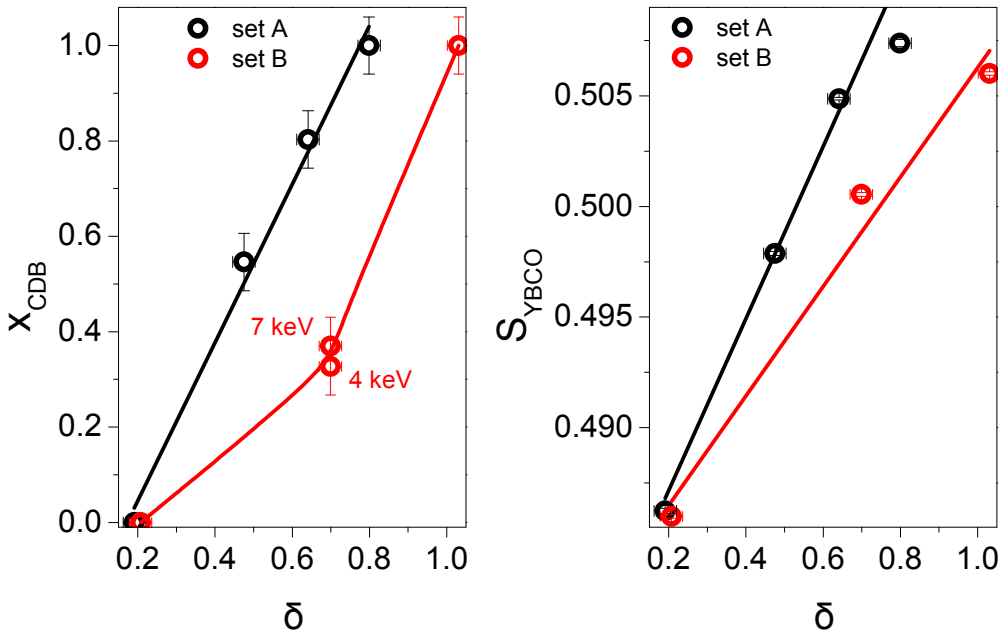

Figure 6.13: CDB weighting factor x_{CDB} and S_{YBCO} in dependence of the oxygen deficiency δ: The solid lines are linear fits to the data, except for x_{CDB} of set B. In set B, the CDBS results show a lower sensitivity to δ, which could be caused by potentially present Y vacancies $\mathrm{V_Y}$.

V_{Y}, where positrons might get trapped prior to their annihilation. This behavior can also explain the relatively low distinctiveness of the CDB signature of B1 and, presumably, leads to the less linear behavior x_{CDB}.

It is concluded that for a set of thin YBCO films, which are grown together and then individually heat treated in order to alter δ, the Doppler broadening of the annihilation line is correlated to the oxygen deficiency δ. A linear fit well describes the results for set A and also explains the results of set B by trend. In literature, a similar linear dependence of the S-parameter was reported for sintered YBCO bulk samples and $\delta < 0.6$ [152]. For an enhanced quantitative evaluation of the dependency, sets with a higher number of specimens with different δ are required. This requires an adaptation in the growth process: YBCO films need to be deposited on a larger area of STO in order to obtain more samples for an individual heat treatment. Thus, more data points for a quantification of the S_{YBCO}-δ or x_{CDB}-δ correlation could be used. Moreover, due to the presented results, it is clear that for each set the correlation between the Doppler broadening of the annihilation line and the oxygen deficiency δ has to be individually determined in order to make use of it in further (C)DBS experiments as they will be presented in the following.

6.5 Analysis of Lateral Homogeneity

In an experiment dedicated to probe the lateral homogeneity of thin YBCO films, the positron beam was scanned over the samples of set A. Here, the high lateral resolution at the NEPOMUC CDB spectrometer as described in section 4.2 was crucial. These measurements were performed in September 2014, which means nearly eleven months after the previously described ones. In the later beam time, a higher beam intensity, caused by a strong improvement of the remoderation efficiency at the NEPOMUC remoderator stage which is described in 4.1, led to a countrate nearly twice as high than before. Under these new experimental conditions, depth dependent DBS was repeated prior to the spatially resolved measurements in order to confirm the previously found results and to obtain a valid S_{YBCO}-δ calibration.

Depth Dependent DBS - Influence of the STO Substrate

The $S(E_+)$ depth profiles obtained by the repetition of depth dependent DBS are shown in figure 6.14. Qualitatively, they show a similar behavior as those discussed in section 6.4 and shown in figure 6.7. However, the detected S-parameters are about 0.01 smaller in the present experiment. This small difference is attributed to the countrate dependent energy resolution of the HPGe detectors. The VEPFIT result used in the further evaluation was obtained by fitting the $S(E_+)$ of sample A3 using the same fit model as in section 6.4. As previously, the fraction of the positrons annihilating in YBCO is displayed by the color code in figure 6.14. From this fraction, the range of the incident energy E_+ considered for the determination of the characteristic lineshape parameter S_{YBCO} was determined to be $3.25 \leq E_+ \leq 6.25\,\mathrm{keV}$. This range corresponds to a minimum fraction of 98 % of the implanted positrons annihilating in the YBCO film. The plot of the thus determined S_{YBCO} over the oxygen deficiency δ exhibits the formerly found linear dependency as can be seen in figure 6.15 . Moreover, another previous observation was confirmed by the repetition of depth dependent DBS as well, namely the difference in S at $E_+ = 30\,\mathrm{keV}$ for the various samples. Approximately 88 % of the positrons with this high incident energy annihilate in the STO substrate with S_{STO} according to the fit results. Hence, a variation of S_{STO} is the reason for these differences and also leads to crossovers of the $S(E_+)$ curves as e. g. for A3 and A4 at $E \approx 8\,\mathrm{keV}$. As before, the as-deposited sample A1 shows the minimal S_{STO} and A3 the maximal S_{STO}. In both measurements, S_{STO} of A2 lies in between these extremal values. In the earlier measurements, S_{STO} of A4 was nearly identical to that of A1, whereas in the later measurements it is very close to that of A2. This systematic behavior indicates a real origin responsible for the differences of S_{STO}.

As described in section 6.3, all films were deposited on STO from the same wafer. Hence, the subsequent individual treatment could cause the varying substrate S-parameters af-

fecting the defect structure of STO in different ways. However, this cannot explain why A1 and A4 have nearly the same S_{STO} in the earlier measurements. Moreover, this explanation fails for the $S(E_+)$ curves of set B in figure 6.7 where all samples showed the same S_{STO}. Thus, a lateral variation of S_{STO} in the substrate could better explain the observed differences for set A. From recent PAS studies it is well known that commercially available STO wafers contain a high amount of vacancies [18, 162]. It appears plausible that their distribution is not homogeneous. STO with precisely defined concentrations of Sr and Ti vacancies can be obtained by using common STO wafers as substrate for the deposition of STO by PLD [163]. Depositing YBCO films on these special STO materials is a promising approach for a further improvement of the film quality. Analyzing various, especially prepared bare STO substrates by CDBS with focus on their quality and homogeneity should be a first step in this process in future experiments.

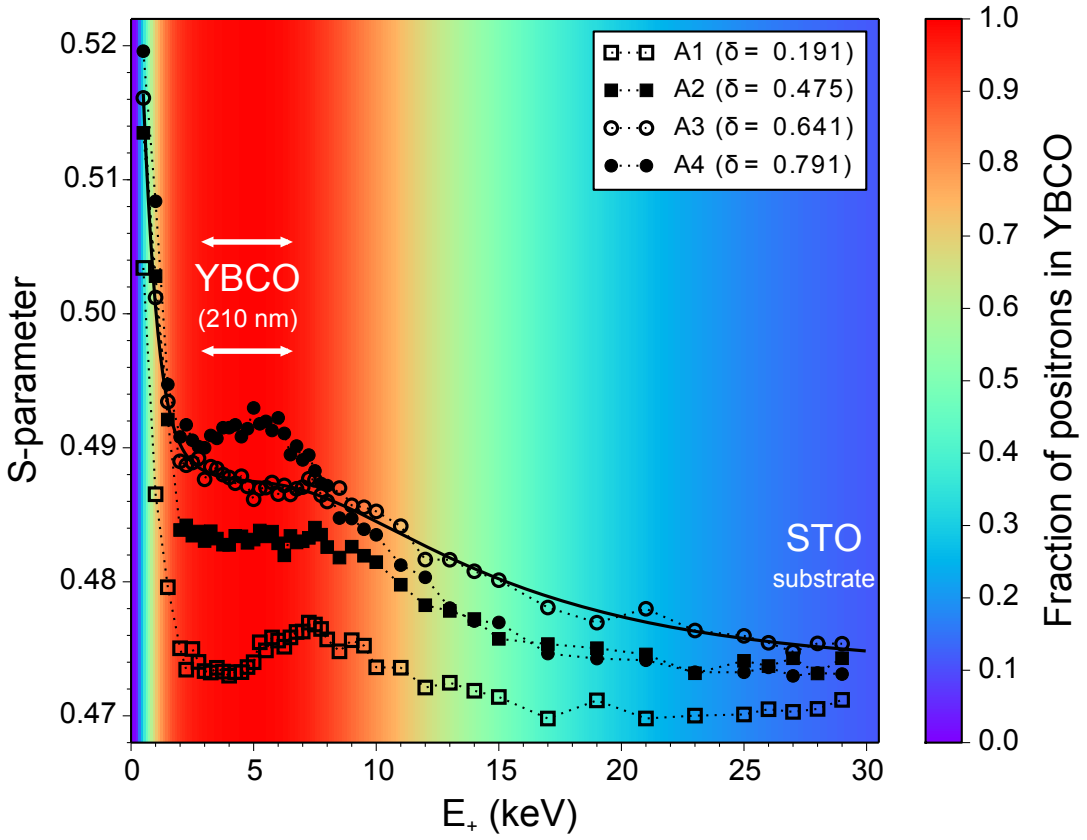

Figure 6.14: The S-parameter as function of the incident positron energy E_+ in thin $YBa_2Cu_3O_{7-\delta}$ films: The incident energy dependent fraction of positrons annihilating in the YBCO films is displayed by the color scale, which was obtained by a fit of the data of sample A 3 (solid line). These measurements were performed eleven months after those shown in figure 6.7 (published in [161]).

Laterally Resolved DBS - Variation in δ

After the relation between S_{YBCO} and δ had been confirmed, laterally resolved DBS was conducted in the four YBCO films of set A at an incident energy E_+=4 keV, where surface and interface effects are negligible. An image of the four samples fixed on the Al sample holder ($S_{\mathrm{Holder}} \approx 0.55$) is obtained by mapping the S-parameter as shown in figure 6.15. In the following, a quantitative analysis of this S-parameter map is presented.

In a first step, for each sample a characteristic S-parameter S_{map} was determined by averaging S over the whole sample area. Similar to S_{YBCO}, its dependency on δ is fairly well described by a linear correlation as shown in figure 6.15. Afterwards, the statistical scattering of S_{map} was investigated by determining its standard deviation σ_{map}. The minimal value was obtained in A1 with $\sigma_{\mathrm{map}} = 0.00128$, whereas in A4 a maximum $\sigma_{\mathrm{map}} = 0.00258$ was detected. This scattering is caused by two contributions, namely

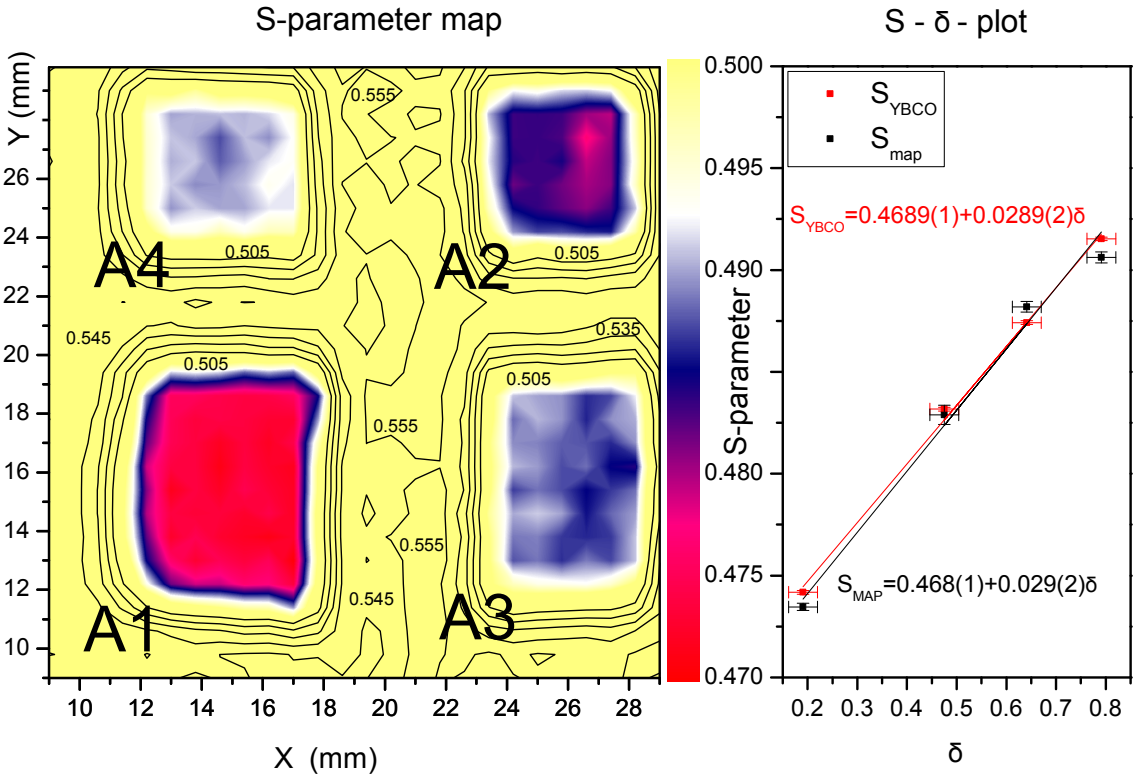

Figure 6.15: Left: 2D S-parameter map of the YBCO samples A1 – A4. The map was obtained by laterally resolved DBS at $E_+ = 4$ keV. *Right:* Correlation between δ determined from XRD and the S-parameters S_{YBCO} and S_{map} averaged from the depth profiles in figure 6.14 and the shown map. The solutions of linear fits are depicted as solid lines (published in [161]).

Sample	δ	σ_δ	T_c (K)
A1	0.191	0.019(1)	90
A2	0.475	0.079(5)	60
A3	0.641	0.048(3)	60
A4	0.791	0.031(2)	25

Table 6.3: Thin $YBa_2Cu_3O_{7-\delta}$ films investigated by spatially resolved DBS (see figure 6.15). The quantity σ_δ for the lateral variation of δ was determined from these measurements by use of equations 6.3 and 6.4.

the statistical error of the measured S-parameter, denoted as σ_{stat}, and the *true* lateral variation σ_{lateral} of S within the probed depth region of the YBCO film. The latter one is of high interest for further analyzing the samples and is given by

$$\sigma_{\text{lateral}} = \sqrt{\sigma_{\text{map}}^2 - \sigma_{\text{stat}}^2} \tag{6.3}$$

with $\sigma_{\text{stat}} = 1.16 \cdot 10^{-3}$, which was determined by repeated measurements of S in a single film at constant E, X and Y.[2] Due to the correlation between oxygen deficiency δ and S, a spatial variation σ_δ of δ leads to the detected lateral variation σ_{lateral} of S. By use of the linear fit result for the S_{map}-δ correlation (figure 6.15), σ_δ was determined by

$$\sigma_\delta = \frac{1}{0.029(2)} \sigma_{\text{lateral}} \tag{6.4}$$

yielding the values given in table 6.3. Here it is assumed that only a lateral variation of δ, with its strong correlation with S, contributes to σ_{lateral}. Possibly, σ_{lateral} could also partially stem from a spatial inhomogeneity in the distribution of potentially present metallic vacancies. However, at least it is expected that the heat treatment performed at relatively low temperatures of 400° C did not alter the concentration or distribution of metallic vacancies. Hence, the following comparison of σ_δ determined by equation 6.4 for the various films should not be affected by these vacancies, because they are assumed to be equally present in all specimens with a similar lateral distribution.

The as-prepared sample A1 showed an intrinsic lateral variation of $\sigma_\delta = 0.019(1)$. Further heat treatment always led to an increase of σ_δ. A maximum $\sigma_\delta = 0.079(5)$, i.e. an increase by a factor of 4.2, was detected in A2. Concurrent with this result, in the according S-parameter map a significant, inhomogeneous variation of S is observed. In figure 6.15, on the right hand side, i.e. at $Y \approx 27\,\text{mm}$, a clearly smaller S-parameter, caused

[2] σ_{stat} is a factor of 1.5 larger than the error given by the number of counts in the spectra due to electronic noise in the experimental hall of the FRM II (see appendix).

by a lower oxygen deficiency δ, is seen than on the left hand side, i.e. at $Y \approx 25\,\mathrm{mm}$. The absolute increase of σ_δ during tempering depends on the residual pressure p_{temp}: A3 was treated in the same way as A2 (see table 6.2) but under a low ambient pressure of $10^{-7}\,\mathrm{mbar}$ instead of an oxygen atmosphere of $10^{-2}\,\mathrm{mbar}$. As a consequence, σ_δ in A3 is only increased by a factor 2.5 compared to the non-tempered specimen A1. The relatively large inhomogeneity observed in A2 is attributed to a more complicated process of oxygen out diffusion in the oxygen atmosphere [164]. The duration of the heat treatment seems to have only a minor impact on σ_δ: In A4, which was tempered in identical conditions as A3 but 20 minutes longer, a slightly smaller value for σ_δ was detected. Possibly, a longer heat treatment leads to a more homogeneous behavior of δ. However, if present at all, this influence on σ_δ is much smaller than the variation of p_{temp}. It is concluded that the quality, in terms of homogeneity of the oxygen deficiency δ, of additionally tempered thin YBCO films can be improved by optimizing the applied process parameters during heat treatment. The results clearly suggest to apply a low ambient pressures p_{temp} for a further quality enhancement of the YBCO films.

6.6 Observation of Out-Diffusion of Oxygen

The high intensity of the NEPOMUC beam was used in order to conduct in-situ DBS at elevated temperatures in two YBCO films. Due to the short measurement times of 1 min for a single DBS spectrum and due to the found correlation between S_{YBCO} and δ, this experiment can reveal unique information about the process of oxygen atoms diffusing out of a YBCO film. In oder to examine the potential of this technique, the samples A1, where $\delta = 0.191$ in the initial state (see table 6.2), and the additionally prepared sample C1 were investigated. This specimen was prepared under extreme conditions to further increase the oxygen content. It showed a relatively high T_{c}=91 K and it is concluded that $\delta < 0.19$ in this sample.

DBS at Elevated Temperatures - Out-Diffusion of Oxygen

Two different temperature cycles as plotted in figure 6.16, were driven and the time dependent evolution of S in the YBCO film ($E_+ = 4\,\mathrm{keV}$) and at the interface ($E_+ = 7\,\mathrm{keV}$) was measured. In the case of sample C1 (figure 6.16(a)), the temperature was increased within 160 s from room temperature to 400 °C, which was then hold for 60 minutes. For sample A1 (figure 6.16(b)), the temperature was increased in small steps within a total time of 177 minutes to 400 °C, which was then hold for only 10 minutes. The residual pressure during these heat treatments was $3 - 5 \cdot 10^{-7}\,\mathrm{mbar}$. For both specimens, for each of the evaluated incident energies, the relative S-parameters to those detected in the as-deposited state are shown in figure 6.16. Complementary XRD measurements were performed after

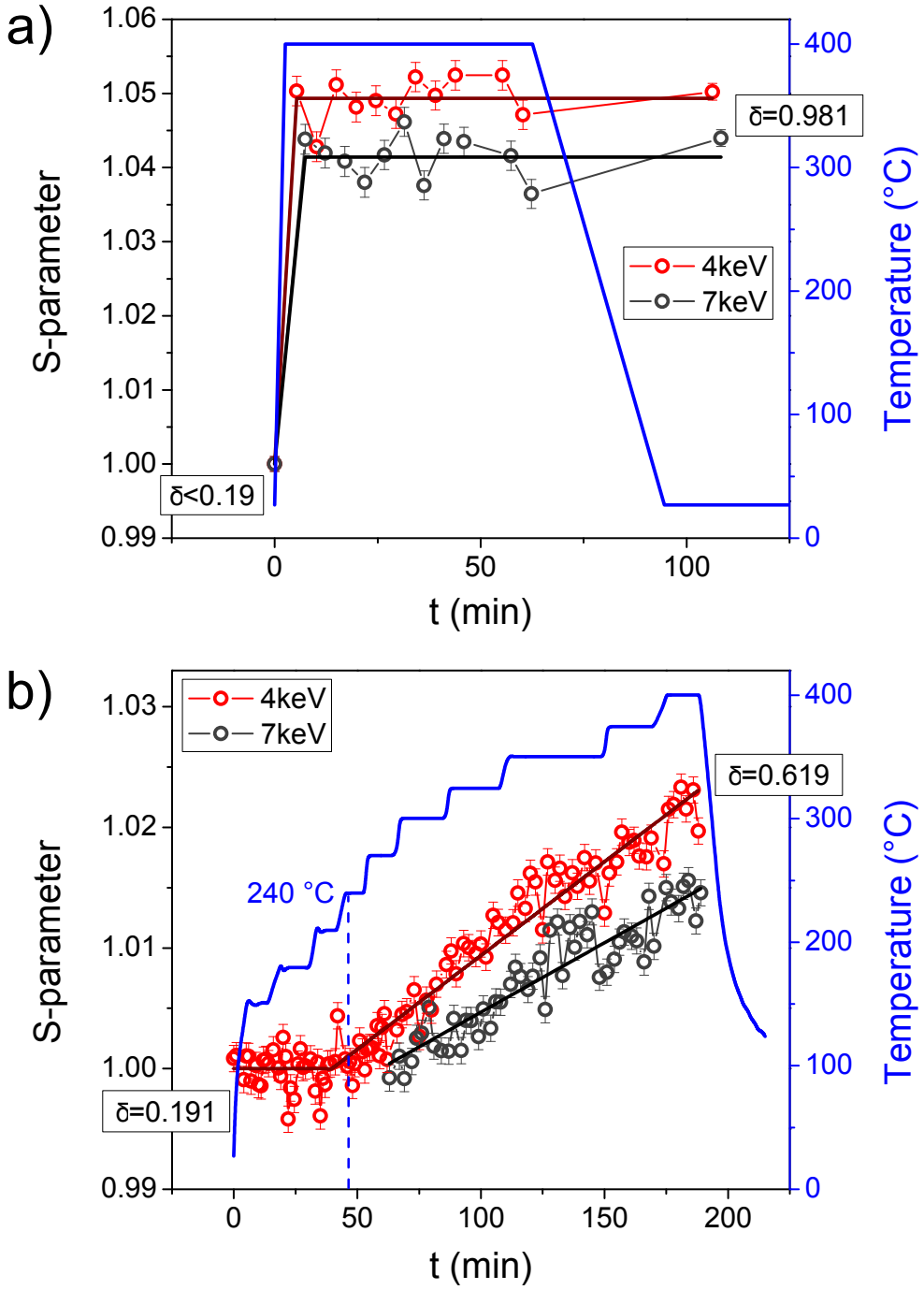

Figure 6.16: In-situ DBS at elevated temperatures in samples (a) C1 and (b) A1 at $E_+ = 4\,\mathrm{keV}$ (film) and $E_+ = 7\,\mathrm{keV}$ (interface): Normalized S-parameters with respect to the as-prepared states and sample temperature as function of time t. The rising of S indicates an increase of δ due to oxygen diffusing out. Guides to the eye are plotted for $S\,(t)$.

tempering at Universität Augsburg and $\delta = 0.619$ in A1 and $\delta = 0.981$ in C1 were measured. As expected, the rise of S above 240 °C correlates with an increase of δ.

The time dependent behavior of S is completely different for both investigated specimens. In sample C1, a massive increase of S took place in the first minutes of the heat cycle at the evaluated implantation energies. After this change in the initial phase of tempering, S did not change any more, even after cooling down. Thus, it is concluded that the specimen was in thermodynamic equilibrium rapidly after $T = 400$ °C has been reached and a non-reversible decrease of the oxygen content took place.

In sample A1, a rise of S (4 keV) began when the temperature exceeded 240 °C, whereas at lower temperatures no changes were observed. For S (7 keV), this threshold temperature is 270 °C. In the subsequent heat treatment with a continuous elevation of temperature in various steps, the S-parameter nearly linearly increased with tempering time as the guides to the eye in figure 6.16(b) illustrate. The linear slope and the absolute maximum of S (7 keV) are smaller than those of S (4 keV), and hence, the reduction of the oxygen

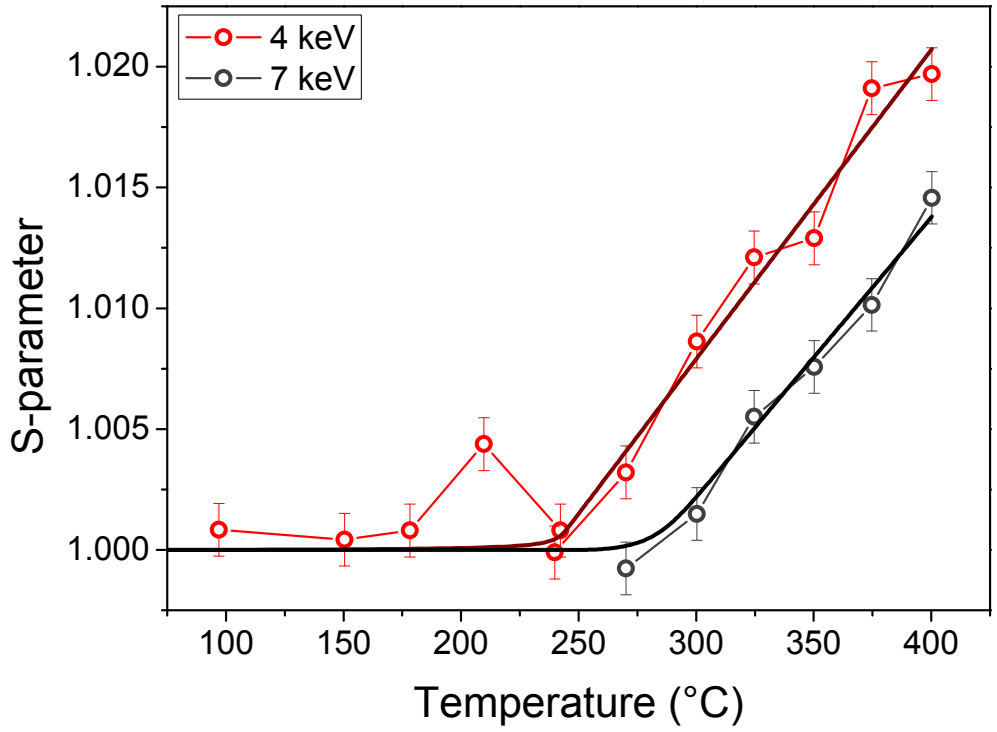

Figure 6.17: S measured at $E_+ = 4$ keV (film) and $E_+ = 7$ keV (interface) as function of temperature in sample A1 as obtained from in-situ DBS at elevated temperature (see figure 6.16). For each temperature step, the last value detected for S is plotted. Solid lines were obtained by a linear fit above the onset temperatures of 240 °C ($E_+ = 4$ keV) and 270 °C ($E_+ = 7$ keV).

content was slower at the interface. In the evolution of $S\,(4\,\mathrm{keV})$ for $T \geq 350\,^{\circ}\mathrm{C}$, a step-like behavior of $S(t)$ reflects the $T(t)$ course. The respective dependence of $S\,(4\,\mathrm{keV})$ and $S\,(7\,\mathrm{keV})$ on the temperature in sample A1 is plotted in figure 6.17. Here, for each temperature step and evaluated incident energy, the lastly detected data point is shown. Above the onset temperatures of 240 °C and 270 °C, respectively, the S-parameters show a linear increase with temperature. The plot reveals that the reduction of the oxygen content was suppressed at the interface. Due to its correlation to S, the oxygen deficiency must be higher in the bulk of the film than at the interface. Hence, the oxygen deficiency δ has to show a depth dependent behavior in the tempered film A1.

Depth Dependent DBS - Inhomogeneities in Tempered Films

In order to corroborate this conclusion, depth dependent DBS was performed on both investigated specimens before and after the heat cycle. The detected $S(E_+)$ curves in figure 6.18 facilitate an interpretation of the observed high-temperature behavior. All

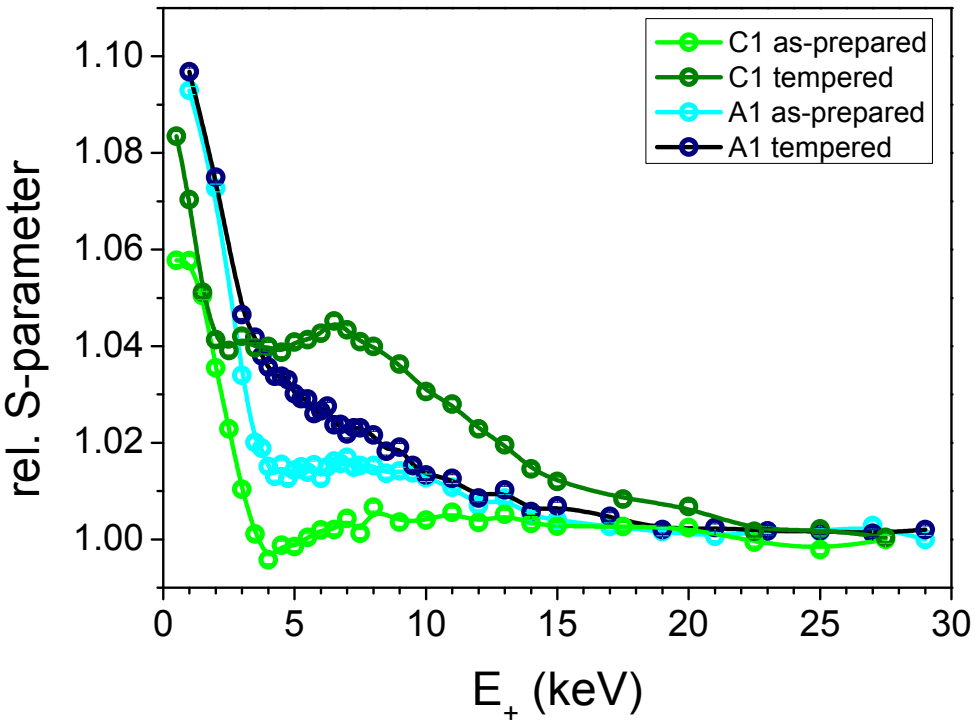

Figure 6.18: S normalized to $S\,(E_+ \geq 25\,keV)$ as function of the incident positron energy E_+ before and after heat treatment (figure 6.16) in the samples A1 and C1: The rising of S between $3 \leq \Delta E \leq 10\,\mathrm{keV}$ is caused by the increase of the oxygen deficiency δ due to the heat treatment. The monotonously decreasing S detected for $3 \leq \Delta E \leq 10\,\mathrm{keV}$ in A1 after the heat cycle is attributed to a non-constant δ.

curves were normalized to their S-parameters detected for $E_+ \geq 25\,keV$ for a better comparability. For both films, as expectable from the previous studies, at these E_+ where positrons mainly probe the substrate, S did not change due to the tempering. In the as-prepared state, C1 exhibits a lower S in the incident energy range $3 < E_+ < 8\,\mathrm{keV}$ than A1, which confirms that $\delta < 0.19$ is smaller in C1. After the heat treatment, a higher S was detected for incident positron energies $3 < E_+ < 8\,\mathrm{keV}$ due to an increased δ in both YBCO films. In this energy range, the tempered specimens A1 and C1 show a completely different behavior in their $S(E_+)$ curves: Similar to the previously investigated YBCO films, C1 exhibits a plateau with a more or less constant S. Inside the film of A1, S, and thus δ, decreases almost linearly with E_+. This depth dependent behavior well agrees with the observations from in-situ DBS described above. Based on all previous results, this strengthens the conclusion that A1 shows a δ, which is clearly inhomogeneous in depth. The oxygen deficiency δ is higher close to the surface than at the interface to the STO substrate.

Depth Dependent CDBS - Oxygen Depth Distribution

As an enhanced technique, depth dependent CDBS was applied to verify the depth dependency of the oxygen deficiency in A1 after the heat treatment. For this purpose, CDB spectra were taken directly in the film with E_+=4 keV and at the interface with E_+ =7 keV before and after tempering. In figure 6.19, the respective ratio curves are shown using the CDB spectra taken at $E_+ = 4\,\mathrm{keV}$ as references. In the as-prepared state, the ratio curve is not significantly deviating from unity and hence, depth dependent features were not detected. This means that the out-diffusion of oxygen took place in a film homogeneous in depth and presumably without any interplay with a defect-rich zone in YBCO close to the interface. After tempering, the ratio curve looks like those of oxygen-rich samples shown in figures 6.10 - 6.11. A very similar curve is obtained when evaluating the CDB ratio of the as-prepared film to the tempered film at E_+=4 keV. Due to the complementary XRD measurements, this CDB signature is unambiguously caused by the lower oxygen content in the tempered film. Thus, CDBS confirmed that the oxygen deficiency δ considerably decreases with depth in A1 after tempering.

Characteristics of Oxygen Diffusion

The in-situ measurements at elevated temperatures clearly reveal that the out-diffusion of oxygen from thin YBCO films is non-trivial: In the firstly investigated sample C1, where a rapid step-like increase to the maximum temperature of 400 °C was applied, the process took place within a few minutes and led to an extremely high $\delta \approx 1$. Thus, at 400 °C, the tempering time apparently is not an appropriate parameter for adjusting the oxygen deficiency in YBCO films. In sample A1, oxygen diffusion was observed above

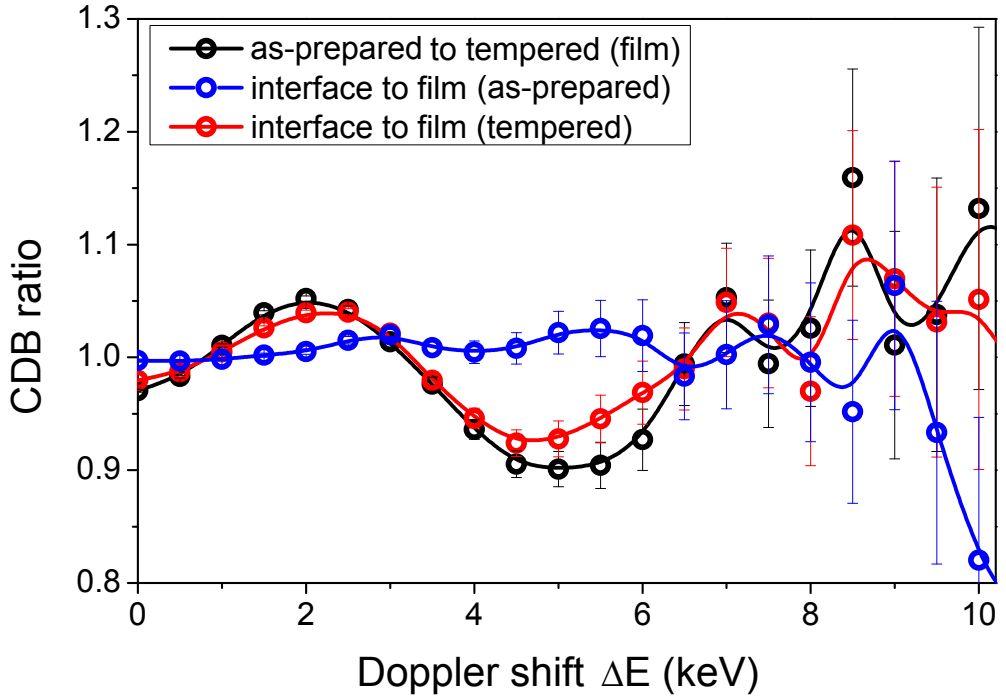

Figure 6.19: CDB ratio curves in A1 before ($\delta = 0.191$) and after tempering ($\delta = 0.619$): The spectra in the film were measured at $E_+ = 4\,\mathrm{keV}$, the spectra at the interface at $E_+ = 7\,\mathrm{keV}$. The ratio curve of the as-prepared film to the tempered film shows a similar signature as oxygen-rich samples in figure 6.11. Before tempering, in the as-prepared sate, no significant differences could be detected between interface and film. After tempering, the ratio curve reveals a lower oxygen deficiency δ close to the interface.

temperatures of 240 °C applying a slow heating ramp. This temperature is relatively low compared to those reported for bulk YBCO in literature, e. g. 350 °C observed in electric resistance [164] or 400 °C in PAS measurements [155]. However, in YBCO films, similarly low onset temperatures have been observed by other techniques, such as 250 °C by a combination of oxygen tracer diffusion and Secondary Ion Mass Spectroscopy (SIMS) [165]. In A1, for temperatures up to 350 °C, oxygen diffusion is slow which makes the tempering time a well suited parameter for controlling the oxygen deficiency. Moreover, after holding A1 for a longer time at these relatively low temperatures and then slowly approaching 400 °C, the total increase of δ was smaller than in C1 which was abruptly heated up to 400 °C. The tempering process applied in Universität Augsburg involved a continuous and relatively slow increase up to the maximum temperature as described in section 6.3. This explains why here the different tempering times led to a variation of δ and it is assumed that the duration of the heating ramp was a decisive factor for the finally obtained δ. Contrariwise, the phase of cooling down did presumably not affect δ as seen for A1 and C1 in figure 6.16.

Beyond these aspects, the found inhomogeneity of the oxygen deficiency with depth in sample A1 after tempering is of high interest. Since this sample was also hold at 400 °C for several minutes and due to the described step-like behavior of $S(t)$ at both probed incident energies (figure 6.16(b)), it is assumed that the observed depth dependency depicts a state of thermodynamic equilibrium at the respective temperature. Thus, according to the diffusion equation [166], in this stationary state δ has to decrease linearly with depth, which corresponds to a linearly decreasing S. The convolution of such a depth dependency with a Makhovian implantation profile was found to be able to explain the respective $S(E_+)$ detected after tempering for incident energies $4 \leq E_+ \leq 8\,\mathrm{keV}$, where positrons are mostly implanted into the YBCO film. However, in this energy range, the Makhovian implantation profile is already relatively broad and hence, a reliable extraction of a function describing the depth dependent behavior of S is not possible from the measured data. Nevertheless, it remains the question why film A1 shows a depth dependent behavior, whereas in all other films S was more or less constant in depth. In any case, the equilibrium concentration of oxygen is apparently determined by the microscopic processes between surface and vacuum leading to an oxygen exchange. In thermodynamic equilibrium, a δ non-constant in depth can be understood when an additional oxygen exchange at the interface between the YBCO film and the STO substrate locally influences the equilibrium concentration of oxygen in the YBCO film near the substrate. If this concentration is different from that at the surface, δ shows a linear transition between both sides of the film. The reason why such processes at the interface influenced the oxygen content in only one film, remains unclear. Possibly, this behavior is connected to the found inhomogeneities of S_{STO} described in section 6.5 or to vacancies present in STO substrates [18, 162, 163]. Moreover, long-term effects due to the storage in silica gel could play a role, since the sample A1 was tempered one year after its growth whereas the other ones were heat treated directly after their growth or, in the case of C1, one month later.

All these phenomena are connected to the mobility of oxygen in YBCO. Typical diffusion lengths were determined in [165] based on the experimental data of several studies for YBCO bulk samples. Assuming a heat treatment at 430 °C for 20 minutes, diffusion lengths of 10 nm along the c-axis and 6 μm along the a- and b-directions were reported. The short value for the c-direction fails to explain the observed temperature-induced increase of δ in the films. Based on the present results, this value must be exceeded in the investigated thin YBCO films by one order of magnitude or even more. An extraordinarily high oxygen mobility along the c-axis has been reported in various studies on YBCO thin films, e. g. in [167] for magnetron sputtered or in [165] for laser ablated YBCO films. Possible origins for this high mobility could be the presence of metallic vacancies which facilitate the motion of oxygen along c. As discussed in section 6.4.2, their presence cannot be excluded with the results of the present work. In order to obtain a complete picture of oxygen

diffusion in thin YBCO films, also purity and lateral homogeneity of the film surface and interface to the substrate should be taken into account and investigated in more detail.

Summary

The presented experiments showed that in-situ DBS at elevated temperatures with a highly intense positron beam is a valuable tool for the investigation of oxygen diffusion out of YBCO films. The observations enabled the revealing of important aspects of this process. By temperature dependent DBS, various characteristics were observed such as (i) an onset temperature of 240 °C, (ii) fast reaching of the thermodynamic equilibrium of the oxygen depth distribution at 400 ° within minutes, (iii) dependence of the final oxygen equilibrium concentration on the heating ramp and (iv) the possible occurrence of a depth dependent decrease of δ in films with increased oxygen deficiency after heat treatment. These phenomena are of great importance for the proper preparation of thin YBCO films with a well defined oxygen deficiency δ. In order to fully understand their background, depth dependent in-situ DBS at elevated temperatures, possibly with an improved experimental set-up which additionally allows laterally resolved measurements at the same time, is a promising experiment, which should be combined with complementary techniques.

6.7 Conclusion

It is well known that the oxygen deficiency δ determines the outstanding electric properties of YBCO, including its HTSC and, probably intertwined, CDW order. Earlier PAS studies published in literature have implied the potential of positrons for probing metallic vacancies and oxygen deficiency in this system. Aim of the present study was to systematically investigate the capability of a positron beam for probing the oxygen deficiency in thin YBCO films using the (C)DBS technique. For this purpose, comprehensive theoretical and experimental studies were combined. The accompanying calculations revealed an exotic behavior of the positrons in the complex crystal structure, which cannot be described by classical models used for PAS studies in metals or semiconductors. Interestingly, positrons probe exclusively the plane of varying oxygen content and hence, are highly sensitive to δ. Surprisingly, this sensitivity, in most cases, is even maintained for positrons trapped in potentially present metallic vacancies. In high-quality single-crystalline thin YBCO films, prepared and well characterized by complementary techniques at Universität Augsburg, the results of the calculations were experimentally confirmed. The measurements revealed a linear correlation between the Doppler broadening of the annihilation radiation and the oxygen deficiency δ, which was independently found in various different (C)DBS experiments and observed directly in the film and also at the interface region close to the STO

substrate. This correlation was also exhibited by the easily accessible S-parameter, which can be measured within one minute at the reactor based beam NEPOMUC but would also be well detectable with commonly used, low-intensity β^+-emitter based positron beams in conventional laboratories. In combination with the highly intense NEPOMUC beam and the high lateral resolution and wide temperature range available for measurements at the CDB spectrometer, the found S-δ correlation enabled novel experiments. Thus, unique insights into the lateral variation of δ in single films and the out-diffusion of oxygen were gained.

The CDBS results strongly suggest to apply low ambient pressures during heat treatment in order to further increase the homogeneity of monocrystalline thin YBCO films. Moreover, a promising approach for an enhancement of the film quality is the use of highly homogeneous STO substrate wafers. These could be obtained by the growth of additional STO by PLD onto the STO substrate prior to the deposition of YBCO. Another important key for improving the quality of the YBCO films is the complete understanding of the oxygen diffusion and the role of surface and interface effects in this process in order to obtain films with a well defined reduced oxygen content and highest spatial homogeneity. This study clearly showed that depth and temperature dependent DBS at the NEPOMUC beam reveals valuable information on oxygen diffusion. The present results strongly suggest to use slow heating ramps during tempering YBCO films in order to precisely manipulate their oxygen deficiency. The preconditions which lead to a oxygen distribution homogeneous in depth have to be further investigated. Single-crystalline YBCO samples with presumably unprecedented quality can be prepared in future taking into account the present results and further investigating a few remaining unclear aspects. The use of such specimens in fundamental experiments with the scope of investigating HTSC and CDW order could simplify the basic understanding of these phenomena and their interplay. Moreover, such high-quality samples are expected to be well suited for technical applications of YBCO, e. g. in high field magnets.

Chapter 7

7 Conclusion and Outlook

In the present work, CDBS at the NEPOMUC beam was used in order to study open volume defects in monocrystalline specimens of MnSi and YBCO. The studies involved the determination of different species of point defects and their concentration. In MnSi, crystals with a varying chemical composition were investigated. The presence of Mn vacancies was proven in all samples. Their concentration can be efficiently reduced by an initial net weight excess of Mn in the first step of preparation. In single-crystalline thin films of YBCO, (C)DBS results were found to strongly correlate with the oxygen deficiency which defines the electric transport properties and hence, is a crucial parameter for the functionality in possible applications.

It was demonstrated that (C)DBS is a powerful technique for the detailed investigation of lattice defects in binary compounds and even more complex materials such as YBCO. The same experimental procedure was applied for both investigated systems and led to valuable results. For a start, the evaluation of the lineshape parameters S and W identifies relevant effects affecting the Doppler broadening of the annihilation line. An unambiguous interpretation of these parameters is possible after analyzing CDB spectra. In both systems, the comparison of measured and calculated CDB spectra enabled the identification of the positron annihilation sites such as, e. g., Mn vacancies in MnSi. In YBCO, the situation was found to be more complex. Nevertheless, changes in the CDB signatures could be clearly attributed to a varying oxygen content which affects nearly all positron states in the system in a similar way. Moreover, the calculations enabled to study positron wave function effects by visualizing the positron probability density. In YBCO, such effects strongly enhance the sensitivity of positrons on the oxygen deficiency. The high reliability of the CDBS results was proven for both systems. In the case of MnSi, the CDBS and complementary PALS measurements were independently analyzed in order to determine the Mn vacancy concentration. An excellent agreement was found between the results of both techniques using different methods of positron generation. For MnSi, CDBS was

shown to be even a more powerful technique because PALS – in contrast to CDBS – cannot distinguish between Mn and Si vacancies. The latter ones were not detected and only play a minor role of in this system as predicted by calculated effective formation energies of point defects in MnSi. Also in YBCO, (C)DBS was applied successfully and yielded trustworthy results as shown by repeated measurements. In combination with XRD data obtained by cooperation partners, the (C)DBS results could be safely interpreted in terms of the oxygen deficiency despite the complexity of the structure.

These results enabled further experiments at the NEPOMUC CDB spectrometer with its unique experimental prospects. As shown by the characterization of the beam spot size at the sample position, the lateral resolution, especially for low incident energies, was further improved within this work. Moreover, the construction of a new sample heating device made a new maximum temperature available for experiments. Thus, studies using spatially resolved DBS and in-situ DBS at high temperatures were possible profiting from the high countrate at NEPOMUC. In the case of YBCO, the preparation of homogeneous samples can be further improved due to the results obtained by laterally resolved DBS. These suggest applying low ambient pressures when YBCO films are tempered in order to decrease their oxygen content. Furthermore, deep insights into the process of outdiffusion of oxygen atoms from the YBCO films were gained by in-situ DBS at elevated temperatures. Tempering in a range below 350 °C leads to a slow reduction of the oxygen content. Moreover, it was found that depth dependencies in the oxygen content of YBCO films can occur after tempering. In the case of MnSi, laterally resolved DBS revealed that Mn vacancies distribute homogeneously during crystal growth, even in the case of concentration gradients in the initial rods used for crystal growth. Hence, (C)DBS at NEPOMUC was proven to expand the field for novel applications of positron beams.

Beyond the scope of this thesis, numerous experiments were conducted within the NEPOMUC team for or together with external users at the FRM II, e. g., on bulk metallic glasses, Cu-In-Ga-Se solar cells, thin Ag-Au bilayers [168], Heusler alloys [72], FePt single crystals, irradiated W, Li-ion batteries, oxide-dispersion strengthened steels [169], silica gel and spider silk materials.

In future experiments, (C)DBS will benefit from the use of the presented novel pixelated HPGe detectors. A new acquisition system and an elaborated algorithm for their read-out was used. It was proven that reliable, high-quality CDB spectra can be recorded with these detectors using the novel read-out. Now, the detection of the momentum of the annihilating electron-positron pair in 3D is possible. This technique will facilitate the identification of various positron states present in a specimen. In the CDB spectrometer, which is currently replaced by a new set-up, experiments will be conducted with an anticipated beam diameter smaller than 10 μm and thus, profit from an even higher lateral resolution than in the present.

Appendix

Abbreviations

ACAR – angular correlation of the annihilation radiation
ADC – analog-to-digital converter
CDB(S) – coincident Doppler broadening (spectroscopy)
CDW – charge-density-wave
DB(S) – Doppler broadening (spectroscopy)
DFT – density functional theory
FRM II – Forschungsreaktor München II
FWHM – full width at half maximum
GGA – generalized gradient approximation
GIPS – gamma induced positron source at Helmholtz-Zentrum Dresden-Rossendorf
HMA – high-momentum area
HPGe – high-purity germanium
HTSC – high-temperature superconductivity
IPM – independent particle model
LDA – local density approximation
MCA – multi-channel analyzer
NEPOMUC – neutron induced positron source Munich at the FRM II
NMR – nuclear magnetic resonance
PAES – positron-induced Auger electron spectroscopy
PALS – positron annihilation lifetime spectroscopy
PAS – positron annihilation spectroscopy
PGAA – prompt-gamma neutron activation analysis
PLD – pulsed laser deposition
RRR – residual resistivity ratio
SANS – small angle neutron scattering
STO – $SrTiO_3$
UHV – ultra-high vacuum
XRD – X-ray diffraction
YBCO – $YBa_2Cu_3O_{7-\delta}$

Enhancement Factors

As described in chapter 3, CDB spectra and lifetimes of positron states were calculated by use of the MIKA Doppler software package. Here, the used parametrizations for describing electron-positron correlations are given; they can be found in the manual for MIKA Doppler [75]. As mentioned, the respective factor $g\left(0, n_+, n_-\right)$ in equation 3.3 is denoted as enhancement factor γ in the limit of a vanishing positron density which is implemented within MIKA Doppler. In this software, γ is evaluated as function of

$$r_\mathrm{s} = \sqrt[3]{\frac{3}{4\pi n_-}}$$

which depends on the undistorted electron density n_- at the position of the positron.

In the calculations for pure elements, the Au-Cu system and YBCO, a Generalized Gradient Approximation (GGA) for the enhancement with a parametrization proposed by Arponnen and Pajanne [75] was used. Here, γ is determined from a Local Density Approximation (LDA) by

$$\gamma_\mathrm{LDA}\left(r_\mathrm{s}\right) = 1 + 1.23 \cdot r_\mathrm{s} - 0.91657 \cdot r_\mathrm{s}^{3/2} + 1.0564 \cdot r_\mathrm{s}^2 - 0.3455 \cdot r_\mathrm{s}^{5/2} + \frac{1}{6} \cdot r_\mathrm{s}^3,$$

This LDA approach is corrected by

$$\gamma_\mathrm{GGA} = 1 + (\gamma_\mathrm{LDA} - 1)e^{-0.22\varepsilon}$$

in order to model effects of the GGA scheme [80]. The parameter

$$\varepsilon = \frac{\left|\nabla n_-\right|^2}{(n_- q_{TF})^2}$$

describes the variation of the electron density with the Thomas-Fermi screening length

$$q_{TF} = (\frac{4}{\pi}(3\pi^2 n_-)^{\frac{1}{3}})^{1/2}.$$

In the calculations for MnSi, a LDA model with a parametrization proposed by Boronski and Nieminen was used [77]. With the function

$$\gamma_\mathrm{LDA-BN}\left(r_\mathrm{s}\right) = 1 + 1.23 \cdot r_\mathrm{s} + 0.8295 \cdot r_\mathrm{s}^{3/2} - 1.26 \cdot r_\mathrm{s}^2 + 0.3286 \cdot r_\mathrm{s}^{5/2} + \frac{1}{6} \cdot r_\mathrm{s}^3$$

best agreement between calculated and measured positron lifetimes was found.

Data Quality

As described in section 4.1, external influences in the experimental hall of the FRM II lead to disturbances in the detection of (C)DBS spectra at NEPOMUC. Within the present thesis, this influence was minimized by an optimized electrostatic insulation of the detection system. However, measurements still can be affected by disturbances in the detection system and thus, data have to be analyzed carefully. The comparison of the four used detectors reveals detailed information on systematic changes in the spectra and influence of external effects. Within the recent years, the following systematic aspects have been found and should be considered in the data evaluation.

In general, external disturbances such as motion of the crane close to the positron beamline or the use of strong magnets in the experimental hall lead to low countrates. By analyzing the number of counts in the recorded spectra, measurements disturbed by such effects can be easily identified and have not been considered in the evaluation. Care was taken in order to avoid any mechanical contact between the HPGe detectors and the spectrometer itself and cables that could lead to vibrations which deteriorate the energy resolution of the detectors. Thus, the S-parameter was found to be rather insensitive on external influence. Only two effects were found to affect the detected S-parameters: (i) From repeated S-parameter measurements at constant conditions it is known that the standard deviation of the detected values for S is a factor of 1.5 larger than expected from the statistical error of S. This is attributed to the electronic noise in the experimental hall. (ii) Sometimes, abrupt changes in the energy resolution of the system were observed which lead to shifts in the detected S-parameters. Most probably, these changes are caused by the digital signal processors applied for the read out of the HPGe detectors. Such changes can be induced by switching pulses at the spectrometer or in its vicinity. In principle, the same observations were made for the W-parameter. However, W also changes when the background of γ radiation in the experimental hall alters. Thus, W is more sensitive on external influences than S. In order to minimize the influence of such disturbances, DBS measurements were routinely repeated. Detectors only have been considered for the data evaluation if repeated measurements of S and W yielded identical results.

CDBS spectra were measured with relatively short measurement times and summed up afterwards for increasing their statistics. Before summing up, the stable operation of the detection system was checked by a quick analysis of the various low-statistics CDB spectra. Thus, the effective energy resolution and the peak-to-background ratio during the detection could be checked. In the case of abrupt, significant deterioration of these observables, the respective low-statistics spectra were not used for the accumulation of high statistics by summing up. At this point, it is emphasized that in both investigated systems, MnSi and YBCO, thus obtained CDB spectra, S- and W-parameters showed the same qualitative and quantitative behavior. Moreover, all measured CDB spectra

are well explained by theoretically calculated ones. Thus, it is concluded that a careful investigation of data as described above, which only is based on detectors stably running during a whole measurement cycle (with typical durations of several days), allows the reliable extraction of quantitative CDBS results.

Lens Voltages

As described in section 4.2, the electrostatic focusing system of the CDB spectrometer was modified. For an optimal lateral resolution, the lens voltage U_4 was readjusted by simulations based on a finite-element method. In figure A.1, the tested settings for $U_4\,(E_+)$ are shown. In real measurements, i. e. for arbitrary values of E_+, $U_4\,(E_+)$ is obtained from a linear interpolation between the data points. With the new settings, an enhanced resolution was obtained as shown in figures 4.4 and 4.5. Alternatively, different settings were tested but led to a lower resolution. This was also the case for the old settings used in the original set-up [12]. The absolute values of the new and old settings are given in table A.1.

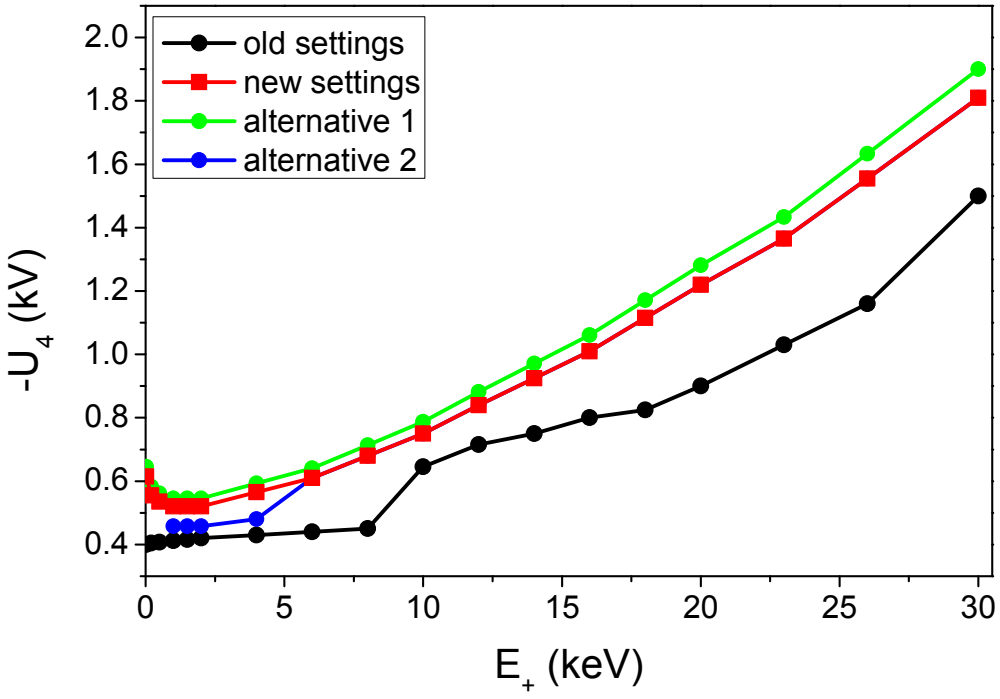

Figure A.1: Lens voltages U_4 in dependence on the incident positron energy E_+. The old settings were taken from [12]; the new settings were obtained as described in section 4.2 and yielded the optimal lateral resolution. For the given alternative settings, a lower resolution was found. Solid lines are guides to the eye.

E_+ (keV)	old	new
0.02	0.400	0.615
0.20	0.405	0.555
0.50	0.408	0.535
1.00	0.412	0.520
1.50	0.416	0.520
2.00	0.420	0.520
4.00	0.430	0.565
6.00	0.440	0.610
8.00	0.450	0.680
10.0	0.645	0.750
12.0	0.715	0.840
14.0	0.750	0.925
16.0	0.800	1.010
18.0	0.825	1.115
20.0	0.900	1.220
23.0	1.030	1.365
26.0	1.160	1.555
30.0	1.500	1.810

Table A.1: Values of new and old lens voltages $-U_4$ (kV) as shown in figure A.1.

Mn-Si Phase Diagram

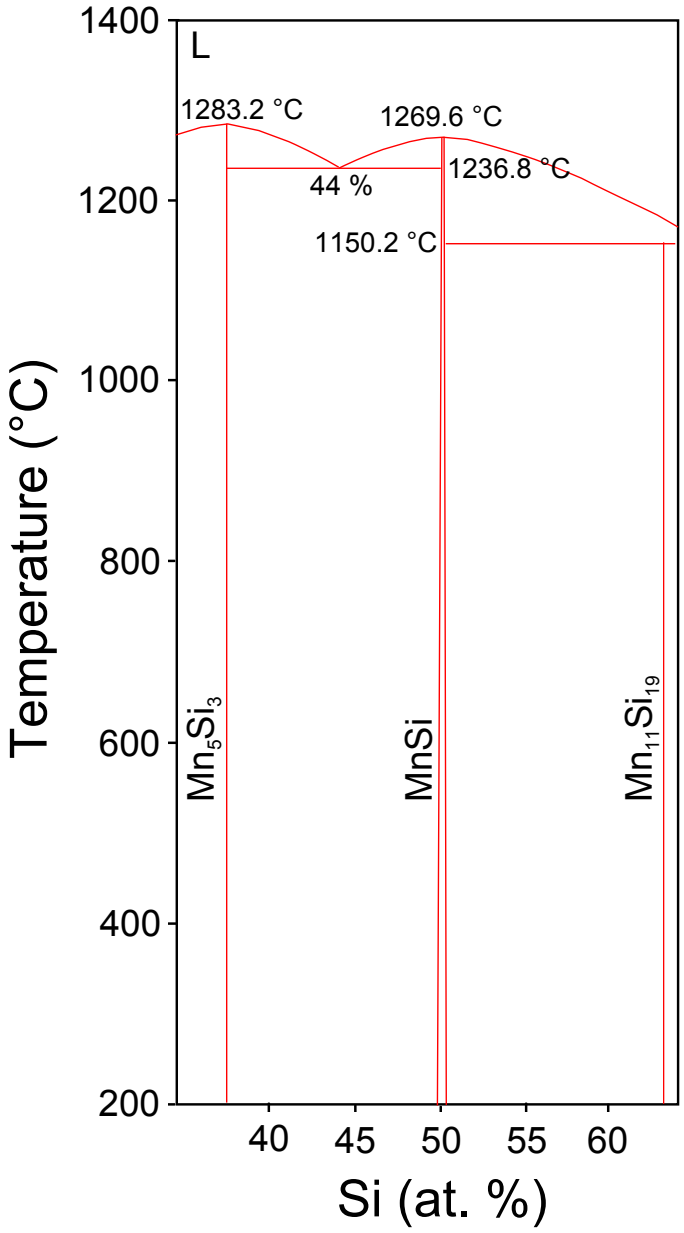

Figure A.2: Metallurgical phase diagram of Mn-Si in the regime of stoichiometry. Data taken from [107].

List of Publications

[P1] M. Reiner, T. Gigl, R. Jany, G. Hammerl, and C. Hugenschmidt. Detection and imaging of the oxygen deficiency in single crystalline $YBa_2Cu_3O_{7-\delta}$ thin films using a scanning positron beam. *Applied Physics Letters*, 106(11):111910, 2015.
Earlier version available online (open access). *ArXiv e-prints*, arXiv:1501.06383 [cond-mat.mtrl-sci], 2015.

[P2] M. Reiner, T. Gigl, and C. Hugenschmidt. Ab-initio calculation of CDB spectra - a case study on transition metals. *Journal of Physics: Conference Series*, 505(1):012025, 2014.

[P3] M. Reiner, P. Pikart, and C. Hugenschmidt. Thin film annealing and alloying of a Au/Cu two-layer system studied by positron annihilation spectroscopy. *Journal of Alloys and Compounds*, 587(0):515 – 519, 2014.

[P4] M. Reiner, P. Pikart, and C. Hugenschmidt. In-situ (C)DBS at high temperatures at the NEPOMUC positron beam line. *Journal of Physics: Conference Series*, 443(1):012071, 2013.

[P5] M. Reiner, P. Pikart, and C. Hugenschmidt. Annealing of thin metallic films studied by depth dependent DB-spectroscopy and free Ps annihilation. *Physics Procedia*, 35:104 – 110, 2012.

[P6] M. Reiner, A. Bauer, M. Leitner, W. Anwand, M. Butterling, T. Gigl, P. Kudejova, A. Wagner, C. Pfleiderer, and C. Hugenschmidt. Point defects in MnSi and their influence on magnetic properties. To be submitted for publication in Oct. 2015.

[P7] P. Parente, T. Leguey, V. de Castro, T. Gigl, M. Reiner, C. Hugenschmidt, and R. Pareja. Characterization of ion-irradiated ODS Fe-Cr alloys by doppler broadening spectroscopy using a positron beam. *Journal of Nuclear Materials*, 464(0):140 – 146, 2015.

[P8] C. Hugenschmidt, A. Bauer, P. Böni, H. Ceeh, S. W. H. Eijt, T. Gigl, C. Pfleiderer, C. Piochacz, A. Neubauer, M. Reiner, H. Schut, and J. Weber. Quality of Heusler single crystals examined by depth-dependent positron annihilation techniques. *Applied Physics A*, 119(3):997 – 1002, 2015.

[P9] T. Gigl, C. Piochacz, M. Reiner, and C. Hugenschmidt. Positronbeam for μm resolved coincident Doppler broadening spectroscopy at NEPOMUC. *Journal of Physics: Conference Series*, 505:012032, 2014.

[P10] C. Hugenschmidt, H. Ceeh, T. Gigl, F. Lippert, C. Piochacz, M. Reiner, K. Schreckenbach, S. Vohburger, Weber. J., and S. Zimnik. Positron beam characteristics at NEPOMUC upgrade. *Journal of Physics: Conference Series*, 505(1):012029, 2014.

[P11] B. Löwe, M. Reiner, W. Egger, C. Hugenschmidt, and G. Dollinger. A position sensitive germanium detector for the measurement of angular deviation of annihilation radiation. *Journal of Physics: Conference Series*, 443(1):012098, 2013.

[P12] C. Hugenschmidt, H. Ceeh, T. Gigl, F. Lippert, C. Piochacz, P. Pikart, M. Reiner, J. Weber, and S. Zimnik. The Upgrade of the Neutron Induced Positron Source NEPOMUC. *Journal of Physics: Conference Series*, 443:012079, 2013.

[P13] C. Hugenschmidt, C. Piochacz, M. Reiner, and K. Schreckenbach. The NEPOMUC upgrade and advanced positron beam experiments. *New Journal of Physics*, 14(5):055027, 2012.

[P14] M. A. Noah, D. Flötotto, Z. Wang, M. Reiner, C. Hugenschmidt, and E. J. Mittemeijer. Interdiffusion in epitaxial Ag/Au thin films; an AES sputter-depth profiling and positron annihilation study. In preparation for submission for publication.

Bibliography

[1] R. N. West. Positron studies of condensed matter. *Adv. Phys.*, 1973.

[2] M. J. Puska and R. M. Nieminen. Theory of positrons in solids and on solid surfaces. *Rev. Mod. Phys.*, 66(3):841–897, 1994.

[3] A. Dupasquier and A. P. Mills jr., editors. *Proceedings of the International School of Physics 'Enrico Fermi' – 125: Positron Spectroscopy of Solids.* IOS Press, 1995.

[4] F. Tuomisto and I. Makkonen. Defect identification in semiconductors with positron annihilation: Experiment and theory. *Rev. Mod. Phys.*, 85:1583–1631, 2013.

[5] A. Dupasquier, A. P. Mills jr., and R. S. Brusa, editors. *Proceedings of the International School of Physics 'Enrico Fermi' – 174: Physics with Many Positrons.* IOS Press, 2009.

[6] T. Torsti, T. Eirola, J. Enkovaara, T. Hakala, P. Havu, V. Havu, T. Höynälänmaa, J. Ignatius, M. Lyly, I. Makkonen, T. T. Rantala, J. Ruokolainen, K. Ruotsalainen, E. Räsänen, H. Saarikoski, and M. J. Puska. Three real-space discretization techniques in electronic structure calculations. *Phys. Status Solidi B*, 243(5):1016–53, 2006.

[7] P. J. Schultz and K. G. Lynn. Interaction of positron beams with surfaces, thin films, and interfaces. *Rev. Mod. Phys.*, 60(3):701–779, 1988.

[8] P. Coleman, editor. *Positron beams and their applications.* World Scientific, 2000.

[9] C. Hugenschmidt, C. Piochacz, M. Reiner, and K. Schreckenbach. The NEPOMUC upgrade and advanced positron beam experiments. *New J. Phys.*, 14(5):055027, 2012.

[10] C. Hugenschmidt, H. Ceeh, T. Gigl, F. Lippert, C. Piochacz, M. Reiner, K. Schreckenbach, S. Vohburger, J. Weber, and S. Zimnik. Positron beam characteristics at NEPOMUC upgrade. *J. Phys.: Conf. Ser.*, 505(1):012029, 2014.

[11] C. Hugenschmidt, H. Ceeh, T. Gigl, F. Lippert, C. Piochacz, P. Pikart, M. Reiner, J. Weber, and S. Zimnik. The upgrade of the neutron induced positron source NEPOMUC. *J. Phys.: Conf. Ser.*, 443:012079, 2013.

[12] M. Stadlbauer. *Investigation of the chemical vicinity of defects in Mg and AZ31 with positron coincident Doppler broadening spectroscopy.* PhD thesis, Technische Universität München, 2008.

[13] M. Stadlbauer, C. Hugenschmidt, and K. Schreckenbach. New design of the CDB-spectrometer at NEPOMUC for T-dependent defect spectroscopy in Mg. *Appl. Surf. Sci.*, 255(1):136 – 138, 2008. Proceedings of the Eleventh International Workshop on Slow Positron Beam Techniques for Solids and Surfaces.

[14] M. Reiner, P. Pikart, and C. Hugenschmidt. In-situ (C)DBS at high temperatures at the NEPOMUC positron beam line. *J. Phys.: Conf. Ser.*, 443(1):012071, 2013.

[15] M. Stadlbauer, C. Hugenschmidt, K. Schreckenbach, and P. Böni. Investigation of the chemical vicinity of crystal defects in ion-irradiated Mg and a Mg-Al-Zn alloy with coincident Doppler broadening spectroscopy. *Phys. Rev. B*, 76:174104, 2007.

[16] C. Hugenschmidt, P. Pikart, M. Stadlbauer, and K. Schreckenbach. High elemental selectivity to Sn submonolayers embedded in Al using positron annihilation spectroscopy. *Phys. Rev. B*, 77:092105, 2008.

[17] C. Hugenschmidt, N. Qi, M. Stadlbauer, and K. Schreckenbach. Correlation of mechanical stress and Doppler broadening of the positron annihilation line in Al and Al alloys. *Phys. Rev. B*, 80:224203, 2009.

[18] D. J. Keeble, R. A. Mackie, W. Egger, B. Löwe, P. Pikart, C. Hugenschmidt, and T. J. Jackson. Identification of vacancy defects in a thin film perovskite oxide. *Phys. Rev. B*, 81:064102, 2010.

[19] B. Oberdorfer, E.-M. Steyskal, W. Sprengel, W. Puff, P. Pikart, C. Hugenschmidt, M. Zehetbauer, R. Pippan, and R. Würschum. *In Situ* probing of fast defect annealing in Cu and Ni with a high-intensity positron beam. *Phys. Rev. Lett.*, 105:146101, 2010.

[20] R. M. Hengstler-Eger, P. Baldo, L. Beck, J. Dorner, K. Ertl, P. B. Hoffmann, C. Hugenschmidt, M. A. Kirk, W. Petry, P. Pikart, and A. Rempel. Heavy ion irradiation induced dislocation loops in AREVA's M5® alloy. *J. Nucl. Mater.*, 423(1-3):170 – 182, 2012.

[21] P. Pikart, C. Hugenschmidt, M. Horisberger, Y. Matsukawa, M. Hatakeyama, T. Toyama, and Y. Nagai. Positron annihilation in Cr, Cu, and Au layers embedded in Al and quantum confinement of positrons in Au clusters. *Phys. Rev. B*, 84:014106, 2011.

[22] R. Gilles, M. Hofmann, F. Johnson, Y. Gao, D. Mukherji, C. Hugenschmidt, and P. Pikart. Analysis of antiphase domain growth in ternary FeCo alloys after different cooling rates and annealing treatments using neutron diffraction and positron annihilation. *J. Alloys Compd.*, 509(2):195 – 199, 2011.

[23] Y. Ishikawa, G. Shirane, J. A. Tarvin, and M. Kohgi. Magnetic excitations in the weak itinerant ferromagnet MnSi. *Phys. Rev. B*, 16:4956–4970, 1977.

[24] H. J. Williams, J. H. Wernick, R. C. Sherwood, and G. K. Wertheim. Magnetic properties of the monosilicides of some 3d transition elements. *J. Appl. Phys.*, 37(3):1256–1256, 1966.

[25] L. M. Levinson, G. H. Lander, and M. O. Steinitz. Anomalous magnetic behavior of MnSi. *AIP Conf. Proc.*, 10(1):1138–1142, 1973.

[26] D. Bloch, J. Voiron, V. Jaccarino, and J. H. Wernick. The high field-high pressure magnetic properties of MnSi. *Phys. Lett. A*, 51(5):259 – 261, 1975.

[27] K. Motoya, H. Yasuoka, Y. Nakamura, and J. H. Wernick. Helical spin structure in MnSi - NMR studies. *Solid State Commun.*, 19(6):529 – 531, 1976.

[28] Y. Ishikawa, K. Tajima, D. Bloch, and M. Roth. Helical spin structure in manganese silicide MnSi. *Solid State Commun.*, 19(6):525 – 528, 1976.

[29] A. Bauer, M. Garst, and C. Pfleiderer. Specific heat of the skyrmion lattice phase and field-induced tricritical point in MnSi. *Phys. Rev. Lett.*, 110:177207, 2013.

[30] M. Janoschek, M. Garst, A. Bauer, P. Krautscheid, R. Georgii, P. Böni, and C. Pfleiderer. Fluctuation-induced first-order phase transition in Dzyaloshinskii-Moriya helimagnets. *Phys. Rev. B*, 87:134407, 2013.

[31] S. A. Brazovskii. Phase transition of an isotropic system to a nonuniform state. *Sov. J. Exp. Theor. Phys.*, 41:85, 1975.

[32] C. Pfleiderer, D. Reznik, L. Pintschovius, H. v. Löhneysen, M. Garst, and A. Rosch. Partial order in the non-Fermi-liquid phase of MnSi. *Nature*, 427(6971):227–231, 2004.

[33] R. Ritz, M. Halder, M. Wagner, C. Franz, A. Bauer, and C. Pfleiderer. Formation of a topological non-Fermi liquid in MnSi. *Nature*, 497(7448):231–234, 2013.

[34] S. Mühlbauer, B. Binz, F. Jonietz, C. Pfleiderer, A. Rosch, A. Neubauer, R. Georgii, and P. Böni. Skyrmion lattice in a chiral magnet. *Science*, 323(5916):915–919, 2009.

[35] C. Pfleiderer, T. Adams, A. Bauer, W. Biberacher, B. Binz, F. Birkelbach, P. Böni, C. Franz, R. Georgii, M. Janoschek, F. Jonietz, T. Keller, R. Ritz, S. Mühlbauer, W. Münzer, A. Neubauer, B. Pedersen, and A. Rosch. Skyrmion lattices in metallic and semiconducting B20 transition metal compounds. *J. Phys.: Condens. Matter*, 22(16):164207, 2010.

[36] F. Jonietz, S. Mühlbauer, C. Pfleiderer, A. Neubauer, W. Münzer, A. Bauer, T. Adams, R. Georgii, P. Böni, R. A. Duine, et al. Spin transfer torques in MnSi at ultralow current densities. *Science*, 330(6011):1648–1651, 2010.

[37] M. K. Wu, J. R. Ashburn, C. J. Torng, P. H. Hor, R. L. Meng, L. Gao, Z. J. Huang, Y. Q. Wang, and C. W. Chu. Superconductivity at 93 K in a new mixed-phase Y-Ba-Cu-O compound system at ambient pressure. *Phys. Rev. Lett.*, 58:908–910, 1987.

[38] S. Hikami, T. Hirai, and S. Kagoshima. High transition temperature superconductor: Y-Ba-Cu oxide. *Jpn. J. Appl. Phys.*, 26(4A):L314, 1987.

[39] J. G. Bednorz and K. A. Müller. Possible high T_c superconductivity in the Ba – La – Cu – O system. *Z. Phys. B*, 64(2):189–193, 1986.

[40] E. Fradkin and S. A. Kivelson. High-temperature superconductivity: Ineluctable complexity. *Nat. Phys.*, 8:864–866, 2012.

[41] G. Ghiringhelli, M. Le Tacon, M. Minola, S. Blanco-Canosa, C. Mazzoli, N. B. Brookes, G. M. De Luca, A. Frano, D. G. Hawthorn, F. He, T. Loew, M. Moretti Sala, D. C. Peets, M. Salluzzo, E. Schierle, R. Sutarto, G. A. Sawatzky, E. Weschke, B. Keimer, and L. Braicovich. Long-range incommensurate charge fluctuations in (Y,Nd)$Ba_2Cu_3O_{6+x}$. *Science*, 337(6096):821–825, 2012.

[42] J. Chang, E. Blackburn, A. T. Holmes, N. B. Christensen, J. Larsen, J. Mesot, L. Ruixing, D. A. Bonn, W. N. Hardy, A. Watenphul, M. v. Zimmermann, E. M. Forgan, and S. M. Hayden. Direct observation of competition between superconductivity and charge density wave order in $YBa_2Cu_3O_{6.67}$. *Nat. Phys.*, 8:871–876, 2012.

[43] Superconducting wire breaks record, 2006. Online available at http://phys.org/news105718161.html; lastly accessed on 17th April 2015.

[44] E. M. Leung. Superconducting fault current limiters. *IEEE Power Eng. Rev.*, 20(8):15–18, 30, 2000.

[45] New world record for superconducting magnet set, 2007. Online available at http://phys.org/news105718161.html; lastly accessed on 17th April 2015.

[46] P. A. M. Dirac. A theory of electrons and protons. *Proc. R. Soc. London, Ser. A*, 126(801):360–365, 1930.

[47] P. A. M. Dirac. Quantised singularities in the electromagnetic field. *Proc. R. Soc. London, Ser. A*, 133(821):60–72, 1931.

[48] C. D. Anderson. The positive electron. *Phys. Rev.*, 43(6):491–494, 1933.

[49] H. Huomo, A. Vehanen, M. D. Bentzon, and P. Hautojärvi. Positron diffusion in Mo: The role of epithermal positrons. *Phys. Rev. B*, 35(15):8252–8255, 1987.

[50] D. T. Britton, P. C. Rice-Evans, and J. H. Evans. Epithermal effects in positron depth profiling measurements. *Phil. Mag. Let.*, 57(3):165–169, Jul 1988.

[51] P. A. Huttunen, J. Mäkinen, D. T. Britton, E. Soininen, and A. Vehanen. Temperature dependence of thermal positron branching at metal surfaces. *Phys. Rev. B*, 42(3):1560–1573, 1990.

[52] A. Weiss, R. Mayer, M. Jibaly, C. Lei, D. Mehl, and K. G. Lynn. Auger-electron emission resulting from the annihilation of core electrons with low-energy positrons. *Phys. Rev. Lett.*, 61:2245–2248, 1988.

[53] K. O. Jensen and A. Weiss. Theoretical study of the application of positron-induced Auger-electron spectroscopy. *Phys. Rev. B*, 41:3928–3936, 1990.

[54] A. P. Mills jr. Brightness enhancement of slow positron beams. *Appl. Phys.*, 23(2):189–191, 1980.

[55] G. S. Adkins. Radiative corrections to positronium decay. *Ann. Phys.*, 146(1):78 – 128, 1983.

[56] J. Mayer. *High energy resolution and first time-dependent positron annihilation induced Auger-electron spectroscopy.* PhD thesis, Technische Universität München, 2010.

[57] P. Hautojärvi and C. Corbel. Positron spectroscopy of defects in metals and semiconductors. In A. Dupasquier and A. P. Mills jr., editors, *Proceedings of the International School of Physics 'Enrico Fermi' – 125: Positron Spectroscopy of Solids.* IOS press, 1995.

[58] M. Reiner. *Depth resolved Doppler broadening spectroscopy of thin metallic films with a mono energetic positron beam.* Diploma thesis, Technische Universität München, 2011.

[59] G. Dlubek. Positron studies of decomposition phenomena in Al alloys. *Mat. Sci. For.*, 13:11–32, 1987.

[60] M. J. Puska, P. Lanki, and R. M. Nieminen. Positron affinities for elemental metals. *J. Phys.: Condens. Matter*, 1(35):6081, 1989.

[61] M. Haaks, T. E. M. Staab, and K. Maier. Analyzing the high-momentum part of positron annihilation Doppler spectra with a single germanium detector. *Nucl. Instrum. Meth. A*, 569(3):829 – 836, 2006.

[62] M. Reiner, P. Pikart, and C. Hugenschmidt. Thin film annealing and alloying of a Au/Cu two-layer system studied by positron annihilation spectroscopy. *J. Alloys Compd.*, 587:515–519, 2014.

[63] P. Asoka-Kumar, M. Alatalo, V. J. Ghosh, A. C. Kruseman, B. Nielsen, and K. G. Lynn. Increased elemental specificity of positron annihilation spectra. *Phys. Rev. Lett.*, 77(10):2097–2100, 1996.

[64] P. E. Mijnarends, A. C. Kruseman, A. van Veen, H. Schut, and A. Bansil. Two-detector Doppler broadening study of enhancement in Al. *J. Phys.: Condens. Matter*, 10:10383–10390, 1998.

[65] P. Pikart and C. Hugenschmidt. Determination of electron binding energies in two-dimensional coincident Doppler broadening spectra. *J. Phys.: Conf. Ser.*, 443(1):012089, 2013.

[66] P. Pikart. *Advances in Coincident Doppler Broadening Spectroscopy: Element Selective Studies on Metallic Nanolayers with Monoenergetic Positrons.* PhD thesis, Technische Universität München, 2012.

[67] P. Pikart and C. Hugenschmidt. Novel data evaluation algorithm for coincident Doppler broadening spectroscopy. *Nucl. Instrum. Meth. A*, 750(0):61 – 68, 2014.

[68] R. Krause-Rehberg and H. S. Leipner. *Positron Annihilation in Semiconductors, Defect studies.* Springer, 1999.

[69] B. Bergersen, E. Pajanne, P. Kubica, M. J. Stott, and C. H. Hodges. Positron diffusion in metals. *Solid State Commun.*, 15(8):1377 – 1380, 1974.

[70] M. Reiner, P. Pikart, and C. Hugenschmidt. Annealing of thin metallic films studied by depth dependent DB-spectroscopy and free Ps annihilation. *Phys. Procedia*, 35:104–110, 2012.

[71] E. Soininen, J. Mäkinen, D. Beyer, and P. Hautojärvi. High-temperature positron diffusion in Si, GaAs, and Ge. *Phys. Rev. B*, 46(20):13104–13118, 1992.

[72] C. Hugenschmidt, A. Bauer, P. Böni, H. Ceeh, S. W. H. Eijt, T. Gigl, C. Pfleiderer, C. Piochacz, A. Neubauer, M. Reiner, H. Schut, and J. Weber. Quality of Heusler single crystals examined by depth-dependent positron annihilation techniques. *Appl. Phys. A*, 2015.

[73] A. van Veen, H. Schut, M. Clement, J. M. M. de Nijs, A. Kruseman, and M. R. IJpma. VEPFIT applied to depth profiling problems. *Appl. Surf. Sci.*, 85:216 – 224, 1995. Proceedings of the Sixth International Workshop on Slow-Positron Beam Techniques for Solids and Surfaces.

[74] G. C. Aers, P. A. Marshall, T. C. Leung, and R. D. Goldberg. Defect profiling in multilayered systems using mean depth scaling. *Appl. Surf. Sci.*, 85:196 – 209, 1995. Proceedings of the Sixth International Workshop on Slow-Positron Beam Techniques for Solids and Surfaces.

[75] Laboratory of Physics, Helsinki University, Helsinki. *Doppler: A program to model positron states and annihilation in solids*, 2003.

[76] M. Reiner, T. Gigl, and C. Hugenschmidt. Ab-initio calculation of CDB spectra - a case study on transition metals. *J. Phys.: Conf. Ser.*, 505(1):012025, 2014.

[77] E. Boroński and R. M. Nieminen. Electron-positron density-functional theory. *Phys. Rev. B*, 34:3820–3831, 1986.

[78] M. J. Puska and R. M. Nieminen. Defect spectroscopy with positrons: A general calculational method. *J. Phys. F. Met. Phys.*, 13(2):333, 1983.

[79] M. J. Puska. Positron states and annihilation at defects in semiconductors. *Mat. Sci. For.*, 255:171–178, 1997.

[80] B. Barbiellini, M. J. Puska, T. Torsti, and R. M. Nieminen. Gradient correction for positron states in solids. *Phys. Rev. B*, 51:7341–4, 1995.

[81] M. Hakala, M. J. Puska, and R. M. Nieminen. Momentum distributions of electron-positron pairs annihilating at vacancy clusters in Si. *Phys. Rev. B*, 57:7621–7627, 1998.

[82] V. J. Ghosh, M. Alatalo, P. Asoka-Kumar, B. Nielsen, K. G. Lynn, A. C. Kruseman, and P. E. Mijnarends. Calculation of the Doppler broadening of the electron-positron annihilation radiation in defect-free bulk materials. *Phys. Rev. B*, 61:10092–9, 2000.

[83] A. Calloni, A. Dupasquier, R. Ferragut, P. Folegati, M. M. Iglesias, I. Makkonen, and M. J. Puska. Positron localization effects on the Doppler broadening of the annihilation line: Aluminum as a case study. *Phys. Rev. B*, 72:054112, 2005.

[84] I. Makkonen, M. Hakala, and M. J. Puska. First-principles calculation of positron states and annihilation at defects in semiconductors. *Physica B*, 376–77(0):971–4, 2006.

[85] J. C. Erskine and J. D. McGervey. Electron momentum distribution in silicon and germanium by positron annihilation. *Phys. Rev.*, 151:615–20, 1966.

[86] Z. Tang, M. Hasegawa, Y. Nagai, and M. Saito. Density functional study on metastable bcc copper: Electronic structure and momentum density of positron-electron pairs. *Phys. Rev. B*, 65:195108, 2002.

[87] I. Makkonen, M. Hakala, and M. J. Puska. Modeling the momentum distributions of annihilating electron-positron pairs in solids. *Phys. Rev. B*, 73:035103, 2006.

[88] H. Okamoto, D. J. Chakrabarti, D. E. Laughlin, and T. B. Massalski. The Au-Cu (gold-copper) system. *J. Phase Equilib.*, 8(5):454–474, 1987.

[89] C. Hugenschmidt, G. Kögel, R. Repper, K. Schreckenbach, P. Sperr, and W. Triftshäuser. First platinum moderated positron beam based on neutron capture. *Nucl. Instrum. Meth. B*, 198(3-4):220 – 229, 2002.

[90] C. Piochacz, G. Kögel, W. Egger, C. Hugenschmidt, J. Mayer, K. Schreckenbach, P. Sperr, M. Stadlbauer, and G. Dollinger. A positron remoderator for the high intensity positron source NEPOMUC. *Appl. Surf. Sci.*, 255(1):98 – 100, 2008.

[91] C. Piochacz, E. Erdnüß, T. Gigl, N. Grill, and C. Hugenschmidt. Enhancement and transformation of the phase space density of the NEPOMUC positron beam. *J. Phys.: Conf. Ser.*, 505(1):012027, 2014.

[92] C. Piochacz. *Generation of a high-brightness pulsed positron beam for the Munich scanning positron microscope*. PhD thesis, Technische Universität München, 2009.

[93] B. Friedl. *Temperature dependent Doppler broadening spectroscopy with monoenergetic positrons*. Bachelor thesis, Technische Universität München, 2010.

[94] Struck Innovative Systems. *SIS3302 12xx Firmware - Gamma*. SIS GmbH, Hamburg, v101 edition, 2008.

[95] Energy and intensity standards. Online available at http://ie.lbl.gov/decay.html; lastly accessed on 29th July 2015.

[96] B. Löwe, M. Reiner, W. Egger, C. Hugenschmidt, and G. Dollinger. A position sensitive germanium detector for the measurement of angular deviation of annihilation radiation. *J. Phys.: Conf. Ser.*, 443(1):012098, 2013.

[97] L. Milechina and B. Cederwall. 3d position sensitivity of a highly segmented Ge detector. *Nucl. Instrum. Meth. A*, 550(1-2):278 – 291, 2005.

[98] Geant4: A toolkit for the simulation of the passage of particles through matter, 2007. Online available at http://geant4.web.cern.ch/geant4/; lastly accessed on 26th August 2015.

[99] J. Roth, J. H. Primbsch, and R. P. Lin. Segmentation and pulse shape discrimination techniques for rejecting background in germanium detectors. *IEEE T. Nucl. Sci.*, 31(1):367–371, 1984.

[100] C. Pfleiderer, G. J. McMullan, S. R. Julian, and G. G. Lonzarich. Magnetic quantum phase transition in MnSi under hydrostatic pressure. *Phys. Rev. B*, 55:8330–8338, 1997.

[101] A. E. Petrova, E. D. Bauer, V. Krasnorussky, and S. M. Stishov. Behavior of the electrical resistivity of MnSi at the ferromagnetic phase transition. *Phys. Rev. B*, 74:092401, 2006.

[102] M. Reiner, A. Bauer, M. Leitner, W. Anwand, M. Butterling, T. Gigl, P. Kudejova, A. Wagner, C. Pfleiderer, and C. Hugenschmidt. Point defects in MnSi and their influence on magnetic properties. To be submitted for publication in Oct. 2015.

[103] B. Meyer and M. Fähnle. Atomic defects in the ordered compound B2-NiAl: A combination of ab initio electron theory and statistical mechanics. *Phys. Rev. B*, 59:6072–6082, 1999.

[104] M. Leitner. Thermodynamics of point defects and diffusion mechanisms in B2-ordered compounds. *ArXiv e-prints*, arXiv:1503.03798 [cond-mat.mtrl-sci], 2015.

[105] A. Neubauer. *Single crystal growth of intermetallic compounds with unusual low temperature properties*. PhD thesis, Technische Universität München, 2011.

[106] A. Neubauer, J. Boeuf, A. Bauer, B. Russ, H. v. Löhneysen, and C. Pfleiderer. Ultra-high vacuum compatible image furnace. *Rev. Sci. Instrum.*, 82(1):–, 2011.

[107] H. Okamoto. Mn-Si (manganese-silicon). *J. Phase Equilib.*, 12(4):505–507, 1991.

[108] P. Kudejova, G. Meierhofer, K. Zeitelhack, J. Jolie, R. Schulze, A. Türler, and T. Materna. The new PGAA and PGAI facility at the research reactor FRM II in Garching near Munich. *J. Radioanal. Nucl. Chem.*, 278(3):691–695, 2008.

[109] D. W. Gidley and W. E. Frieze. Reemitted-positron spectroscopy of thin metal films. *Phys. Rev. Lett.*, 60(12):1193–1196, 1988.

[110] F. A. Selim, D. P. Wells, J. F. Harmon Harmon, J. Kwofie, R. Spaulding, G. Erickson, and T. Roney. Bremsstrahlung-induced highly penetrating probes for nondestructive assay and defect analysis. *Nucl. Instrum. Meth. A*, 495(2):154 – 160, 2002.

[111] F. A. Selim, D. P. Wells, J. F. Harmon, W. Scates, J. Kwofie, R. Spaulding, S. P. Duttagupta, J. L. Jones, T. White, and T. Roney. Doppler broadening measurements of positron annihilation using bremsstrahlung radiation. *Nucl. Instrum. Meth. B*, 192(1-2):197 – 201, 2002.

[112] F. A. Selim, D. P. Wells, J. F. Harmon, and J. Williams. Development of accelerator-based γ-ray-induced positron annihilation spectroscopy technique. *J. Appl. Phys.*, 97(11):–, 2005.

[113] M. Butterling, W. Anwand, G. Brauer, T. E. Cowan, A. Hartmann, M. Jungmann, K. Kosev, R. Krause-Rehberg, A. Krille, R. Schwengner, and A. Wagner. Positron annihilation spectroscopy using high-energy photons. *Phys. Status Solidi A*, 207(2):334–337, 2010.

[114] M. Butterling, W. Anwand, T. E. Cowan, A. Hartmann, M. Jungmann, R. Krause-Rehberg, A. Krille, and A. Wagner. Gamma-induced positron spectroscopy (GiPS) at a superconducting electron linear accelerator. *Nucl. Instrum. Meth. B*, 269(22):2623 – 2629, 2011.

[115] A. Wagner, W. Anwand, M. Butterling, T. E. Cowan, F. Fiedler, M. Kempe, and R. Krause-Rehberg. Annihilation lifetime spectroscopy using positrons from bremsstrahlung production. *Defect Diffus. Forum*, 331:41–52, 2012.

[116] R. Schwengner, R. Beyer, F. Dönau, E. Grosse, A. Hartmann, A. R. Junghans, S. Mallion, G. Rusev, K. D. Schilling, W. Schulze, and A. Wagner. The photon-scattering facility at the superconducting electron accelerator ELBE. *Nucl. Instrum. Meth. A*, 555(1-2):211 – 219, 2005.

[117] M. Butterling, W. Anwand, T. E. Cowan, A. Hartmann, M. Jungmann, R. Krause-Rehberg, A. Krille, and A. Wagner. Gamma-induced positron spectroscopy (GiPS) at a superconducting electron linear accelerator. *Nucl. Instrum. Meth. B*, 269(22):2623 – 2629, 2011. Figure reprinted with permission from Elsevier.

[118] M. Butterling. *Application of High-Energy Photons for Positron Annihilation Spectroscopy and Positronium Chemistry.* PhD thesis, Martin-Luther-Universität Halle-Wittenberg, 2014.

[119] J. Kansy. Microcomputer program for analysis of positron annihilation lifetime spectra. *Nucl. Instrum. Meth. A*, 374(2):235 – 244, 1996.

[120] D. Giebel and J. Kansy. LT10 program for solving basic problems connected with defect detection. *Phys. Procedia*, 35(0):122 – 127, 2012. Positron Studies of Defects 2011.

[121] J. Kansy and D. Giebel. LT10, 2010. Online available at http://prac.us.edu.pl/ kansy/index.php?id=lt10; lastly accessed on 7th April 2015.

[122] K. A. Müller and H. Burkard. $SrTiO_3$: An intrinsic quantum paraelectric below 4 K. *Phys. Rev. B*, 19:3593–3602, 1979.

[123] C. S. Koonce, Marvin L. Cohen, J. F. Schooley, W. R. Hosler, and E. R. Pfeiffer. Superconducting transition temperatures of semiconducting $SrTiO_3$. *Phys. Rev.*, 163:380–390, 1967.

[124] A. Ohtomo and H. Y. Hwang. A high-mobility electron gas at the $LaAlO_3/SrTiO_3$ heterointerface. *Nature*, 427:423–426, 2004.

[125] S. Thiel, G. Hammerl, A. Schmehl, C. W. Schneider, and J. Mannhart. Tunable quasi-two-dimensional electron gases in oxide heterostructures. *Science*, 313(5795):1942–1945, 2006.

[126] P. R. Willmott and J. R. Huber. Pulsed laser vaporization and deposition. *Rev. Mod. Phys.*, 72:315–328, 2000.

[127] G. Hammerl. *Neues Verfahren zur Optimierung von Bandsupraleitern.* PhD thesis, Universität Augsburg, 2004. PhD thesis.

[128] J. D. Jorgensen, B. W. Veal, A. P. Paulikas, L. J. Nowicki, G. W. Crabtree, H. Claus, and W. K. Kwok. Structural properties of oxygen-deficient $YBa_2Cu_3O_{7-\delta}$. *Phys. Rev. B*, 41:1863–1877, 1990.

[129] T. A. Zaleski and T. K. Kopeć. Possible origin of 60-K plateau in the $YBa_2Cu_3O_{6+y}$ phase diagram. *Phys. Rev. B*, 74:014504, 2006.

[130] R. J. Cava, B. Batlogg, C. H. Chen, E. A. Rietman, S. M. Zahurak, and D. Werder. Oxygen stoichiometry, superconductivity and normal-state properties of $YBa_2Cu_3O_{7-\delta}$. *Nature*, 329(6138):423–425, 1987.

[131] J. Bardeen, L. N. Cooper, and J. R. Schrieffer. Theory of superconductivity. *Phys. Rev.*, 108:1175–1204, 1957.

[132] C. E. Gough, M. S. Colclough, E. M. Forgan, R. G. Jordan, M. Keene, C. M. Muirhead, A. I. M. Rae, N. Thomas, J. S. Abell, and S. Sutton. Flux quantization in a high-T_c superconductor. *Nature*, 326:855–855, 1987.

[133] D. Manske. *Theory of unconventional superconductors: Cooper pairing mediated by spin excitations*. Springer-Verlag, 2004.

[134] J. L. Tallon, C. Bernhard, H. Shaked, R. L. Hitterman, and J. D. Jorgensen. Generic superconducting phase behavior in high-T_c cuprates: T_c variation with hole concentration in $YBa_2Cu_3O_{7-\delta}$. *Phys. Rev. B*, 51:12911–12914, 1995.

[135] R. Liang, D. A. Bonn, and W. N. Hardy. Evaluation of CuO_2 plane hole doping in $YBa_2Cu_3O_{6+x}$ single crystals. *Phys. Rev. B*, 73:180505, 2006.

[136] V. M. Matic, N. Dj. Lazarov, and M. Milic. A model for the quasi 60 K plateau in the $YBa_2Cu_3O_{6+x}$ high-T_c compound. *J. Alloys Compd.*, 551(0):189 – 194, 2013.

[137] J. D. Guo A. Schilling, M. Cantoni and H. R. Ott. Superconductivity above 130 K in the Hg – Ba – Ca – Cu – O system. *Nature*, 363:56 – 58, 1993.

[138] Z.-A. Ren, W. Lu, J. Yang, W. Yi, X.-L. Shen, Zheng-Cai, G.-C. Che, X.-L. Dong, L.-L. Sun, Zhou Fang, and Zhao Zhong-Xian. Superconductivity at 55 K in Iron-based f-doped layered quaternary compound $SmO_{1-x}F_xFeAs$. *Chin. Phys. Lett.*, 25(6):2215, 2008.

[139] Z.-A. Ren, W. Lu, J. Yang, W. Yi, X.-L. Shen, Zheng-Cai, G.-C. Che, X.-L. Dong, L.-L. Sun, F. Zhou, and Z.-X. Zhao. Superconductivity and phase diagram in iron-based arsenic-oxides $ReFeAsO_{1-\delta}$ (Re = rare-earth metal) without fluorine doping. *Europhys. Lett.*, 83(1):17002, 2008.

[140] D. Singh, W. E. Pickett, E. C. von Stetten, and S. Berko. Theoretical electron-positron zone-reduced momentum density for $YBa_2Cu_3O_7$: Fermi surface and wave-function effects. *Phys. Rev. B*, 42:2696–2699, 1990.

[141] A. Bansil, P. E. Mijnarends, and L. C. Smedskjaer. Fermi surface and electron-positron momentum density in $YBa_2Cu_3O_7$. *Phys. Rev. B*, 43:3667–3670, 1991.

[142] B. Barbiellini, P. Genoud, J. Y. Henry, L. Hoffmann, T. Jarlborg, A. A. Manuel, S. Massidda, M. Peter, W. Sadowski, H. J. Scheel, A. Shukla, A. K. Singh, and E. Walker. Positron annihilation on single crystals of $YBa_2Cu_3O_{7-x}$. *Phys. Rev. B*, 43:7810–7825, 1991.

[143] E. C. von Stetten, S. Berko, X. S. Li, R. R. Lee, J. Brynestad, D. Singh, H. Krakauer, W. E. Pickett, and R. E. Cohen. High sensitivity of positrons to oxygen vacancies

and to copper-oxygen chain disorder in $YBa_2Cu_3O_{7-x}$. *Phys. Rev. Lett.*, 60:2198–2201, 1988.

[144] M. Peter and A. A. Manuel. Positron annihilation studies of high- T_c superconductors. *Phys. Scr.*, 1989(T29):106, 1989.

[145] H. Haghighi, J.H. Kaiser, S. Rayner, R.N. West, J.Z. Liu, R. Shelton, R.H. Howell, F. Solal, and M.J. Fluss. Direct observation of Fermi surface in $YBa_2Cu_3O_{7-\delta}$. *Phys. Rev. Lett.*, 67(3):382–385, 1991.

[146] L. C. Smedskjaer, A. Bansil, U. Welp, Y. Fangp, and K. G. Bailey. Positron studies of metallic $YBa_2Cu_3O_{7-x}$. *J. Phys. Chem. Solids*, 52(11-12):1541 – 1549, 1991. Special Issue Fermiology of High-Tc Superconductors.

[147] L. C. Smedskjaer, A. Bansil, U. Welp, Y. Fang, and K. G. Bailey. A temperature dependent 2d-ACAR study of untwinned metallic $YBa_2Cu_3O_{7-x}$. *Physica C*, 192(3-4):259 – 271, 1992.

[148] B. Barbiellini, M. Gauthier, L. Hoffmann, T. Jarlborg, A. A. Manuel, S. Massidda, M. Peter, W. Sadowski, A. Shukla, and E. Walker. Positron annihilation in $YBa_2Cu_3O_{7-\delta}$: A clearer picture. *Physica C*, 209(1-3):75 – 78, 1993.

[149] K. O. Jenson, R. M. Nieminen, and M. J. Puska. Positron states in $YBa_2Cu_3O_{7-x}$. *J. Phys.: Condens. Matter*, 1(23):3727, 1989.

[150] R. M. Nieminen. Positron trapping in oxide superconductors. *J. Phys. Chem. Solids*, 52(11):1577 – 1587, 1991. Special Issue Fermiology of High-T_c Superconductors.

[151] T. McMullen, P. Jena, S. N. Khanna, Yi Li, and Kjeld O. Jensen. Positron trapping at defects in copper oxide superconductors. *Phys. Rev. B*, 43:10422–10430, 1991.

[152] L. C. Smedskjaer, B. W. Veal, D. G. Legnini, A. P. Paulikas, and L. J. Nowicki. Positron trapping in the superconductor $YBa_2Cu_3O_x$:$Ba_2Cu_3O_x$. *Physica B+C*, 150(11-12):56 – 60, 1988.

[153] S. G. Usmar, P. Sferlazzo, K. G. Lynn, and A. R. Moodenbaugh. Temperature dependence of positron-annihilation parameters in $YBa_2Cu_3O_{7-x}$ above and below the superconducting transition. *Phys. Rev. B*, 36:8854–8857, 1987.

[154] C. Q. Tang, B. R. Li, and A. Chen. Positron-annihilation study of oxygen-deficient $YBa_2Cu_3O_x$. *Phys. Rev. B*, 42:8078–8080, 1990.

[155] H. Hermes, M. Forster, and H.-E. Schaefer. High-temperature equilibrium study of the oxygen-site occupancy in $YBa_2Cu_3O_{7-\delta}$ by positron annihilation. *Phys. Rev. B*, 43:10399–10404, 1991.

[156] D. Singh, W. E. Pickett, R. E. Cohen, H. Krakauer, and S. Berko. Positron annihilation in high-T_c superconductors. *Phys. Rev. B*, 39:9667–9670, 1989.

[157] P. E. A. Turchi, A. L. Wachs, K. H. Wetzler, J. H. Kaiser, R. N. West, Y. C. Jean, R. H. Howell, and M. J. Fluss. Electron momentum density studies in high-T_c materials by positron annihilation spectroscopy: Theory and experiment. *J. Phys.: Condens. Matter*, 2(6):1635, 1990.

[158] P. E. Mijnarends and A. Bansil. Theory of electron and positron momentum distributions in solids. In A. Dupasquier and A. P. Mills jr., editors, *Proceedings of the International School of Physics 'Enrico Fermi' – 125: Positron Spectroscopy of Solids*. IOS press, 1995.

[159] G. Hammerl, A. Schmehl, R. R. Schulz, B. Goetz, H. Bielefeldt, C. W. Schneider, H. Hilgenkamp, and J. Mannhart. Enhanced supercurrent density in polycrystalline $YBa_2Cu_3O_{7-\delta}$ at 77 K from calcium doping of grain boundaries. *Nature*, 407:162–164, 2000.

[160] P. Benzi, E. Bottizzo, and N. Rizzi. Oxygen determination from cell dimensions in YBCO superconductors. *J. Cryst. Growth*, 269(2-4):625 – 629, 2004.

[161] M. Reiner, T. Gigl, R. Jany, G. Hammerl, and C. Hugenschmidt. Detection and imaging of the oxygen deficiency in single crystalline $YBa_2Cu_3O_{7-\delta}$ thin films using a scanning positron beam. *Appl. Phys. Lett.*, 106(11):111910, 2015.

[162] R. A. Mackie, S. Singh, J. Laverock, S. B. Dugdale, and D. J. Keeble. Vacancy defect positron lifetimes in strontium titanate. *Phys. Rev. B*, 79:014102, 2009.

[163] D. J. Keeble, S. Wicklein, R. Dittmann, L. Ravelli, R. A. Mackie, and W. Egger. Identification of *a*- and *b*-site cation vacancy defects in perovskite oxide thin films. *Phys. Rev. Lett.*, 105:226102, 2010.

[164] J. R. LaGraff and D. A. Payne. Chemical diffusion of oxygen in single-crystal and polycrystalline $YBa_2Cu_3O_{6+x}$ determined by electrical-resistance measurements. *Phys. Rev. B*, 47:3380–3390, 1993.

[165] Y. Li, J. A. Kilner, T. J. Tate, M. J. Lee, R. J. Chater, H. Fox, R. A. De Souza, and P. G. Quincey. Secondary-ion-mass-spectroscopy study of oxygen tracer diffusion in a *c*-axis-oriented $YBa_2Cu_3O_{7-\delta}$ film. *Phys. Rev. B*, 51:8498–8502, 1995.

[166] H. Mehrer. *Diffusion in solids*. Springer, 2007.

[167] X. X. Xi, G. Linker, O. Meyer, E. Nold, B. Obst, F. Ratzel, R. Smithey, B. Strehlau, F. Weschenfelder, and J. Geerk. Superconducting and structural properties of

YBaCuO thin films deposited by inverted cylindrical magnetron sputtering. *Z. Phys. B*, 74(1):13–19, 1989.

[168] M. A. Noah, D. Flötotto, Z. Wang, M. Reiner, C. Hugenschmidt, and E. J. Mittemeijer. Interdiffusion in epitaxial Ag/Au thin films; an AES sputter-depth profiling and positron annihilation study. In preparation for submission.

[169] P. Parente, T. Leguey, V. de Castro, T. Gigl, M. Reiner, C. Hugenschmidt, and R. Pareja. Characterization of ion-irradiated ODS Fe-Cr alloys by Doppler broadening spectroscopy using a positron beam. *J. Nucl. Mater.*, 464(0):140 – 146, 2015.

Acknowledgments

Finally, I want to thank all people who have supported me during the work for this thesis. At the first place, I want to thank PD Dr. Christoph Hugenschmidt who attracted my interest in the interesting field of positron physics and enabled the funding of my position from BMBF projects. During my work, I benefited from his valuable advice in many occasions, his on-going, optimistic motivation for trying new things and his permanent readiness for fruitful discussions. Moreover, I am thankful for the possibility to visit many national and international conferences which have given important input for this work.

Here, I also want to acknowledge the support all other (former) coworkers in the NEPOMUC team from Technische Universität München and Universität der Bundeswehr München. The work of Dr. Christian Piochacz and Thomas Gigl was most important for the daily activity at the CDB spectrometer. Christian provided an excellent beam for our experiments, was always available for trouble shooting at the beamline and engaged in further enhancing the beam quality. Beyond that I could profit from his considerable experience in constructing beamline and UHV components and from daily professional discussions with him. I wish him that his football team will win the Champions League again. Thomas as direct colleague at the CDB spectrometer was not only a great support during beam times and for maintenance of the spectrometer but also helped a lot with exceptional manual skills whenever there was any kind of construction work to be done. Here, I also acknowledge the important support of Sebastian Vohburger who constructed the beamline to the CDB spectrometer and was always ready to help in all the technical work which is necessary to run positron beam experiments. At this place, I thank two former PhD students, namely Dr. Martin Stadlbauer who constructed the CDB spectrometer and Dr. Philip Pikart who further upgraded this set-up. For improving the hardware control of the spectrometer, the advice of Marcel Dickmann and Benjamin Rienäcker was very useful. The use of the pixelated detectors was a common project with Benjamin Löwe, who gave important contributions to this project, in particular with his astonishing programming skills for the read-out algorithm and the accompanying Geant4 simulations. Here, Matthias Hackenberg also performed interesting studies which helped to understand the results presented in this work. Dr. Michael Leitner with his impressively deep understanding of nearly all matters in physics gave valuable in-put not only because of his theoretical work in the MnSi studies but also due to many discussions about any experimental findings. I want to especially thank Hubert Ceeh, with whom I have been working

together for six years. He is a true walking encyclopedia in the wide field of physics and always willing to share his profound knowledge and experience with others. Moreover, he motivated our group for many delighting events such as visits at the Oktoberfest or mountain tours. At the ACAR spectrometer, which Hubert constructed together with Josef Andreas Weber, we could also perform measurements with the pixelated detectors. Here, I also thank Josef who made a useful positron lifetime spectrometer in our laboratory available for complementary measurements. During my daily work I also benefited from many fruitful discussions with scientists from Universität der Bundeswehr München, especially with Dr. Luca Ravelli and Dr. Werner Egger. Furthermore, I thank Hubert Ceeh, Marcel Dickmann, Benjamin Löwe, Johannes Mitteneder and Josef Andreas Weber for proofreading this thesis. Moreover, I thank all colleagues, the mentioned ones and Ulrich Ackermann, Lukas Beddrich, Niklas Grill, Eicke Hecht, Bernhardt Kallies, Florian Lippert, Pascal Neibecker, Matthias Thalmayr, Matthias Tischler and Samantha Zimnkik, for many important discussions in the field of physics and beyond, their cooperation and contribution to an effective and often enjoyable atmosphere of work.

Important parts of my research were done in cooperation with collaborators from external groups. I especially want to thank Dr. Andreas Bauer and Prof. Dr. Christian Pfleiderer and their coworkers from Technische Universität München who provided a large set of well characterized MnSi crystals for positron experiments and whose expertise was very helpful in the interpretation of data. Within this project, I also acknowledge the support of Wolfgang Anwand, Dr. Maik Butterling and Dr. Andreas Wagner from Helmholtz-Zentrum Dresden-Rossendorf during the GIPS measurements and their analysis. I am also thankful to Dr. Petra Kudejova for the accompanying PGAA measurements. Moreover, I thank Dr. Rainer Jany and Prof. Dr. German Hammerl and their coworkers from Universität Augsburg for their cooperation in the studies on YBCO. They prepared excellent films, conducted comprehensive complementary experiments and always were open for discussions on our results. Beyond these directly contributed persons, I also want to thank many of the users who visited the CDB spectrometer. The discussions with them often gave new insights and were useful for further improving the CDB experiment.

Last but not least I want to thank my family and friends for mental support during the last years. Especially my parents, Ulrike and Rudolf Reiner, supported me a lot during my studies and enabled my academic education.